GEOMETRIC ANALYSIS OF FINITE DIFFERENCE TIME DOMAIN SIMULATION FOR DAMAGE ASSESSMENT IN GROUND PENETRATING RADAR APPLICATIONS

BY

BURAK BOYACI
BACHELOR OF SCIENCE, MIDDLE EAST TECHNICAL UNIVERSITY,
ANKARA, TURKEY (2008)

SUBMITTED IN PARTIAL FULFILLMENT OF THE REQUIREMENTS
FOR THE DEGREE OF MASTER OF SCIENCE
DEPARTMENT OF CIVIL AND ENVIRONMENTAL ENGINEERING
UNIVERSITY OF MASSACHUSETTS LOWELL

Signature of the Author . . . . . .
Department of Civil and Environmental Engineering
June 10, 2010

Signature of Thesis Supervisor . . . . . .
Tzu-Yang Yu
Assistant Professor

Committee Member Signature . . . . . .
Professor Donald Leitch
Department of Civil and Environmental Engineering

Committee Member Signature . . . . . .
Professor Susan Faraji
Department of Civil and Environmental Engineering

GEOMETRIC ANALYSIS OF FINITE DIFFERENCE TIME DOMAIN SIMULATION FOR DAMAGE ASSESSMENT IN GROUND PENETRATING RADAR APPLICATIONS

BY

BURAK BOYACI
BACHELOR OF SCIENCE, MIDDLE EAST TECHNICAL UNIVERSITY,
ANKARA, TURKEY (2008)

ABSTRACT OF A THESIS SUBMITTED TO THE FACULTY OF THE
DEPARTMENT OF CIVIL AND ENVIRONMENTAL ENGINEERING
IN PARTIAL FULFILLMENT OF THE REQUIREMENTS
FOR THE DEGREE OF
MASTER OF SCIENCE
UNIVERSITY OF MASSACHUSETTS LOWELL
2010

Thesis Supervisor: Tzu-Yang Yu
Title: Assistant Professor

Abstract

Detection and characterization of damages in civil structures is vital for public safety. Microwave/radar NDT (Nondestructive Testing) techniques are suitable for in-depth assessment of concrete structures since electromagnetic waves can penetrate into dielectric materials like concrete. Ground penetrating radar (GPR) is one of the commonly used microwave/radar techniques for concrete structures. Numerical simulation provides valuable insights to understand the wave propagation and scattering phenomena in the GPR applications for subsurface defect detection and characterization. In this thesis, Finite Difference Time Domain (FDTD) methods are used. Delaminations with different sizes and at different depths inside a rectangular concrete slab with different dielectric properties are modeled. From the simulation results, it is found that delaminations are detectable in all cases. Moreover, the curvature values of arch-like shapes obtained from B-scan images of concrete slabs are calculated. It is shown that the curvature value and the size of delamination are related. Finally, a procedure for estimating the size of subsurface delamination in concrete slabs is proposed.

Acknowledgements

I would like to offer my deepest appreciations and utmost gratitude to my advisor, Dr. Tzu-Yang Yu, whose enormous and endless efforts has enhanced my ability and personality beyond any expectations.

I also would like to thank my thesis committee members, Dr. Susan Faraji and Prof. Donald Leitch for their valuable comments and inputs.

I am indebted to Dr. Ahmet Yakut and Dr. Oguz Gunes for their assistance during my entire professional education.

Many thanks go to the National Institute of Standards and Technology (NIST) Technology Innovation Program (TIP) for their financial support during my graduate study.

I wish to express my sincere gratitude to I.Cagatay Solak, Samed Maltabas, O.Kubilay Ekekon, Mena Sliman and Gerti Kola for their support and help during the course of this research.

I am heartily thankful to Ilke Tan for her conditionless encouragement and everlasting support.

Finally, I wish to express my forever gratefulness to my mother, Sukran Boyaci, and

my father, Erdal Boyaci, who always make me proud of being their son in every breath of my life. Their unmeasured and unquestionable love always gives me the courage to overcome every obstacle in life. I also wish to gratefully thank my sister, Busra Boyaci, for her warm support.

Contents

List of Figures

List of Tables

Chapter 1

Introduction

Deterioration of engineering structures is inevitable in real life applications, including civil engineering structures. Because the typical design service life of the structures is approximately 50 years or longer, required precautions have to be taken against the deterioration process. From the point of economy, client needs to get benefit from his investment by operating the structure until the end of its service life. On the other hand, precautions must be taken for the public safety to prevent a sudden failure of a structure.

Recent, structural maintanence or repairing/retfrofitting of the damaged/deteriorated structures is favored rather than building a new structure in the field of civil engineering economics. However, adequate inspection, monitoring and evaluation of the structures are needed to detect the deterioration or anomaly, its location and the level of deterioration in order to retrofit the structure properly. Therefore, reliable, accurate and field applicable nondestructive testing (NDT) techniques are required to inspect the current condition of the structure in question. Even after the retrofitting construction, the struc-

ture has to be inspected for the quality assurance of the construction.

Nondestructive testing (NDT) or nondestructive evaluation (NDE) is the appraisal of the condition of a material or structure without causing any damage to the functionality of the material/structure. The aim of NDT is to collect information about both the serviceability and sustainability of the examined structure. For this purpose, various NDT techniques have been developed to provide proper solutions to the problem. NDT techniques can be differentiated according to their key features such as the physical principle behind the technique, wave or field type utilized and the equipment used [31]. Brief descriptions of the techniques are :

- Optical Methods : The techniques rely on the propagation of the electromagnetic waves in the optical spectrum. This method includes visual inspection and laser-based techniques. While visual inspection is easy to conduct and the most commonly used technique for transportation infrastructure such as bridges, accuracy and reliability of the technique sometimes can be questionable because of the qualitative and the subjective nature of the technique [13].

- Acoustic Methods : Acoustic methods utilize the propagation of mechanical waves such as body and surface waves to evaluate the material under test (MUT). The velocity of the waves are affected by the mechanical properties (i.e. Young's modulus) of the MUT. Travelling mechanical waves need to change their path

when they encounter cracks, voids or delamination, resulting in a delay on the arrival time to the transducer and attenuation [23].

- Thermal Methods : These techniques use emitted and/or reflected thermal radiation or temperature from the examined specimen [31]. Various materials having different thermal properties emit different amounts of thermal energy. On the other hand, defects or anomalies such as voids do not allow the thermal radiation and changes the thermal image. Therefore, thermal energy and radiation can be used for distinguishing one material from another and for detecting anomalies.

- Radiographic Methods : In these methods, X-rays, gamma-rays, beta rays and neutrons penetrate through one side of the material under test to obtain a shadow image (radiograph) onto a film on the other side [8]. Different levels of absorption of the penetrating radiation can be identified from the contrast colors in the radiograph. In the application of the technique, access to the both sides of the material and the safety concerns regarding the radiation of these rays can be considered as drawbacks of the technique.

- Magnetic and Electrical Methods : In magnetic methods such as magnetic particle inspection, after magnetizing the material and spraying with magnetic particles, the distortion of the magnetic field is observed in order to detect surface cracks in the MUT. Electrical methods such as eddy current testing relies on the

flowing current on the surface of the material. Changes in the electrical properties of the specimen such as variation of the amplitude of electromotive force indicate the presence of a defect. However, in order to utilize this method, material under test must be conductive.

- Microwave/Radar Methods : These methods are used to inspect the MUT and assess their characteristics such as material composition and geometry by utilizing the transmission and/or reflection properties of electromagnetic waves interacting with the MUT. A portion of incident electromagnetic waves are scattered/reflected from an interface of two materials such as concrete-air interface because of the change in the electromagnetic properties of the medium. By interpreting the scattering effect of the waves, not only cracks and air voids but also material composition of the MUT can be evaluated.

From civil engineering point of view, sometimes NDT techniques are insufficient or discouraging. This is because the results are chosen from a technique either not having enough accuracy or being inadequate for the structural problem in question [23]. For instance, general purpose and routine condition evaluation of concrete structures is usually conducted by visual inspection. However, it is difficult or even not possible to assess subsurface defects such as internal voids and delaminations by visual inspection [16]. In fact, in building inspections, walls are covered by paint or wall paper making the surface assessment difficult using visual methods [27].

Among various NDT methods, microwave or radar methods are one of the reliable, accurate and applicable techniques for the inspection of concrete material. Although electromagnetic waves can not penetrate into conductors such as metals, they can penetrate into dielectric materials such as concrete. Therefore, the methods are capable of conducting in-depth assessment of concrete structures. By utilizing this ability, subsurface cracks and voids can be detected [28, 20, 16, 32, 34]. Also, surface defects are obviously detectable by evaluating the reflection properties of the electromagnetic waves [24, 27]. The phase and velocity of electromagnetic waves change while they are traveling through the interface between two dielectrics with different dielectric properties. As a result, thickness of different layers of materials, such as concrete cover, asphalt layer thickness on bridge decks, can be determined using this technique [22, 2]. In addition, steel reinforcements inside concrete can be located by their strong reflection/scattering of electromagnetic waves [29, 3, 28, 32]. Beside these capabilities, by interpreting the dielectric properties of concrete, curing condition of fresh concrete, material composition of hardened concrete, such as water/cement ratio, and compressive strength of hardened concrete can be estimated [6, 1, 15].

Ground penetrating radar (GPR) is one of the microwave/radar NDT methods using electromagnetic waves to image the subsurface of the MUT. GPR transmits electromagnetic waves towards the MUT. If electromagnetic waves impinge on a boundary with different dielectric properties in the subsurface of the MUT, GPR detects the reflections caused by the boundary. GPR is used to detect the subsurface anomalies in concrete

structures as well as various other applications. Figure 1-1 shows the application of GPR on a bridge deck.

Figure 1-1: Bridge deck evaluation using GPR [*source* : *GSSI*]

Numerical/computer simulation is always considered as a powerful tool by researchers. In the simulation environment, one has an unlimited freedom to alter or try every condition desired and observe the results, which makes the simulation result insightful, before expensive physical experiments are performed. Comparing radar NDT measurement with computer simulation, it can be concluded that simulation provides valuable ideas about the prediction and interpretation of measurement results [7]. Therefore, computer simulation can be very helpful to understand the radar measurements of concrete for damage detection by trying different defect geometries and different material properties in the simulations.

1.1 Research Objective

The objective of this research is to assist the interpretation of microwave/radar NDT measurements of GPR for detecting the subsurface anomalies/defects (e.g., voids, delaminations) in concrete structures. The thesis aims at investigating the interaction between electromagnetic waves and subsurface anomalies with different geometries in concrete subtrates and the estimation of the size of defect in concrete structures.

1.2 Thesis Approach

To achieve the objective, numerical simulation is applied in conducting a parametric study in this research. Finite difference time domain (FDTD) methods are used to simulate the propagation and scattering of electromagnetic waves to observe the reflection properties of the material under test (MUT). Rectangular concrete specimens with various defect geometries are modeled; different electromagnetic properties of concrete are also considered.

1.3 Organization of the Thesis

The organization of the thesis is described in the followings

Chapter 2 reviews both the application of microwave/radar NDT methods for the inspection of concrete and their numerical simulations.

Chapter 3 introduces FDTD methods by explaining their principles. Moreover, a simulation scheme is illustrated.

Chapter 4 reports the results of numerical simulation. Various simulation cases including different defect geometries and material properties are investigated and the results are compared. Using the simulation results, a relationship between the reflection properties of the MUT and the size of defect is found.

Chapter 5 summarizes the findings from simulation results. Discussions on the results and future work are also provided.

Chapter 2

Literature Review

Among existing NDT techniques, microwave/radar NDT is considered as promising, reliable and applicable in civil engineering due to following reasons [31]:

- distant and/or non-contact testing ability
- less vulnerable to temperature change
- capable of penetrating into dielectric materials (such as concrete)
- no limitations due to safety concerns during operation

In view of these reasons, active research and industrial developments of microwave/radar NDT techniques for the condition assessment of concrete structures are reported. On the other hand, numerical simulation also has been applied to model laboratory or field measurements. This chapter reports previous physical measurements and numerical simulation work from literature regarding the use of microwave/radar NDT technique

for inspection of concrete structures.

2.1 Physical Measurement

Microwave/radar NDT techniques have been used to determine the material properties of concrete such as moisture content and w/c (water/cement) ratios and to provide useful information about the deterioration and mechanical strength of concrete. Klysz et al. (2003) [17] used radar to estimate the moisture content of concrete. A concrete slab with a w/c = 0.58 was tested in both dry and surface wet conditions by a measurement system consisted of one transmitter and one receiver antennas with adjustable distance between the antennas. Speed of the ”material wave” (the wave propagating in the subsurface at the vicinity of the air-specimen interface) was measured at a distance of 4 cm between the antennas from 100 MHz to 1.3 GHz. Comparing the speeds of the material wave in two conditions of the slab (dry and surface wet), it was concluded that the speed of the wave decreases when the surface of the slab is wet. Moreover, the dielectric constant of the concrete was calculated using the velocity.

Bois et al. (2000) [6] correlated the w/c ratio and ca/c (coarse aggreagete-cement ratio) with the reflection coefficient using open ended rectangular waveguide. Measurements were collected on cubic specimens with different w/c and ca/c values at frequencies of 3 GHz and 10 GHz. According to their results, w/c can be correlated to the mean value of reflection coefficient at 3 GHz and ca/c to the standart deviation of

the reflection coeffient. On the other hand, Kharkovsky et al. (2002) [15] conducted a similar research using free-space measurement scheme at 10.38 GHz and showed the dependency of reflection and transmission coefficients on the w/c ratio of the specimen under test. Moreover, Al-Mattarneh et al. (2001) [1] used free-space reflection measurements to estimate the w/c and to determine the compressive strength of concrete specimens.

Since metals are strong scatterers of electromagnetic waves, radar techniques can be used to detect rebars in concrete. Chung et al. (1994) [9] used three concrete panels with a w/c = 0.45; a plain concrete panel, a concrete with single layer of rebars, and a concrete panel with double layer of rebars. By using an impulse radar, amplitudes of the reflected electromagnetic waves from the concrete surface and rebars were measured in the time domain. Therefore, the depth of the rebars could be calculated using the difference in arrival times of the reflected waves from concrete surface and rebars. Similiar studies were performed to detect rebars in concrete by Derobert et al. (2002) [10], Shaw et al.(2005) [29] using GPR, Rhim et al. (2000) [28] and Yu et al. (2007) [32] using free-space radar measurements. On the other hand, Begum et al. (2008) [3] proposed a method to determine the diameter of rebars embedded in concrete by measuring the rib's pitch and relating the rib's pitch to the diameter of the rebars.

Nadakuduti et al. (2006) [24] reported the results of detecting surface cracks having various widths and depths in cement mortar and cement paste specimens at various standoff distances using an open-ended rectangular waveguide in the X-band frequency

range (8.2 – 12.4 GHz). In another study, Oka et al. (2009) [27] proposed a near-field radar method to detect sub-millimeter width cracks on the concrete surface. It was shown that the algorithm used for this tool can detect 0.2 mm-wide cracks.

Various studies have been conducted to detect subsurface anomalies. Kim et al. (2004) [16] developed a planar radar antenna array consisting of 8×8 receiving and 8×8 transmitting antennas operating at 5.2 GHz to detect the voids inside concrete blocks. It was shown that developed antenna array with an image reconstruction algorithm can reconstruct the images of the artificial voids created by using Styrofoam (dielectric properties are same as air). Besides, Maierhofer et al. (2003) [21] used a 1.5 GHz radar to estimate the depth of subsurface voids in concrete. It was found that the depth of the voids can be calculated from the traveling time of the impulse reflected from the concrete-void interface as long as the velocity of the impulse in concrete is known.

In addition to the voids inside the concrete, delamination or debonding between the concrete and fiber reinforced polymer (FRP) is a threat for the health of the strengthened/retrofitted FRP-concrete structures. Microwave/radar methods have been used to detect the anomaly at the concrete-FRP interface. Feng et al. (2002) [12] conducted the reflection and transmission measurements on concrete columns wrapped with glass fiber reinforced polymer (GFRP) using a waveguide reflectometer operating at X-band frequency range (8.2 – 12.4 GHZ). At the same frequency range, Kharkovsky et al. (2008) [14] applied the near-field microwave/radar technique on mortar slabs

wrapped with carbon fiber reinforced polymer (CFRP) in laboratory and on CFRP patches bonded elements of a bridge in field using an open-ended waveguide probe. Results of both studies illustrated that bonding condition of concrete-FRP interface can be assessed using the techniques proposed. Furthermore, Yu et al. (2007) [32] proposed a far-field radar NDT technique for the same problem at the same frequency range. However, this technique is not constrained by the inspection distance as in the case of near-field techniques.

2.2 Numerical Simulation

Buyukozturk et al. (1995) [7] visualized the electromagnetic field propagation in concrete using FDTD simulations. Three types of concrete specimens (cylindrical, square and rectangular) were modeled and either a rebar or void was introduced at the center of the specimens. A Gaussian pulse plane wave with a half power bandwidth of 5 GHz was used. Concrete specimens were modeled by a dielectric constant of 4.8 and conductivity of 0.15 mhos/m. Snap shots of the simulation were generated to show the effect of an inclusion (i.e. void or rebar) to the propagation and the scattering of electromagnetic waves inside concrete. Also, electric field amplitude of the received signals were shown in the time domain. It is shown that, by using the model, size of the specimens and the inclusion inside them can be predicted. Detectibility of the inclusion was affected by the shape of the specimen. It is found that the back surface reflections were received earlier when the target is cylindrical than the other shapes due to the edge

effect even though the thickness of all specimens is identical.

Neyrat et al. (2009) [25] used monostatic and multistatic B-scan to simulate the detection of burried objects using GPR. One transmitter emitting a modulated Gaussian impulse with a center frequency of 1.0 GHz and ten receivers employed to detect the buried pipes in heterogeneous medium (dielectric constant assigned as 6). In multistatic B-scan, retiming method was applied by taking the delay between the various receivers into account. The resulting monostatic and retimed multistatic B-scans were compared. It is shown that the B-scan of the latter provides better detectibility than the former. On the other hand, wavefront migration technique is introduced to remove unwanted reflections and hyperbolic reflection characteristics of buried objects from B-scan.

An approach to detect subsurface anomalies inside reinforced concrete bridge decks using 2D FDTD simulations was proposed by Belli et al. (2008) [4]. A healthy bridge deck consisting of an asphalt layer placed on a reinforced concrete substrate was modeled. Dielectric constants assigned for asphalt and concrete were 5 and 10 respectively and the conductivity of these materials was assumed to be zero. An impulse wave with a center frequency of 778 MHz was used in the bridge deck model. A GPR source located at 307.3 mm above the asphalt layer was modeled. The dielectric constants and the thickness of asphalt and concrete, the depth of the rebars and the horizontal spacing between them were calculated from the reflection response. In another model, a rectangular air void was placed underneath the reinforcing steel. However, the void could not be detected from the reflection response due to the strong scattering from the

reinforcing steel. Therefore, subtraction of the reflection response of the healthy deck model from the response of the model with an air void was suggested to show the effect of air void.

A similar study using FDTD methods to model the GPR application on bridge decks was conducted by Zhan et al. (2008) [33]. Both 2D and 3D models of reinforced concrete bridge deck were created to compare the detectibility of the delamination between asphalt and concrete layer and the delamination inside reinforced concrete. The dielectric constants of asphalt and concrete were assumed to be 5 and 9 respectively. A bistatic GPR elevated at 30.6 cm from the asphalt layer was used as an excitation pulse source with 1.0 GHz center frequency to create B-scan images. It was shown that 2D and 3D simulations resulted in approximately the same B-scans for different kinds of defect scenario. Because the bridge deck was relatively uniform in the third dimension and the computational time of 2D simulations were short, it was suggested that 2D simulation is a good approximation for bridge deck models although the accuracy of 3D simulation is superior when the geometry of the model becomes complicated. Later, Belli et al. (2009) [5] also compared 2D and 2.5D models with 3D FDTD models for the detection of bridge deck delaminations and concluded that it is convinient to use 2D or 2.5D simulation for this problem, considering the reduction in computational time.

Liu et al. (2007) [19] utilized FDTD methods to simulate the tunnel coating quality inspection using GPR. In their model, a concrete layer containing metal wires was laid on rock with two delaminations (one filled with water between the concrete and the

rock layers). The dielectric constant and conductivity of the concrete and the rock was assigned to be 6, 0.005 S/m and 5, 0.0001 S/m, respectively. The center frequency of the antenna was 900 MHz, and the excitation source was a Gaussian pulse. Reflection from the delaminations was found to be not clear due to the interference of strong metal wire scattering in the B-scan. However, another simulation model was performed without the presence of the metal wires; the delamination between the concrete and the rock layer was clearly identified in the B-scan.

Nojavan et al. (2009) [26] adopted the Born image algorithm for the damage detection of reinforced concrete structures. A reinforced concrete slab, a horizontal crack and a debonding layer between concrete and one of the rebars were modeled in their 2D FDTD simulation. Dielectric constant and conductivity of the concrete was assigned to be 5.3 and 0.05 S/m, respectively. The center wavelength of the excitation signal in concrete was about 1.7 cm. Actuators and the receivers were densely placed on the upper surface of the modeled slab. Images were constructed from the scattered field created by the excitation of each actuator and obtained from each receiver. It was shown that damage geometries can be estimated correctly using the Born imaging algorithm and any components of electromagnetic field (i.e. Ey, Hz, Hx) can be utilized to identify the damage.

2.3 Summary

In this chapter, previous physical measurement and numerical simulation work are reported regarding the use of microwave/radar NDT techniques for inspection of concrete structures. In ”Physical Measurements” section, investigation of material properties and detection of defect capabilities of microwave/radar NDT techniques are addressed by referring to previous researches. Also, a few numerical simulation studies regarding the defect detection of concrete structures using microwave/radar NDT techniques are reviewed in ”Numerical Simulation” section.

Chapter 3

Numerical Simulation - Finite Difference Time Domain (FDTD) Methods

In the application of microwave/radar NDT methods, numerical simulation is valuable tool for figuring out how electromagnetic waves propagate through concrete and are scatterred due to the presence of anomalies inside concrete. In this simulation work, the time-domain response of scattered electromagnetic waves from a concrete target with various sizes of defect is generated. The finite difference time domain (FDTD) methods using the Yee algorithm [30] are used to solve Maxwell's curl equations (governing equations of electromagnetic fields). FDTD methods can easily accomodate different geometries in the simulation.

3.1 Maxwell's Curl Equations and TE and TM Modes of Waves

Consider an isotropic, nondispersive and lossy material in a linear problem, Maxwell's curl equations can be written as [18];

$$\frac{\partial \bar{E}}{\partial t} = \frac{1}{\epsilon}\left(\nabla \times \bar{H} - \sigma \bar{E}\right) \tag{3.1}$$

$$\frac{\partial \bar{H}}{\partial t} = -\frac{1}{\mu}\left(\nabla \times \bar{E} + \sigma^{*} \bar{H}\right) \tag{3.2}$$

where

$\bar{H}$ = magnetic field strength (amperes/m)

μ = magnetic permeability of the medium (henrys/m)

$\bar{E}$ = electric field strength (volts/m)

σ^{*} = equivalent magnetic loss (ohms/m)

ϵ = electric permittivity of the medium (farads/m)

σ = electric conductivity of the medium (1/ohms/m = siemens/m)

t = time (seconds)

$\times$ = cross product symbol

∇ = curl operator symbol

In this study, concrete is considered as a non-magnetic and lossless material (σ^{*} is

negligible). Therefore, electromagnetic wave propagation in concrete can be modeled by considering ϵ, μ and σ. On the other hand, Maxwell's curl equations depict the four dimensional space-time (i.e. x,y,z and time) response of electromagnetic waves. Equations (3.1) and (3.2) can be expressed in Cartesian coordinate systems as;

$$\frac{\partial E_x}{\partial t} = \frac{1}{\epsilon}\left(\frac{\partial H_z}{\partial y} - \frac{\partial H_y}{\partial z} + \sigma E_x\right) \tag{3.3}$$

$$\frac{\partial E_y}{\partial t} = \frac{1}{\epsilon}\left(\frac{\partial H_x}{\partial z} - \frac{\partial H_z}{\partial x} + \sigma E_y\right) \tag{3.4}$$

$$\frac{\partial E_z}{\partial t} = \frac{1}{\epsilon}\left(\frac{\partial H_y}{\partial x} - \frac{\partial H_x}{\partial y} + \sigma E_z\right) \tag{3.5}$$

$$\frac{\partial H_x}{\partial t} = -\frac{1}{\mu}\left(\frac{\partial E_z}{\partial y} - \frac{\partial E_y}{\partial z}\right) \tag{3.6}$$

$$\frac{\partial H_y}{\partial t} = -\frac{1}{\mu}\left(\frac{\partial E_x}{\partial z} - \frac{\partial E_z}{\partial x}\right) \tag{3.7}$$

$$\frac{\partial H_z}{\partial t} = -\frac{1}{\mu}\left(\frac{\partial E_y}{\partial x} - \frac{\partial E_x}{\partial y}\right) \tag{3.8}$$

When plane electromagnetic waves are considered, the wave component prependicular to the plane of propagation is constant. Therefore, given the x-y plane is the propagation plane, component of the electromagnetic wave in the z direction is constant. In other words $\frac{\partial}{\partial z} = 0$. With this condition and by eliminating the $\frac{\partial}{\partial z}$ terms in the above equations, we have

$$\frac{\partial E_x}{\partial t} = \frac{1}{\epsilon}\left(\frac{\partial H_z}{\partial y} + \sigma E_x\right) \tag{3.9}$$

$$\frac{\partial E_y}{\partial t} = \frac{1}{\epsilon}\left(-\frac{\partial H_z}{\partial x} + \sigma E_y\right) \tag{3.10}$$

$$\frac{\partial E_z}{\partial t} = \frac{1}{\epsilon}\left(\frac{\partial H_y}{\partial x} - \frac{\partial H_x}{\partial y} + \sigma E_z\right) \tag{3.11}$$

$$\frac{\partial H_x}{\partial t} = -\frac{1}{\mu}\left(\frac{\partial E_z}{\partial y}\right) \tag{3.12}$$

$$\frac{\partial H_y}{\partial t} = -\frac{1}{\mu}\left(-\frac{\partial E_z}{\partial x}\right) \tag{3.13}$$

$$\frac{\partial H_z}{\partial t} = -\frac{1}{\mu}\left(\frac{\partial E_y}{\partial x} - \frac{\partial E_x}{\partial y}\right) \tag{3.14}$$

By splitting Eqs.(3.9),(3.10), (3.20),(3.18), (3.19) and (3.17), two electromagnetic wave propagation modes are defined; transverse electric and transverse magnetic. Transverse electric (TEz) waves or TE wave mode can be defined by the following equations.

$$\frac{\partial E_x}{\partial t} = \frac{1}{\epsilon}\left(\frac{\partial H_z}{\partial y} + \sigma E_x\right) \tag{3.15}$$

$$\frac{\partial E_y}{\partial t} = \frac{1}{\epsilon}\left(-\frac{\partial H_z}{\partial x} + \sigma E_y\right) \tag{3.16}$$

$$\frac{\partial H_z}{\partial t} = -\frac{1}{\mu}\left(\frac{\partial E_y}{\partial x} - \frac{\partial E_x}{\partial y}\right) \tag{3.17}$$

Transverse magnetic (TMz) or TM wave mode can be described by the following

governing equations.

$$\frac{\partial H_x}{\partial t} = -\frac{1}{\mu}\left(\frac{\partial E_z}{\partial y}\right) \tag{3.18}$$

$$\frac{\partial H_y}{\partial t} = -\frac{1}{\mu}\left(-\frac{\partial E_z}{\partial x}\right) \tag{3.19}$$

$$\frac{\partial E_z}{\partial t} = \frac{1}{\epsilon}\left(\frac{\partial H_y}{\partial x} - \frac{\partial H_x}{\partial y} + \sigma E_z\right) \tag{3.20}$$

It is observed that TE and TM modes do not contain mutual field components. Therefore, for isotropic materials, TE and TM modes can exist simultaneously without mutual interaction and can be evaluated independently.

3.2 The Yee Algorithm

In order to implement Maxwell's curl equations, both spatial and temporal discretization schemes are needed. For discretization in time and space, finite difference time domain (FDTD) methods are chosen to simulate the propagation and scattering of electromagnetic waves, in view of its explicit solution of Maxwell's curl equations and its accuracy.

For discretization purpose, among the forward difference, backward difference and central difference schemes, the central difference scheme is chosen because of its supe-

rior accuracy over other two. The first-order derivative of an one-dimensional function ($f(x)$) discretized by three difference schemes using Taylor's theorem are provided in the following.

- $\Delta f(x) = f(x+h) - f(x) \Rightarrow \dfrac{\Delta f(x)}{h} - f'(x) = O(h) \longrightarrow$ Forward difference
- $\nabla f(x) = f(x) - f(x-h) \Rightarrow \dfrac{\nabla f(x)}{h} - f'(x) = O(h) \longrightarrow$ Backward difference
- $\delta f(x) = \dfrac{f(x+h) - f(x-h)}{2} \Rightarrow \dfrac{\delta f(x)}{h} - f'(x) = O(h^2) \longrightarrow$ Central difference

As it can be concluded from the above expressions, for small h values, the decrease in the error is much faster in the central difference scheme than the forward difference and backward difference schemes.

For two-dimensional functions as shown in Figure 3-1, the Taylor's series of $f = f(x,y)$ expanding from point 0 in the direction of x is

$$f(x,y) = f(x_0) + \frac{\partial f}{\partial x}\Big|_{x_0}(x-x_0) + \frac{1}{2!}\frac{\partial^2 f}{\partial x^2}\Big|_{x_0}(x-x_0)^2 + \frac{1}{3!}\frac{\partial^3 f}{\partial x^3}\Big|_{x_0}(x-x_0)^3 + \ldots \quad (3.21)$$

Assuming a uniform h, i.e. $\Delta x = \Delta y = h$,

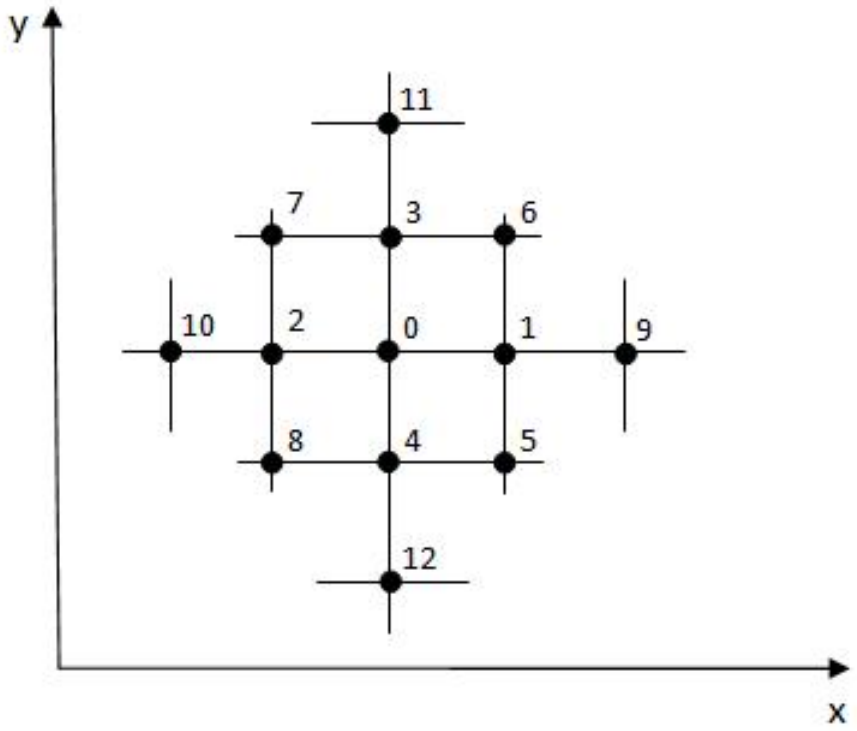

Figure 3-1: Grid configuration

$$x_2 = x_0 - h \tag{3.22}$$

$$x_1 = x_0 + h \tag{3.23}$$

Then, the Eq.(3.21) becomes

$$f(x_2, y_2) = f_2 = f_0 - \frac{\partial f}{\partial x}\Big|_0 h + \frac{\partial^2 f}{\partial x^2}\Big|_0 \frac{h^2}{2} - \frac{\partial^3 f}{\partial x^3}\Big|_0 \frac{h^3}{6} + \ldots \tag{3.24}$$

$$f(x_1, y_1) = f_1 = f_0 + \frac{\partial f}{\partial x}\Big|_0 h + \frac{\partial^2 f}{\partial x^2}\Big|_0 \frac{h^2}{2} + \frac{\partial^3 f}{\partial x^3}\Big|_0 \frac{h^3}{6} + \ldots \tag{3.25}$$

High order terms are negligible when h is small enough. Therefore,

$$f_2 = f_0 - \frac{\partial f}{\partial x}\Big|_0 h + \frac{\partial^2 f}{\partial x^2}\Big|_0 \frac{h^2}{2} \tag{3.26}$$

$$f_1 = f_0 + \frac{\partial f}{\partial x}\Big|_0 h + \frac{\partial^2 f}{\partial x^2}\Big|_0 \frac{h^2}{2} \tag{3.27}$$

Solving for $\frac{\partial f}{\partial x}\Big|_0$ and $\frac{\partial^2 f}{\partial x^2}\Big|_0$ leads to

$$\frac{\partial f}{\partial x}\Big|_0 = \frac{f_1 - f_2}{2h} \tag{3.28}$$

$$\frac{\partial^2 f}{\partial x^2}\Big|_0 = \frac{f_1 - 2f_0 + f_2}{h^2} \tag{3.29}$$

Similarly, $\frac{\partial f}{\partial y}\Big|_0$ and $\frac{\partial^2 f}{\partial y^2}\Big|_0$ are

$$\frac{\partial f}{\partial y}\Big|_0 = \frac{f_3 - f_4}{2h} \tag{3.30}$$

$$\frac{\partial^2 f}{\partial y^2}\Big|_0 = \frac{f_3 - 2f_0 + f_4}{h^2} \tag{3.31}$$

The finite difference time domain solution to Maxwell's curl equations can be found by substituting $\bar{E}$ and $\bar{H}$ into $f(x,y)$.

The Yee algorithm is commonly used for three-dimensional FDTD solutions. In the Yee algorithm, indices i, j and k represents the spatial location of $\bar{E}$ and $\bar{H}$, while n corresponds to time variable in $\bar{E}$ and $\bar{H}$. For example, $(x_i, y_j + \Delta y, z_k + \Delta z, t_n)$ is shown as $(i, j + \frac{1}{2}, k + \frac{1}{2}, n)$.

For instance, FDTD expression of Eq.(3.15) is

$$\frac{\partial E_x}{\partial t} = \frac{1}{\epsilon}\left(\frac{\partial H_z}{\partial y} + \sigma E_x\right)$$

$$\Rightarrow \frac{E_x|_{i,j+\frac{1}{2},k+\frac{1}{2}}^{n+\frac{1}{2}} - E_x|_{i,j+\frac{1}{2},k+\frac{1}{2}}^{n-\frac{1}{2}}}{\Delta t} =$$

$$\frac{1}{\epsilon_{i,j+\frac{1}{2},k+\frac{1}{2}}}\left[\frac{H_z|_{i,j+1,k+\frac{1}{2}}^{n} - H_z|_{i,j,k+\frac{1}{2}}^{n}}{\Delta y} + \sigma_{i,j+\frac{1}{2},k+\frac{1}{2}} E_x|_{i,j+\frac{1}{2},k+\frac{1}{2}}^{n}\right] \tag{3.32}$$

Then Eq.(3.32) is rearranged to obtain $E_x|_{i,j+\frac{1}{2},k+\frac{1}{2}}^{n+\frac{1}{2}}$.

$$E_x|_{i,j+\frac{1}{2},k+\frac{1}{2}}^{n+\frac{1}{2}} = \left(\frac{1 - \frac{\sigma_{i,j+\frac{1}{2},k+\frac{1}{2}} \cdot \Delta t}{2\epsilon_{i,j+\frac{1}{2},k+\frac{1}{2}}}}{1 + \frac{\sigma_{i,j+\frac{1}{2},k+\frac{1}{2}} \cdot \Delta t}{2\epsilon_{i,j+\frac{1}{2},k+\frac{1}{2}}}}\right) \cdot E_x|_{i,j+\frac{1}{2},k+\frac{1}{2}}^{n-\frac{1}{2}} +$$

$$\left(\frac{\dfrac{\Delta t}{\epsilon_{i,j+\frac{1}{2},k+\frac{1}{2}}}}{1+\dfrac{\sigma_{i,j+\frac{1}{2},k+\frac{1}{2}} \cdot \Delta t}{2\epsilon_{i,j+\frac{1}{2},k+\frac{1}{2}}}} \right) \cdot \left[\frac{H_z|^n_{i,j+1,k+\frac{1}{2}} - H_z|^n_{i,j,k+\frac{1}{2}}}{\Delta y} \right] \tag{3.33}$$

3.3 Absorbing Boundry Condition

In order to simulate an infinite open space environment in a finite computational domain, it is obligatory to use boundries which do not reflect electromagnetic waves. If the boundries surrounding the computational domain are not reflectionless, the reflected waves can interfere with the incident or scattered signals. Therefore, accurate and reliable results in free space can not be obtained since the computational domain is not virtually simulating free space. To overcome this problem, absorbing boundry conditions (ABC) are created to absorb electromagnetic waves propagating to the boundries of the computational domain.

In the FDTD code used in this thesis, Enquist-Majda one-way wave equations are utilized to create reflectionless boundries [11]. One-way wave equation is a partial differential equation that allows the propagation of wave in certain directions. Therefore, if this equation is applied to the boundries of the computational domain, the waves impinging on the boundries are absorbed and reflection from the boundries is not observed.

3.4 Discretization in Space and Time

When performing the FDTD computations, numerical dispersion and divergence can occur if the discretization is not done adequately. To achieve appropriate discretization in time and space, stability criteria are applied.

For discretization in space, in order to keep the error in the electric field below 5%, Δx should be [31]

$$\Delta x < \frac{0.9}{k} = \frac{9c}{20\pi f} \tag{3.34}$$

In this thesis, $\Delta x = \Delta y$ is taken as 2.54×10^{-3} m which is in a good aggreement with the criterion in Eq.(3.34) as it is seen in the calculation below

$$\Delta x =< \frac{0.9}{k} = \frac{9c}{20\pi f} \longrightarrow \Delta x = 2.54 \times 10^{-3} < \frac{9 \times 3 \times 10^{8}}{20 \times \pi \times 3.5 \times 10^{9}} = 12.27 \times 10^{-3}$$

The criterion for time discretization, which relates Δt with space increments Δx, Δy and Δz, is the Courant-Friedirchs-Levy (CFL) stability criterion. It can be shown that

$$\Delta t < \frac{1}{c\sqrt{\frac{1}{\Delta x} + \frac{1}{\Delta y} + \frac{1}{\Delta z}}} \tag{3.35}$$

According to Eq.(3.35), if $\Delta x = \Delta y$ in a two dimensional problem, Eq.(3.35) be-

comes $\Delta t < \frac{\Delta x}{c\sqrt{2}}$. Therefore, for spatial increment $\Delta x = \Delta y = 2.54 \times 10^{-3}$ m leads to a criterion as $\Delta t < 5.98 \times 10^{-12}$ s. In this study, Δt is selected as $4.989x10^{-12}$ s, thus, this criterion is satisfied.

3.5 Two-Dimensional Simulations

In this thesis, an FDTD code based on the principles previously mentioned in this chapter is used. The simuluation conducted in this study was designed to simulate the use of ground penetrating radar (GPR) on concrete structures. As mentioned in Chapter 1, GPR scans a structure by transmitting an incident signal to the structure and receiving the scattered electromagnetic waves from the structure while it is moving on a straight line (Figure 3-2).

As seen in Figure 3-2, the GPR antenna transmits and receives signals at one location and then moves to the next location with a spatial increment Δx. Therefore, at each location, the GPR antenna records the amplitude of received signals in the time domain (i.e. E versus time graph). The recorded data are combined to create a two-dimensional (space-time) figure called B-scan image.

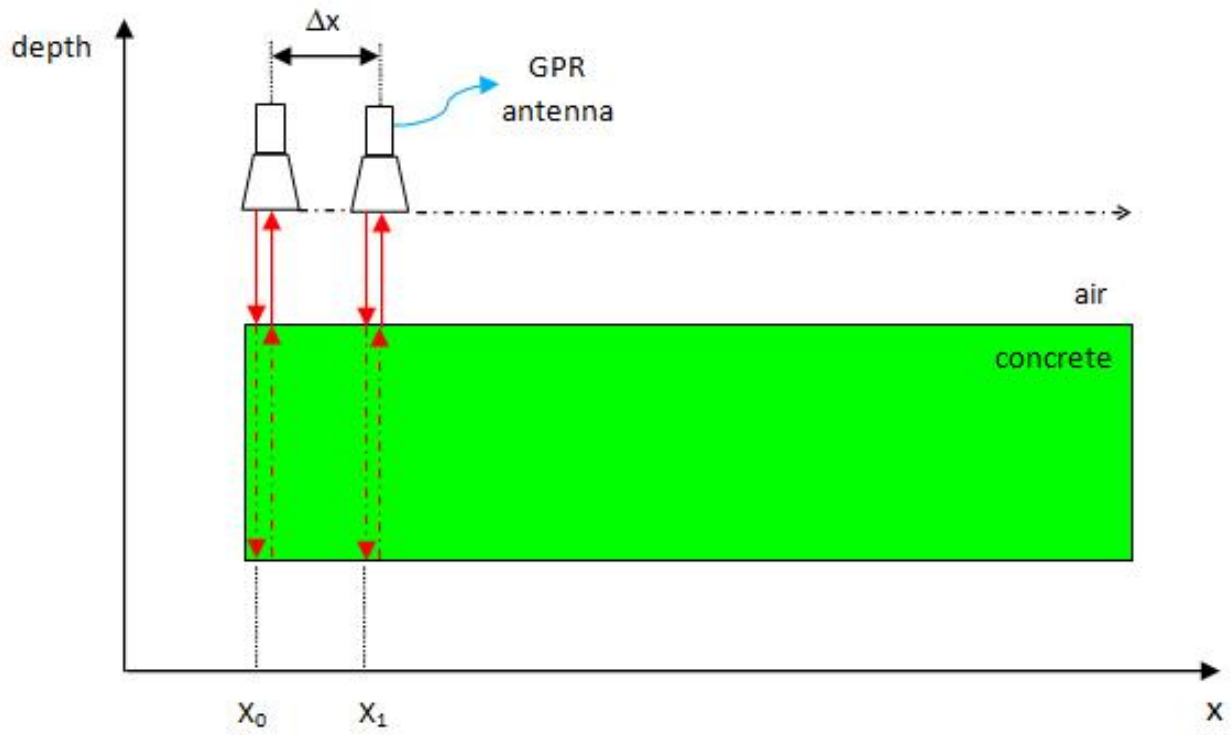

Figure 3-2: Scheme of GPR scan

3.6 Simulation Parameters

The simulation environment was composed of a monostatic radar representing the GPR antenna and a two-dimensional rectangular concrete slab whose dimensions are 1.524m x 0.762m corresponding to 5' x 2.5'. The dielectric constant of the conrete wass assigned as 4 (ϵ_r'=4) and the concrete's relative magnetic permability was defined as 1 (μ_r'=1). On the other hand, conductivity of the concrete was neglected and assumed to be zero (σ=0).

The computational domain was divided into uniform spatial discretization of Δx =

$\Delta y = 2.54x10^{-3}$m= 0.1′ which is in a good agreement with the stability criterion in space. On the other hand, time steps were chosen as $\Delta t = 4.989x10^{-12}$ s satisfying the CFL stability criterion.

The signal exciting the concrete slab was a Gaussian impulse wave with a center frequency of 3.5 GHz. Waveform of the signal is shown in Figure 3-3.

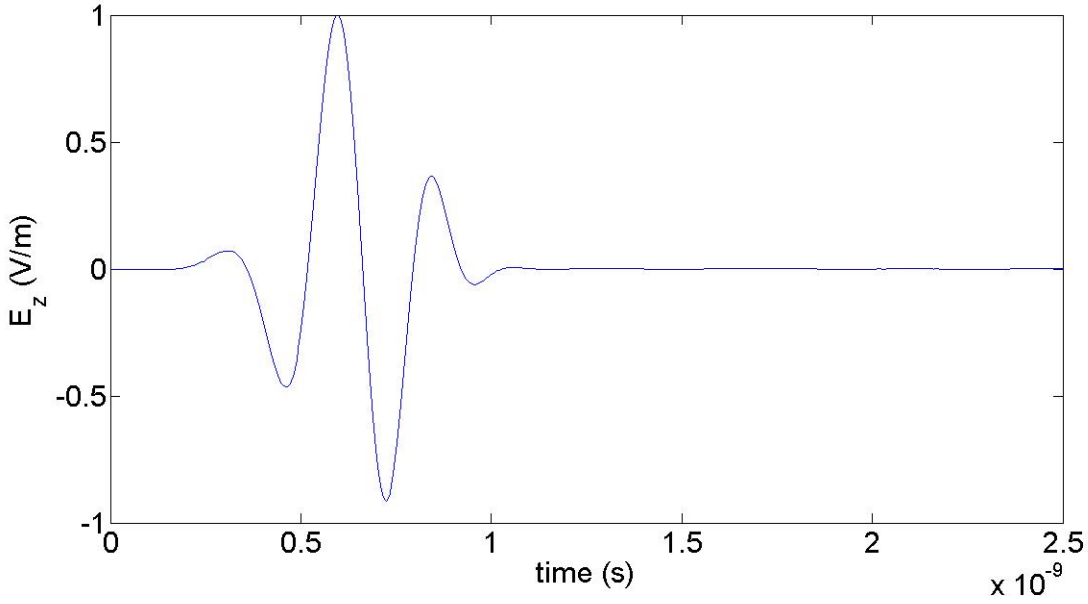

Figure 3-3: Waveform of the excitation signal

3.7 Summary

In this chapter, principles of FDTD methods and simulation parameters are introduced. The main reasons for choosing the FDTD method for simulating the propagation and scattering of electromagnetic waves are the avoidance of numerical instability by providing explicit evaluation of governing equations and its accuracy. On the other hand,

simulation environment and the characteristics of excitation source are introduced at the last section of the chapter.

Chapter 4

Simulation Results

This chapter reports the results of two-dimensional simulations modeling the application of GPR on concrete slabs. The goal of simulation is to detect the line scatterers and to estimate their size. Line scatterers in a concrete slab are considered to represent the delamination, voids and cracking in the concrete structure.

4.1 Simulation Cases

In order to investigate the effects of the line scatterers with different sizes embedded in a rectangular concrete slab from the scattering response, various defect scenerios with different geometries are defined. While the size of the rectangular concrete slab was kept constant in all simulation cases, depth and size of the line scatterers were defined as variables. In Figure 4-1, d is the depth, w is the width and h stands for the height of the delamination. The dimensions of the concrete slab is 1.524 m x 0.762 m and height

of the delamination h is 0.762 cm in all of the simulation cases.

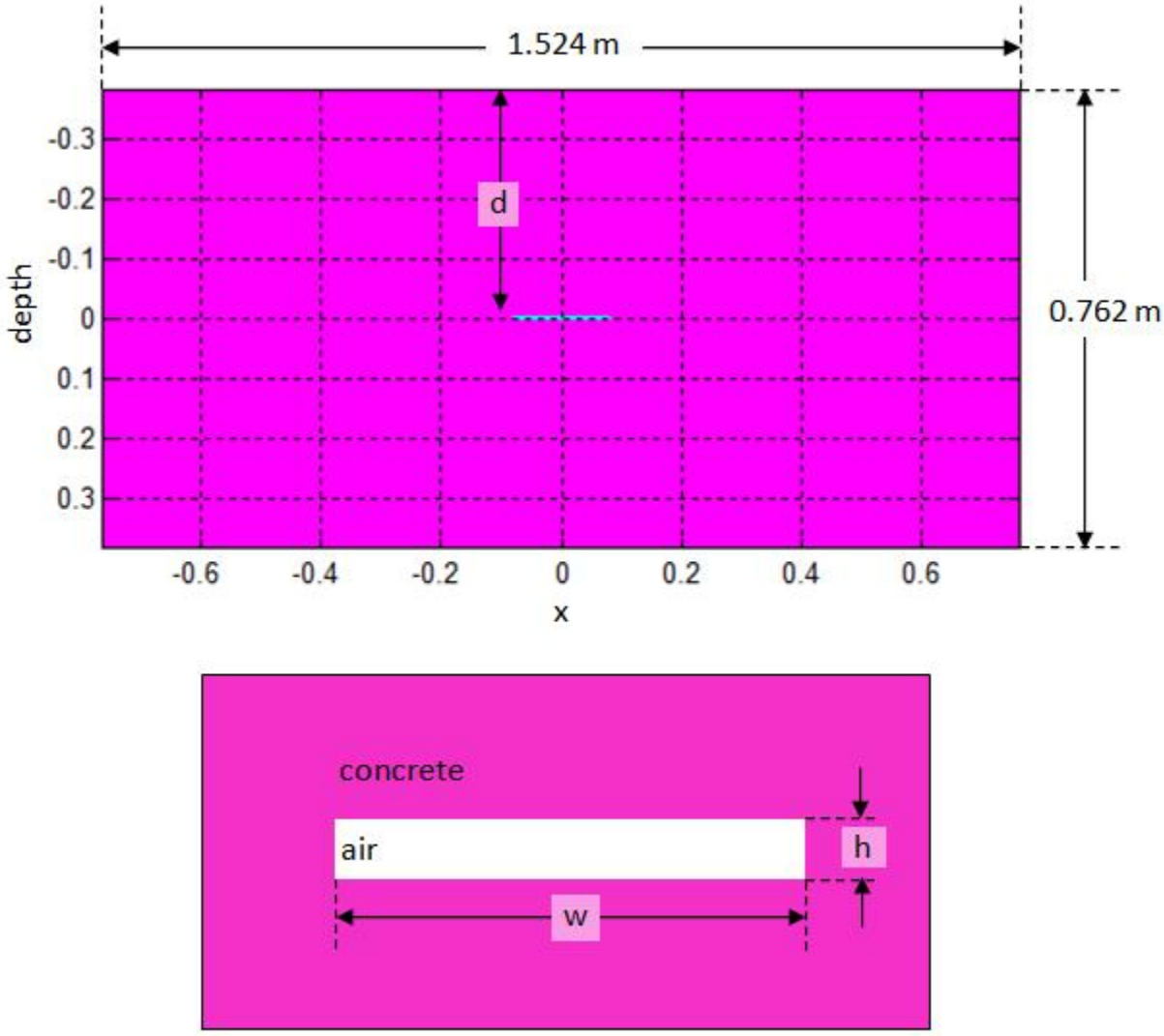

Figure 4-1: Concrete slab with a delamination and the close-up view of the delamination

Different slab types are listed in Table 4.1 according to the depth and the width of delamination inside them.

Simulation Case	d (cm)	d (Δx)	w (cm)	w (Δx)
D149W64	37.846	149	16.256	64
D149W60	37.846	149	15.240	60
D149W56	37.846	149	14.224	56
D149W52	37.846	149	13.208	52
D149W50	37.846	149	12.700	50
D149W48	37.846	149	12.192	48
D149W44	37.846	149	11.176	44
D149W40	37.846	149	10.160	40
D149W36	37.846	149	9.144	36
D149W32	37.846	149	8.128	32
D149W30	37.846	149	7.620	30
D149W28	37.846	149	7.112	28
D149W24	37.846	149	6.096	24
D149W20	37.846	149	5.080	20
D149W16	37.846	149	4.064	16
D149W12	37.846	149	3.048	12
D129W64	32.766	129	16.256	64
D129W48	32.766	129	12.192	48
D129W32	32.766	129	8.128	32
D129W24	32.766	129	6.096	24
D129W16	32.766	129	4.064	16
D129W12	32.766	129	3.048	12
D109W64	27.686	109	16.256	64
D109W48	27.686	109	12.192	48
D109W32	27.686	109	8.128	32
D109W24	27.686	109	6.096	24
D109W16	27.686	109	4.064	16
D109W12	27.686	109	3.048	12
D99W64	25.146	99	16.256	64
D99W12	25.146	99	3.048	12
D89W64	22.606	89	16.256	64
D89W12	22.606	89	3.048	12

Table 4.1: Slab types and geometrical properties of the delamination inside them

4.2 Raw B-scan Images

As defined in Chapter 3, B-scan images are two-dimensional figures which are the time history responses of a monostatic radar scaning the target in a straight line. In Figure 4-2, the B-scan image of a concrete slab with a 3.048 cm-wide delamination at a depth

of 37.846 cm (≅37.8 cm) below the surface of the slab D149W12.

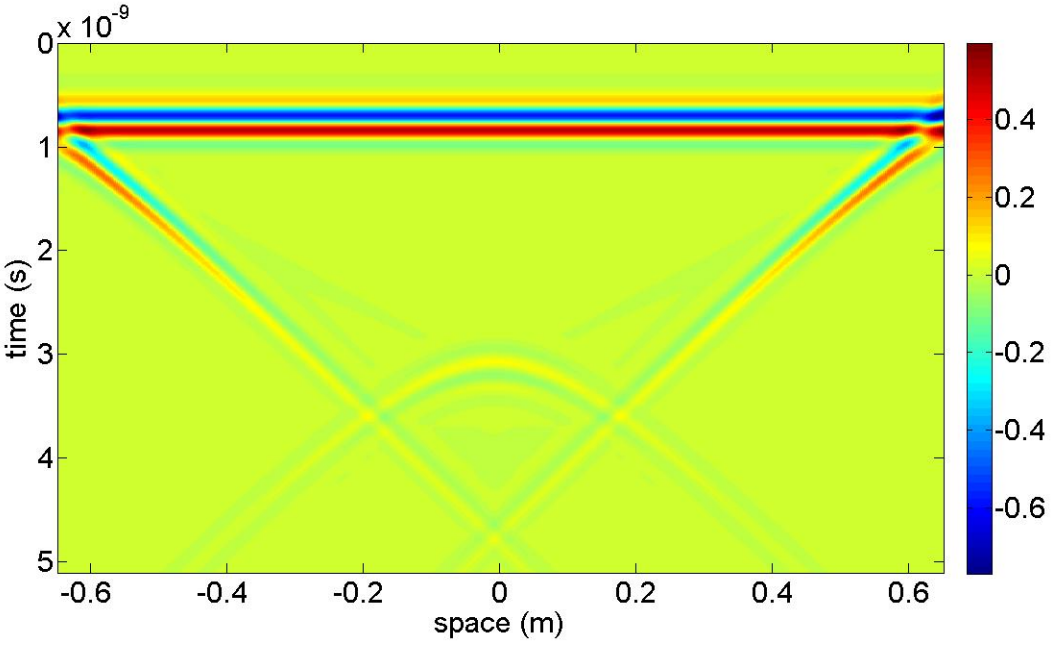

Figure 4-2: Raw B-scan image of concrete slab D149W12

In the B-scan image (Figure 4-2, the horizontal axis represents the direction where radar moves and the vertical axis is time axis. Although the duration of the simulation is 9.96×10^{-9} s=9.96 ns, only a 5.09 ns-long time window is displayed to capture the reflection from the delamination. As seen in the figure, there is a set of horizontal lines between the 0 s and 1×10^{-9} s. This response is due to the strong reflection from the surface of the concrete slab. Moreover, two sets of diagonal lines from the upper corners towards the bottom of the window are also found. These diagonal lines represent the wave scattering from the upper corners of the rectangular slab.

On the other hand, a set of arch-like curves is observed in the B-scan image (Figure

4-2). This arch-like response is due to the delamination inside the concrete slab and is used for the damage detection and size estimation of the delamination in concrete slab.

4.3 Post-Processing of B-scan Images

Since the focus of this study is placed on the reflection response from the delamination (or line scaterer), unrelated or unwanted reflections in the B-scan images must be removed. In order to achieve that, a healthy rectangular concrete slab without any delaminations is defined in the computational domain (Figure 4-3) and used to generate a ”clean” response for background subtraction.

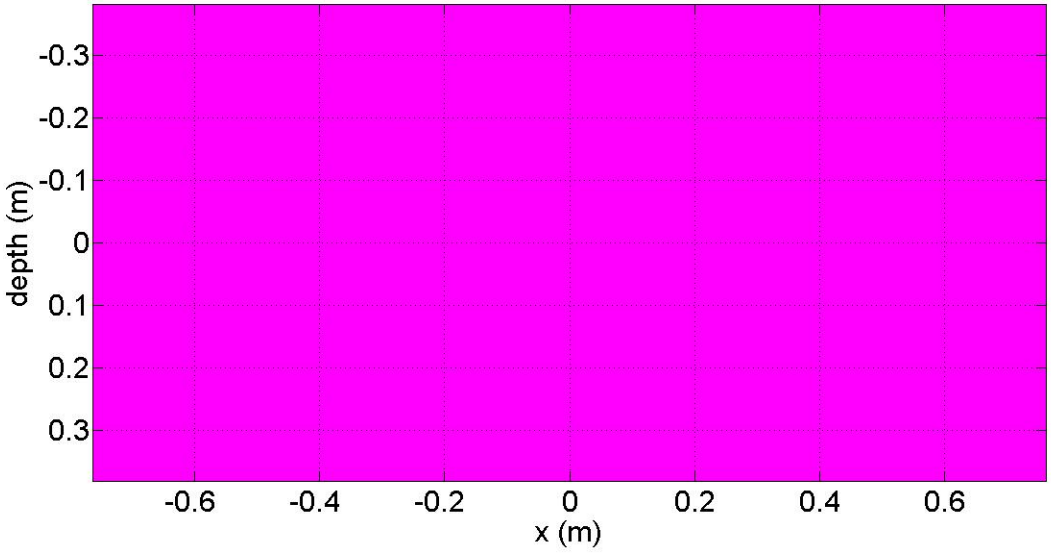

Figure 4-3: Healthy rectangular slab without delamination

The B-scan image of the healthy slab without no delamination is shown in Figure 4-4. The reflection from the slab surface and the scattering from the slab corners are clearly seen in the B-scan image of slab D149W12.

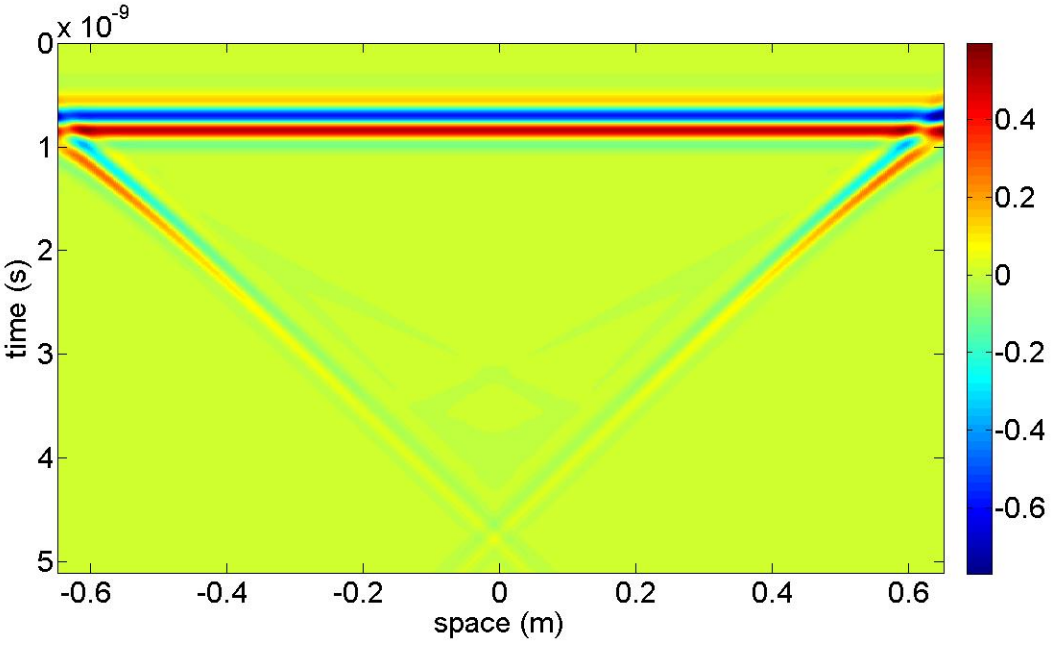

Figure 4-4: B-scan image of healthy rectangular slab having no delamination

Finally, the output image used to construct the B-scan image of healthy slab is subtracted from the output image of the slab D149W12, in order to reveal the reflection signal from the delamination (Figure 4-5). The same procedure is applied to all other slabs in this study.

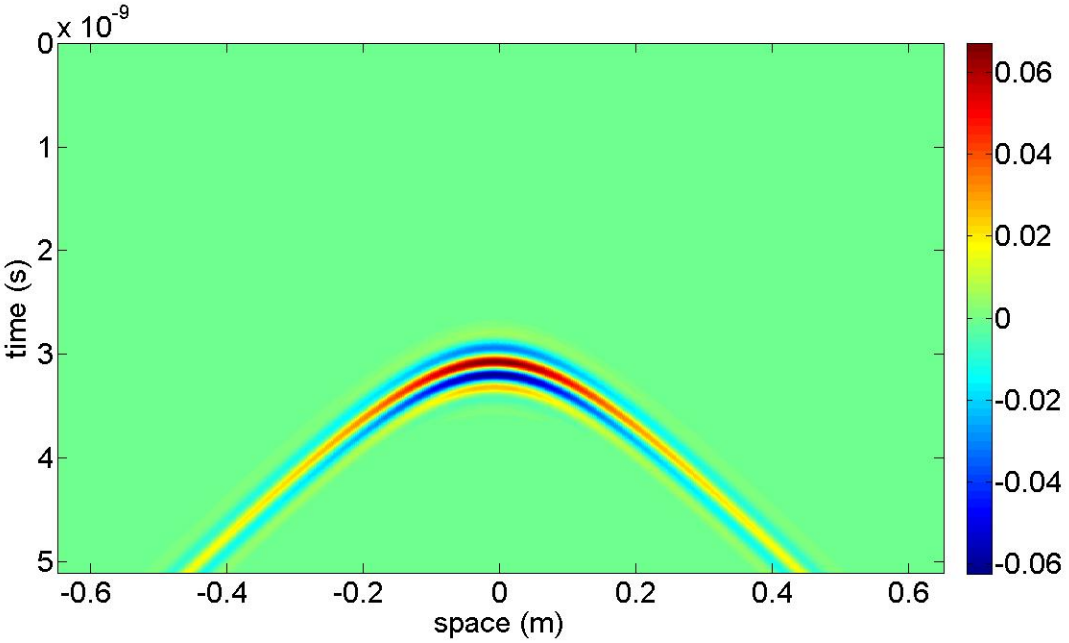

Figure 4-5: Clean B-scan image of slab D149W12

4.4 Interpretation of the B-scan Images

As a known fact, electromagnetic waves are sensitive to the variations in the dielectric properties of the medium in which they propagate. For instance, consider an electromagnetic wave propagating in a medium. When the wave encounters another medium with a different dielectric constant, part of the wave transmits through the next medium, while part of the wave is reflected back (Figure 4-6).

In the simulation cases in this thesis, the dielectric constant of concrete is taken as 4 ($\epsilon_r = 4$). Considering the fact that the dielectric constant of air is 1 ($\epsilon_r = 1$), reflection of electromagnetic waves is expected at the concrete-air interface, i.e. at the boundries of the delamination embedded in the concrete slab. In the B-scan image, the reflection due to delamination is clearly observed, as an evidence to verify the detection of the

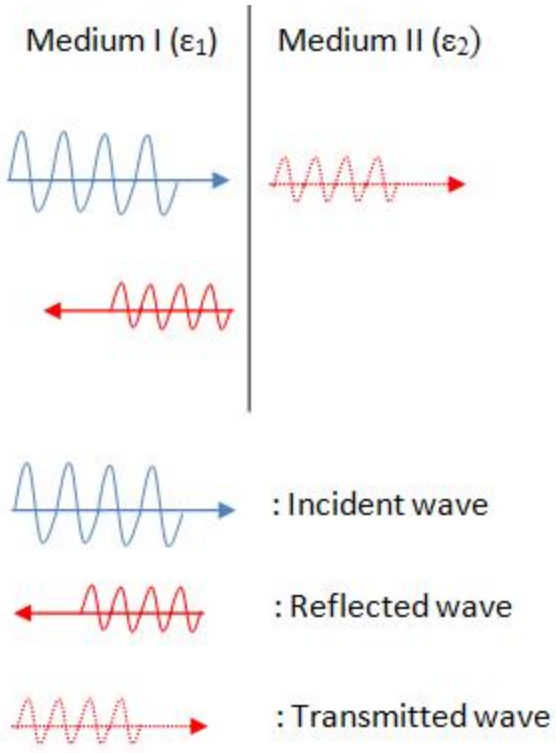

Figure 4-6: Reflection and transmission of an incident wave

delamination inside concrete.

To show the effect of dielectric properties on electromagnetic propagation and B-scan images of concrete slab, dielectric constant of concrete is changed to be 6 ($\epsilon_r = 6$) in slab D149W12. The raw B-scan image of slab D149W12 (dielectric constant of concrete 6) is shown in Figure 4-7. If Figure 4-2 and Figure 4-7 are compared, it is observed that the time required to receive the reflection from delamination is longer in Figure 4-7 than in Figure 4-2. It is because higher the dielectric constant slower the electromagnetic wave speed in a medium.

On the other hand, when the radar is located further away from the delamination,

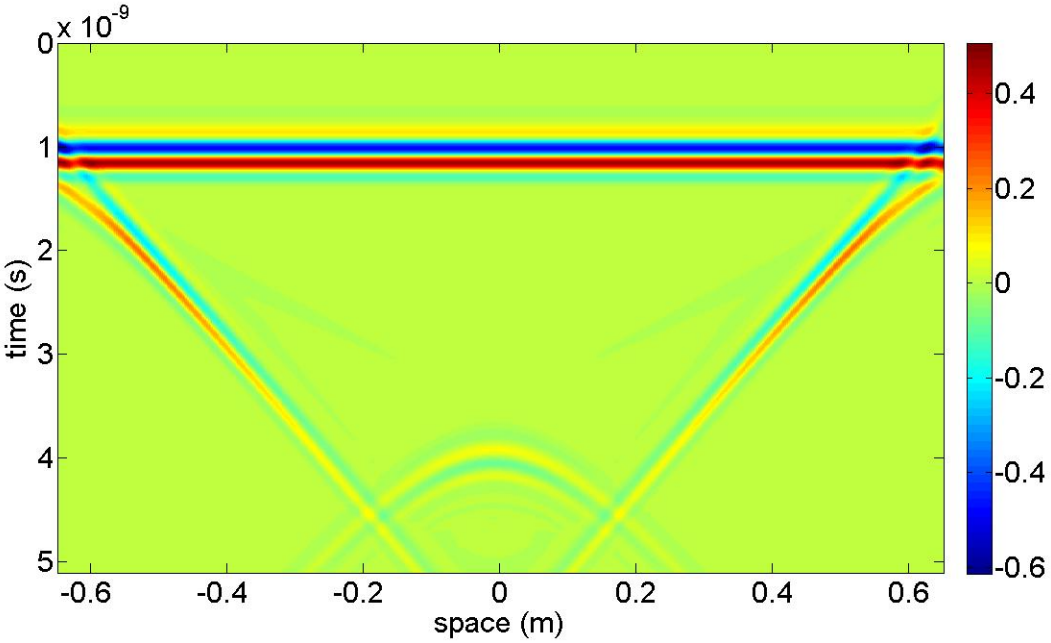

Figure 4-7: Raw B-scan image of slab D149W12 with a dielectric constant of 6

the time required to receive the scattered signal becomes longer. In other words, the longer the distance between radar and scatterer, the later the signal to be received. For example, in Figure 4-5, while going far away from the center (x = 0 m) in the x axis, the time required to receive the signal increases, because the radar is closer to the delamination when it is located at the center rather than when it is located away from the center. This is why an arch-like response is formed and observed.

4.5 Estimation of the Delamination Size

4.5.1 Conversion of the Scattering Response to the Curve Shapes

As concluded, a linear scatterer (delamination) creates an arch-like response in the space-time plane of the B-scan image. To further analyze this response, the arch-like shape consisting of several layers (in terms of the amplitude of the signal) needs to be converted to a simple curve for interpretation. In order to achieve that, a window (red rectangle) is defined on the B-scan image as shown in Figure 4-8.

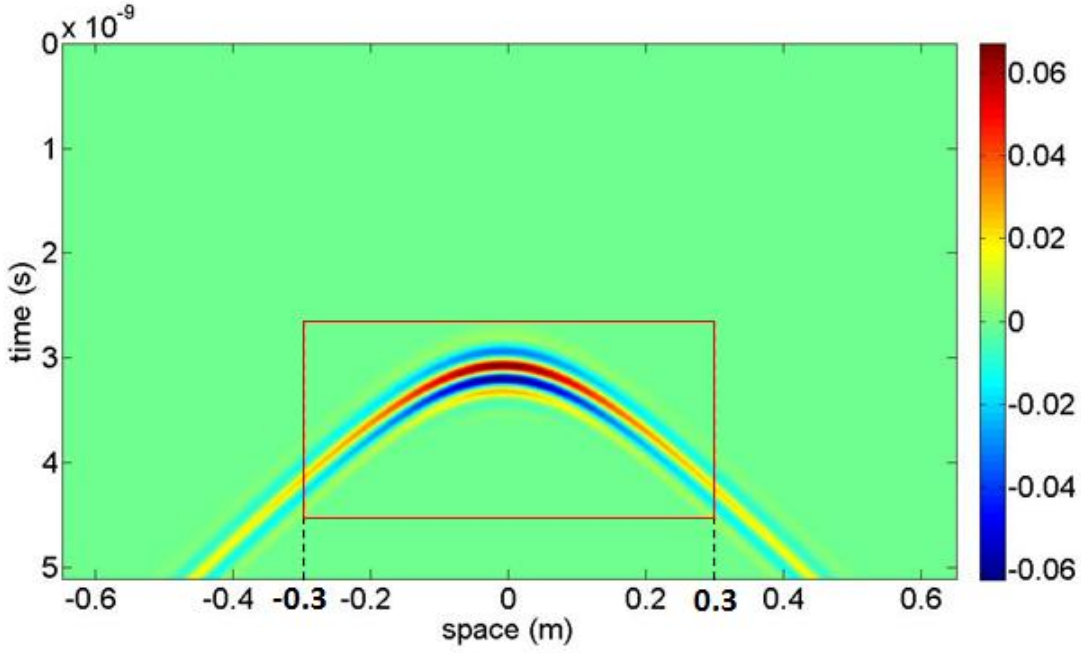

Figure 4-8: The window defined on the B-scan image of slab D149W12

As seen in Figure 4-8, width of the window is 60 cm (238Δt), however the height of the window is not constant for all simulation cases since it needs to be readjusted to capture the arch-like response in the range of -30 cm to 30 cm. As the next step, the window is divided into vertical columns whose width is Δt. Then, each vertical column

is scanned to find out the location of maximum amplitude (i.e. the amplitude in the z direction). Finally, these points are combined in another figure to compose a curve shape in the space-time plane (Figure 4-9). In the figure, t and x axis are demonstrated in terms of unit lenghts (Δt and Δx).

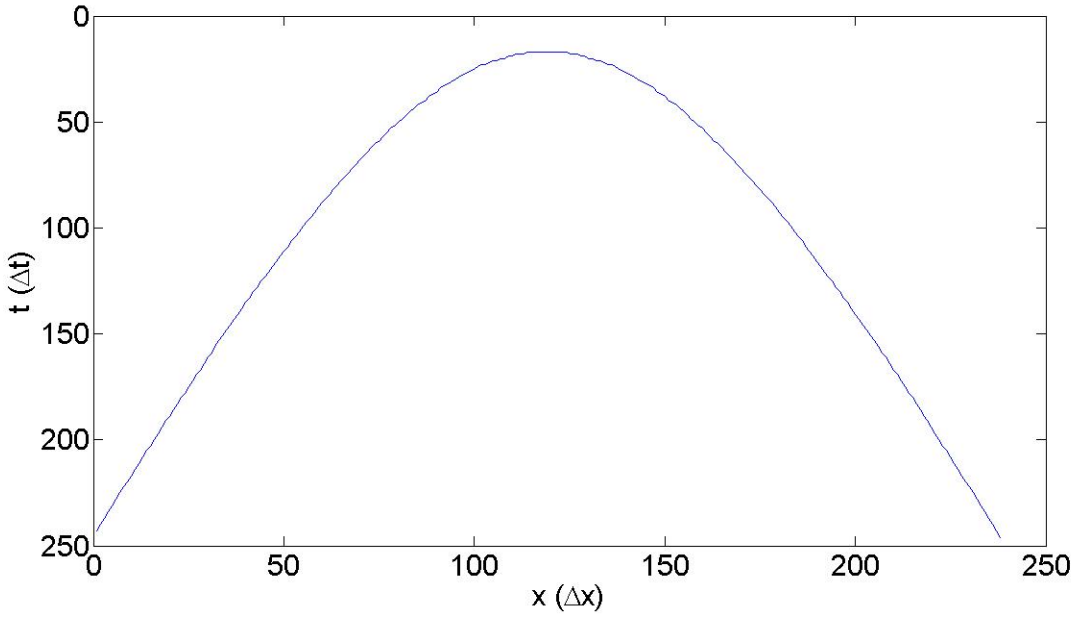

Figure 4-9: The combination of the maximum amplitude points on the window of the B-scan image of slab D149W12

Even though the curve is constucted, at the certain points of the curve, ripples are found and need to be removed for the future processing of the curve (Figure 4-10). The problem is overcome by applying a low-pass filter four times to the data points of the curve. Filtering equations are

$$t'(x) = \frac{t(x) + t(x+1)}{2} \tag{4.1}$$

$$t''(x) = \frac{t'(x) + t'(x+1)}{2} \tag{4.2}$$

$$t'''(x) = \frac{t''(x) + t''(x+1)}{2} \tag{4.3}$$

$$t''''(x) = \frac{t'''(x) + t'''(x+1)}{2} \tag{4.4}$$

where $t(x)$ is the point which is x away from the starting point of the curve.

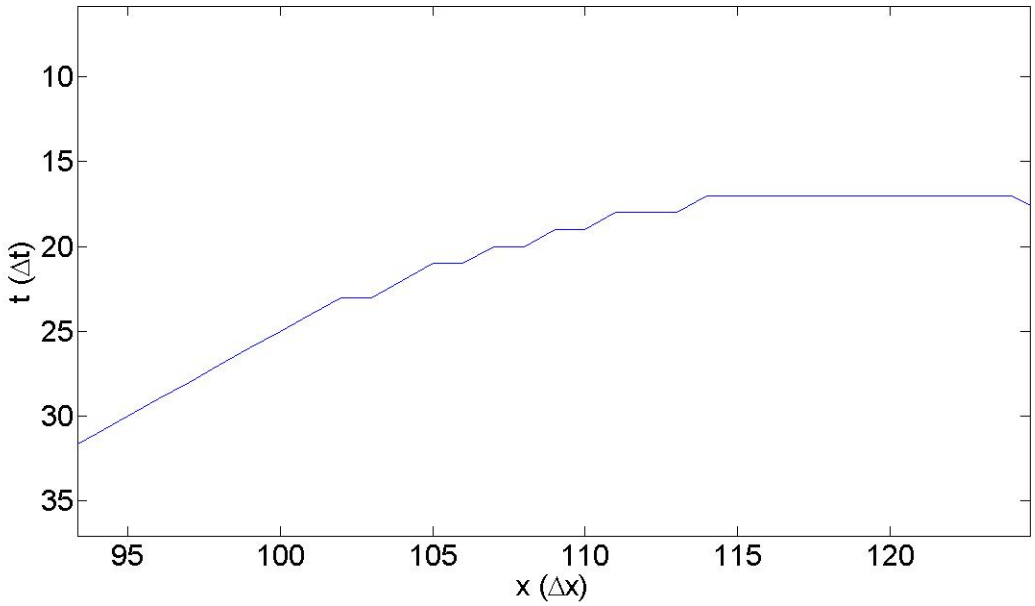

Figure 4-10: Ripples on the curve

The smoothened ripples after the application of the low-pass filter is shown in Figure 4-11

4.5.2 Curvature Calculations

Curvature (k) is defined as the reciprocal of the radius of curvature (r) or, $k = \frac{1}{r}$. In order to calculate the radius of curvature or the curvature of a line, coordinates of at

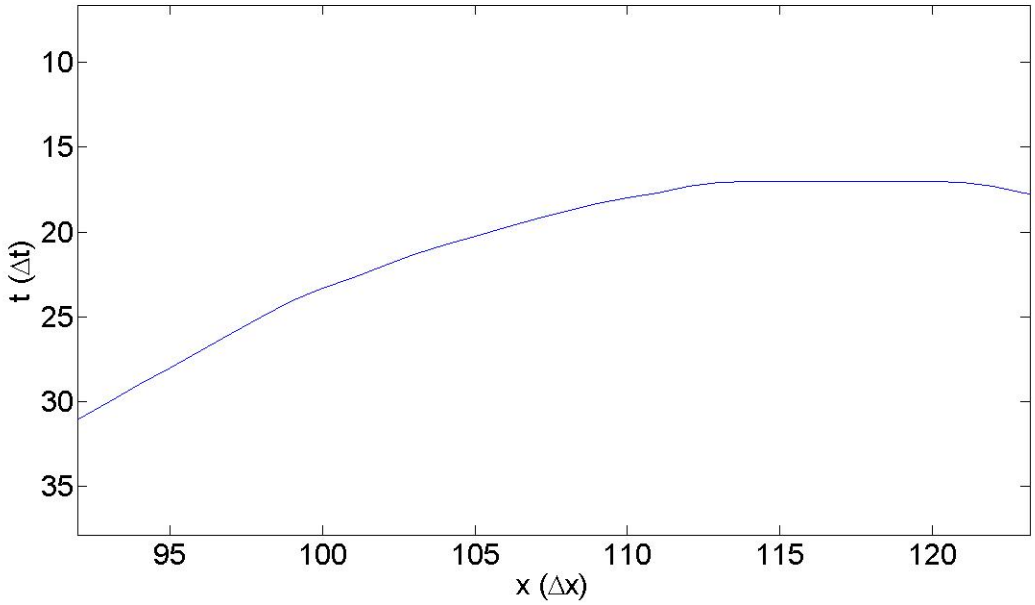

Figure 4-11: Smoothened ripples after filtering

least three points on that line are needed. This is because a circle can be defined by at least three points. Figure 4-12 shows a circle passing through three points of a curve similar to the curves produced from the B-scan images. In Figure 4-12, r corresponds to the radius of curvature calculated by the coordinates of Point 1,2 and 3.

Curvature of the curves representing the scattering response of delamination is calculated using the same technique. The peak point of the curve is selected as the pivot point (x_c, y_c) and the other two points are selected by moving a certain distance (x_d) away from the pivot point both towards the x and -x directions (Figure 4-13).

Calculated curvature values for the curves which are the reflection response of various delaminations with different widths ($12\Delta x$ to $64\Delta x$) at 0.378 m depth is shown in Figure 4-14. As shown in Figure 4-14, for small x_d values, curvature values are significantly fluctuating because of the linear peak values of the curves. However, the

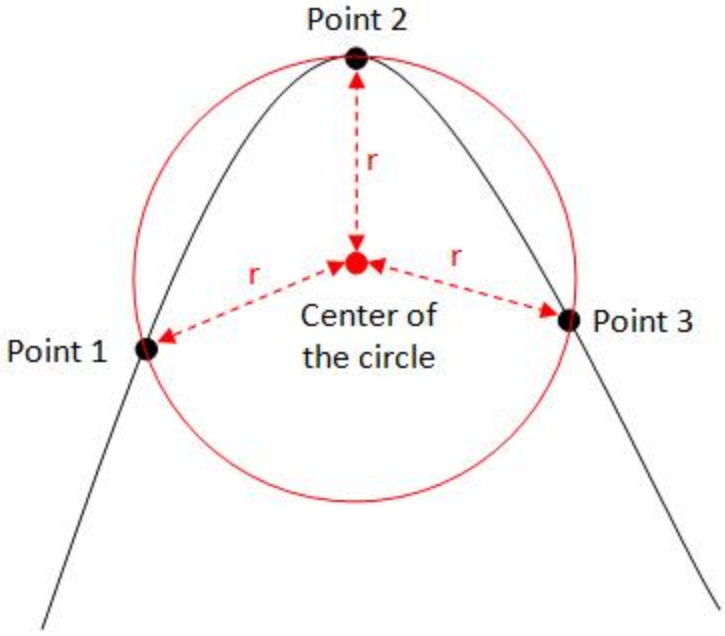

Figure 4-12: The circle passing through the three points of a curve

curvature values show a settled behavior at high x_d values (Figure 4-15).

As seen from Figure 4-15, for a specific x_d value, when the curvature increases, the width of the delamination increases.

4.5.3 Relationship Between the Curvature and the Width of Delamination

In order to relate the curvature of arch-like shapes in the B-scan image to the width of delamination embedded inside the concrete slab, it is decided to examine the curvature value as an indicator. In this thesis, the curvature values are evaluated at $x_d = 116$ which corresponds to approximately 30 cm away from the peak of the arch-like shape (i.e. center of the delamination).

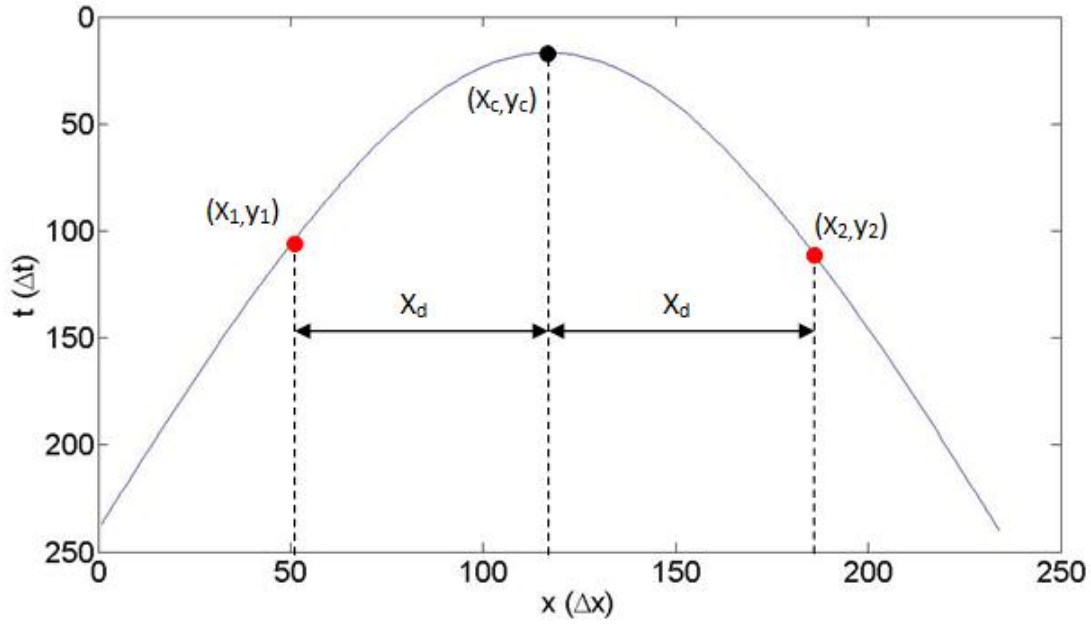

Figure 4-13: Demonstration of the selection of three points on the curve response of slab D149W12

Then, the smallest delamination width, 12Δ*x* is chosen as the reference size. The curvature value of the 12Δ*x*-wide delamination is subtracted from the curvature values of wider delaminations in order to plot the difference in the figure of curvature value versus relative width of the delamination (with respect to 12Δ*x*-wide delamination).

For example, Figure 4-16 shows the curvature difference versus relative width graph for various delaminations at a depth of 37.8 cm from the concrete surface.

As another example, same procedure is applied to the delaminations at a depth of 27.6 cm from the concrete surface (Figure 4-17).

As seen from the Figure 4-16 and Figure 4-17, the relationship between the difference in curvature values of different delaminations and the relative width of delaminations is almost linear, regardless of the depth of delamination. In other words, while the

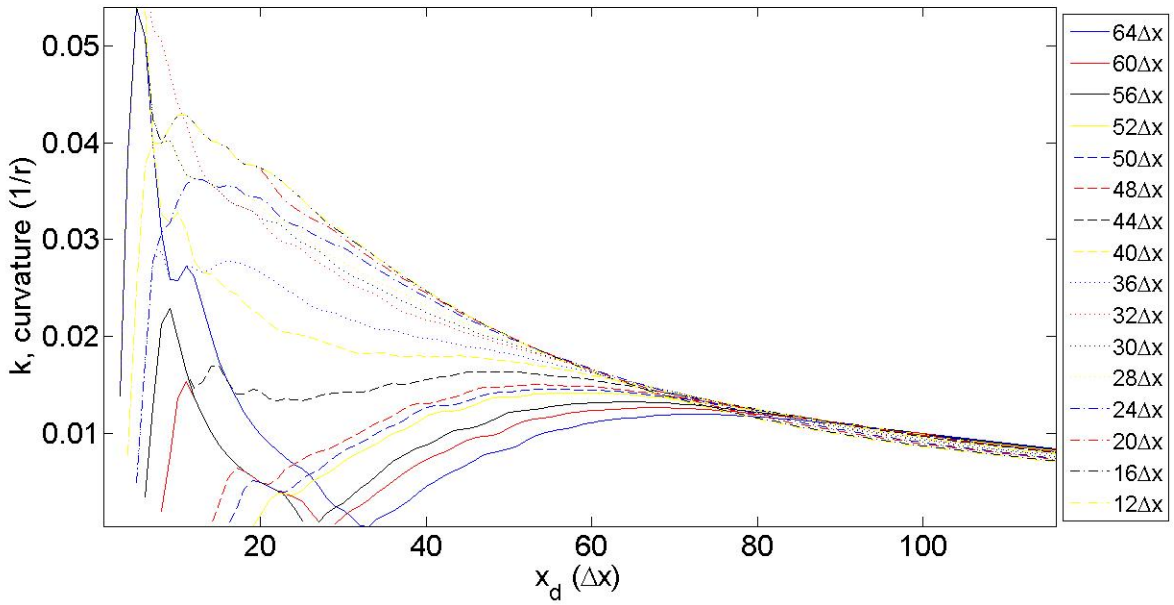

Figure 4-14: Curvature values of various widths of delaminations at 0.378m depth with respect to x_d

difference in curvature values increases, almost a linear increase in the corresponding relative width of the delaminations is observed.

Then, a line connecting the first and the last data points in Figure 4-16 is drawn to calculate the slope of the line (Figure 4-18). The same procedure is applied to the delaminations at different depths and the slopes of these lines are compared as shown in Figure 4-19.

As seen from Figure 4-19, the slope values for different delamination depths do not vary significantly. Therefore, the data set of delaminations at 37.8 cm depth can be used for further analysis.

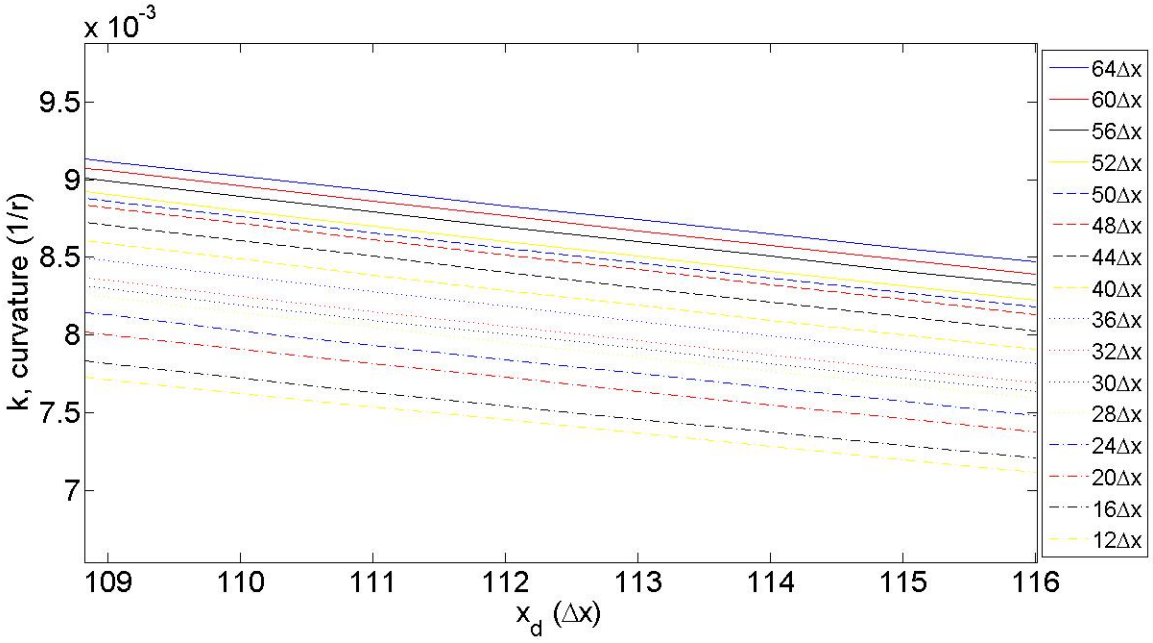

Figure 4-15: Curvature values of various widths of delaminations at 37.8cm depth at higher x_d values

4.5.4 Curve Fitting to Results and Error Calculatons

In order to interpret and to generalize the results in Section 4.5.2, linear, quadratic and cubic curves are used in the curve fitting of the ”difference in the curvature versus relative width of the delamination” graph. As mentioned before, delaminations at 37.8 cm depth are chosen as the representative of other delaminations at different depths. On the other hand, relationships found in Section 4.5.2 and this section depend on the curvature values calculated at $x_d = 116\Delta x (\cong 30$ cm). Results of the curve fitting are reported in the following.

1. Linear Fitting

As the first model of curve fitting, a line connecting the first and the last data

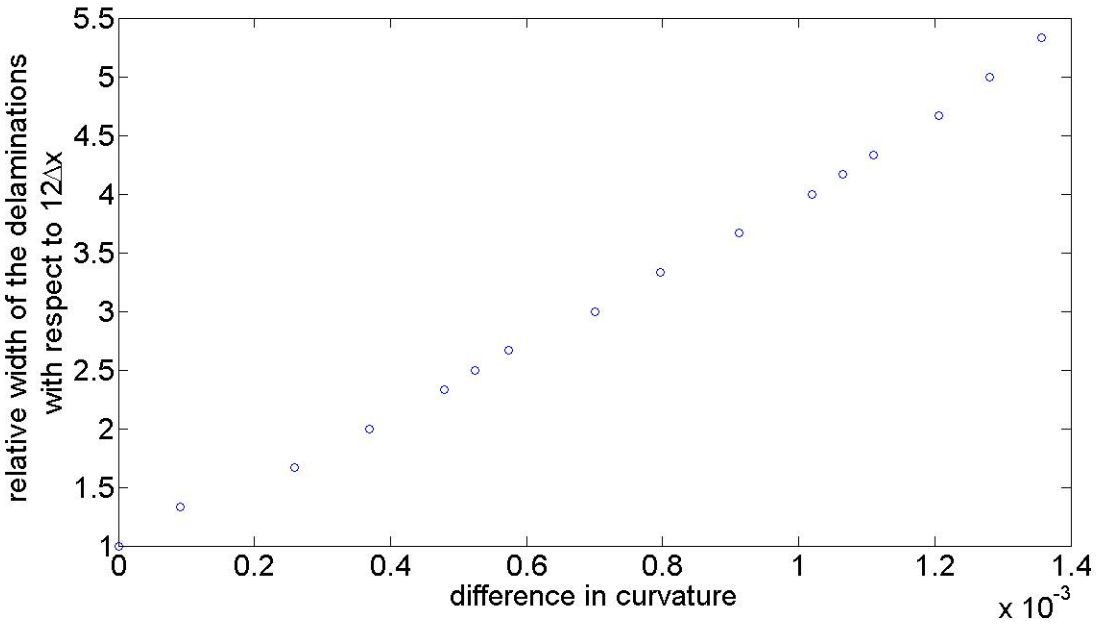

Figure 4-16: Difference in curvature values versus relative width of the delaminations at 37.8cm-deep

points of the ”difference in the curvature versus relative width of the delamination” graph is drawn in (Figure 4-20) and it is called ”easy fit line” in this thesis.

Although, easy fit line represents exactly the first and the last data points, it deviates from other data points. Equation of the easy fit line is

$$W_r = 3193 \times \Delta k + 1 \tag{4.5}$$

where W_r is the relative width of delamination and Δk is the difference in the curvature values with respect to the curvature value of $12\Delta x$-wide delamination.

On the other hand, a ”best fit line” which statistically provides the minimum standard deviation is drawn and shown in Figure 4-21.

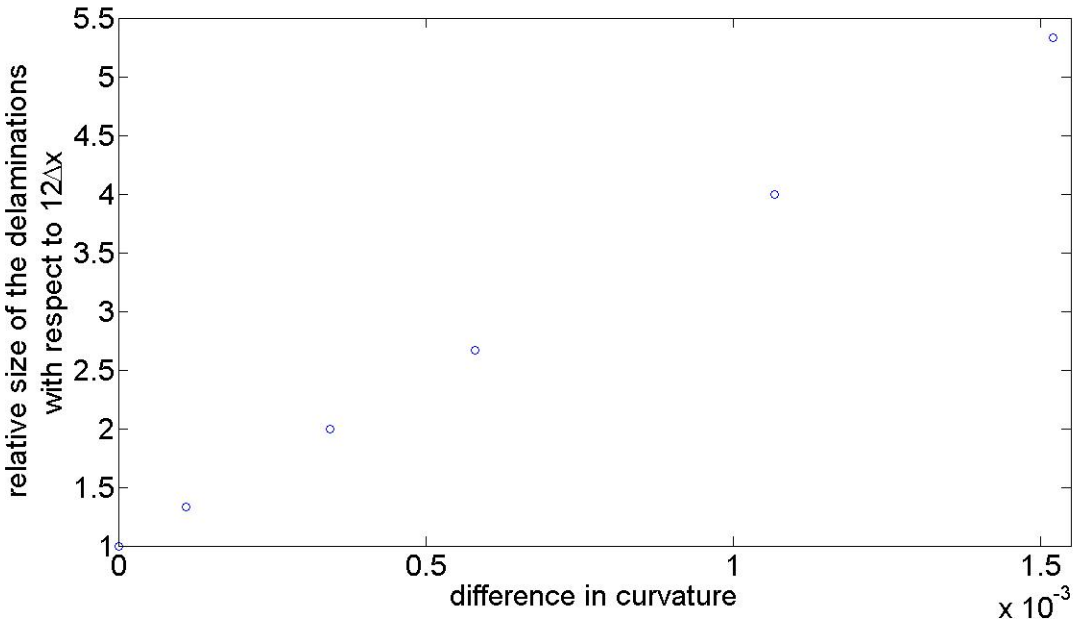

Figure 4-17: Difference in curvature values versus relative width of the delaminations at 27.6cm-deep

The equation of the best fit line is

$$W_r = 3124 \times \Delta k + 0.89 \tag{4.6}$$

Even though the result of the best fit line is very good, the line intersects with the y-axis at 0.89 instead of 1 which is not tolerable for the interpretations. In order to overcome this problem, another linear fitting is applied. The equation of the new line called ”optimized line” is

$$W_r = m \times \Delta k + 1 \tag{4.7}$$

In Eq.(4.7), the second term on the right side of the equation is set to be 1 in order

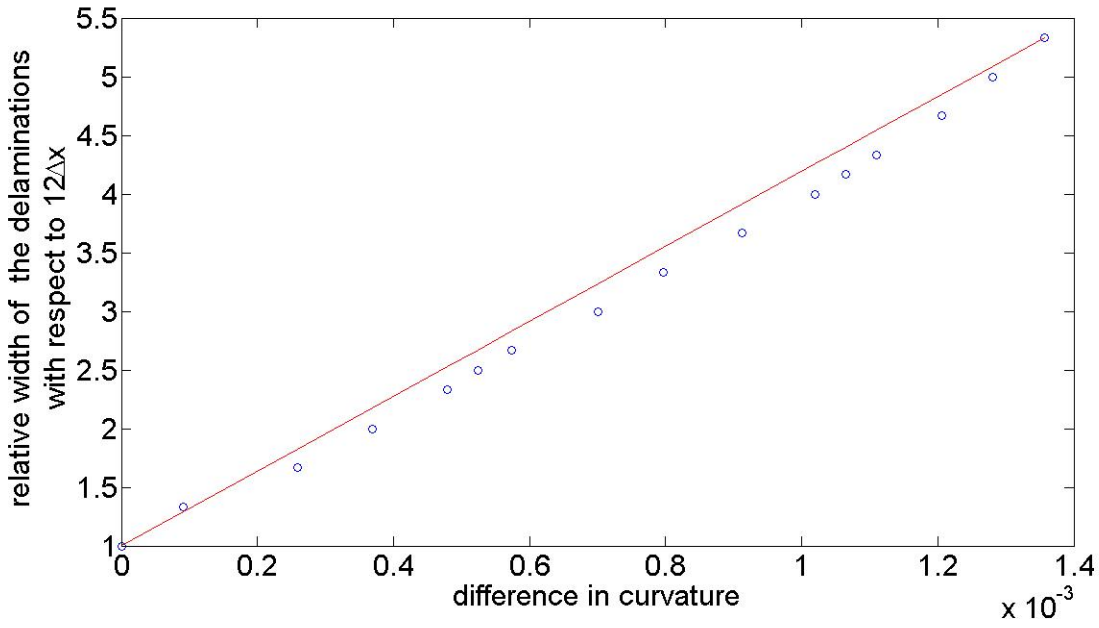

Figure 4-18: The line connecting the first and the last data point for the delaminations at 37.8 cm-deep

to force the line to intersect with the y-axis at 1 and the coefficient (m) represents the slope of the line. Slope (m) is defined as a variable in order to find the line that provides the minimum standard deviation. The lines having various slopes are shown in Figure 4-22.

Then, the standard deviation of these lines are calculated and shown in Figure 4-23. As seen from Figure 4-23, the minimum standard deviation value is associated with the line with a slope of $m = 2950$. Therefore, the equation of the "optimized line" is

$$W_r = 2950 \times \Delta k + 1 \tag{4.8}$$

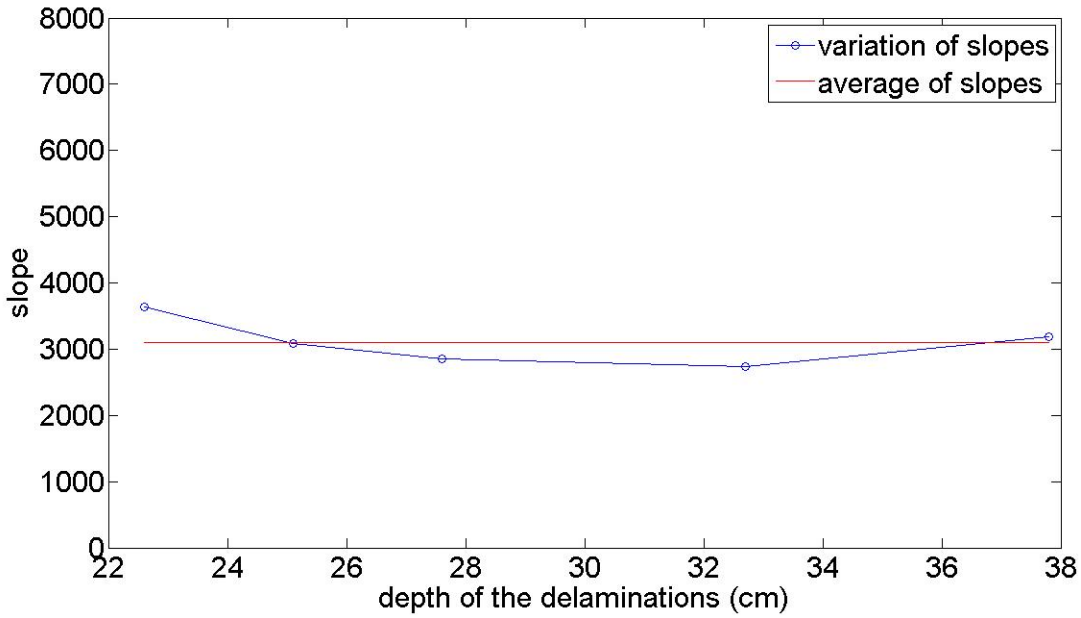

Figure 4-19: Slopes of the lines connecting the first and the last data point for delaminations at different depths

2. Quadratic and Cubic Fitting

If better approximations are desired, quadratic and cubic polynomials are needed instead of linear fitting. Figures 4-24 and 4-25 show the quadratic and cubic polynomials fitted to the data. As shown in Figures 4-24 and 4-25, there is no significant difference in the ploynomial fitting results of quadratic and cubic polynomials. On the other hand, neither quadratic nor cubic polynomial intersects the y-axis at 1 as in the case of easy fit line. Eqs.(4.9) and (4.10) provide the equations of the quadratic and cubic polynomials.

$$W_r = 4.967 \times 10^5 \times \Delta k^2 + 2435 \times \Delta k + 1.047 \qquad (4.9)$$

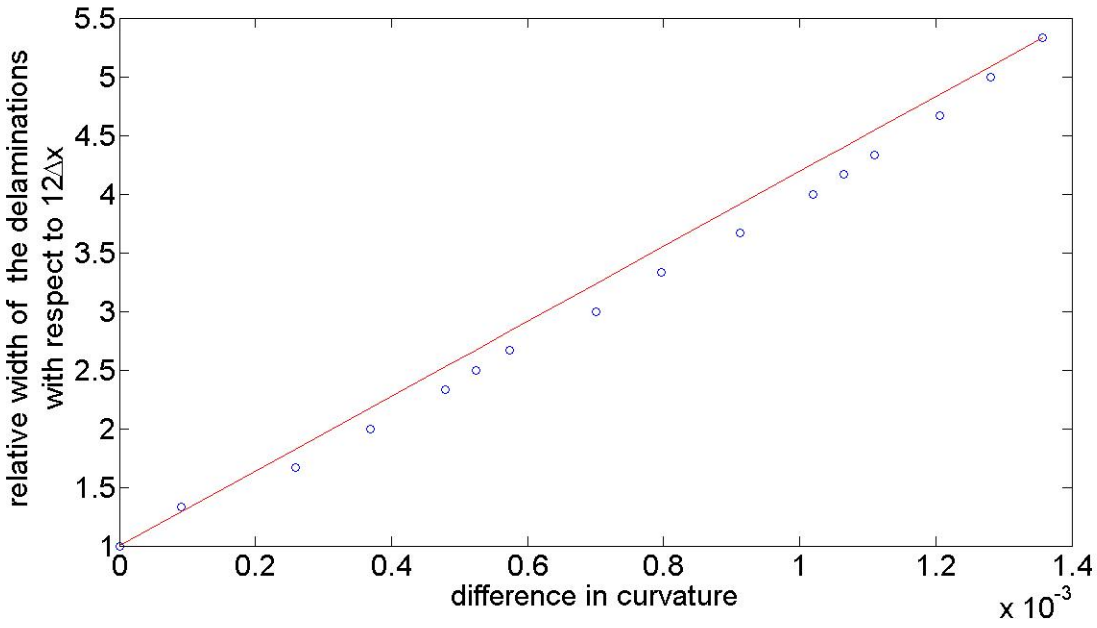

Figure 4-20: Easy fit line

$$W_r = 3.719x10^8 \times \Delta k^3 - 2.553x10^5 \times \Delta k^2 + 2825 \times \Delta k + 1.013 \qquad (4.10)$$

3. Error Calculations

In this section, error is defined to be the absoulute difference between the y coordinate of actual data and the y coordinate of fitted line or polynomials. In other words, error is the deviation of the fitted line or polynomials from the data points in the corresponding relative width values. The fitted line and polynomials are compared in terms of error percentages for each relative width value in Figure 4-26. As seen from Figure 4-26, the easy fit line and the best fit line are the most erroneous approximations to the data. On the other hand, although the error percantages of the quadratic and cubic polynomials are lower than the ones of the

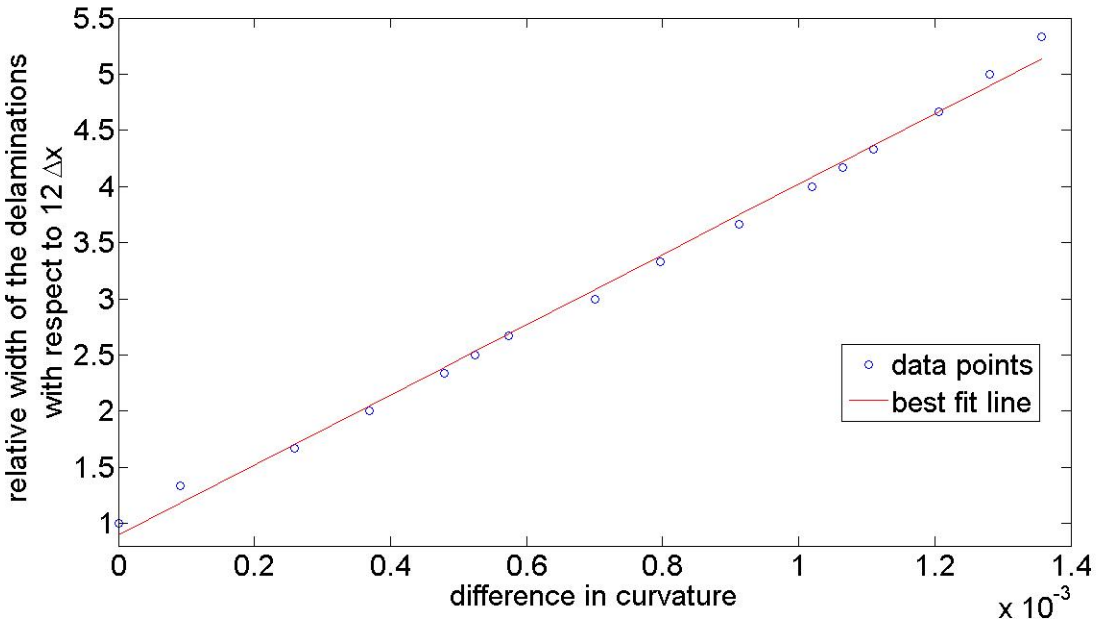

Figure 4-21: Best Fit Line

optimized line, they deviate at the first point where the relative width value is set to be 1. The cumulative error percantages are shown in Figure 4-27. While the highest cumulative error is associated with the easy fit line, the best approximation to the data is the cubic polynomial. As a result of error calculations, it is found that higher order fitting techniques are generally more accurate than linear fitting techniques. Therefore, the cubic polynomial can be used due to its best approximation and relatively small deviation at the first point. Although the error percentages associated with the optimized line is higher than the ones associated with the polynomials, the optimized line can also be used because it does not deviate at the first point and it is superior than other linear approximations.

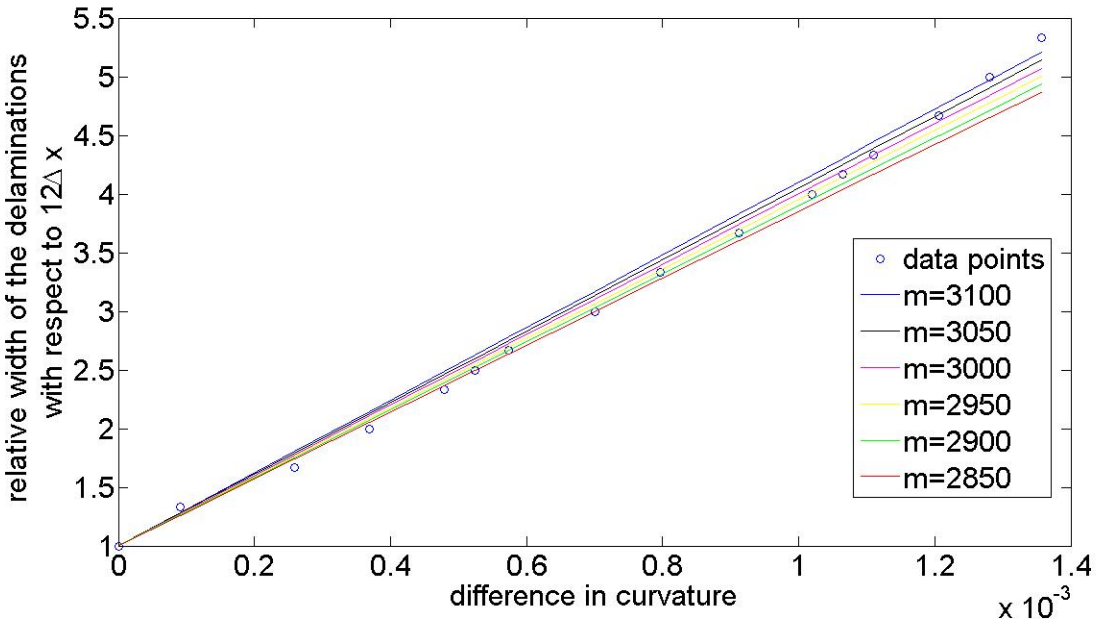

Figure 4-22: Curve fitted lines with various slopes, m

4.6 Summary

In this chapter, results of numerical simulation and their post-processing steps are reported. Concrete slabs with different types of delaminations (with various widths and at different depths) are modeled. Detection of delamination in the subsurface of a concrete slab with different dielectric properties is shown using B-scan images. Extracting the arch-like shape of reflection due to delamination from B-scan figures, the curvature (k) values of the shapes are calculated. Relationship between the difference in curvature values of delaminations with different widths and relative width of delamination is illustrated to be almost linear, regardless the depth of delamination. After the application of different curve fitting models, it is concluded that this relationship can be best represented by either a line (optimized line) or a cubic polynomial.

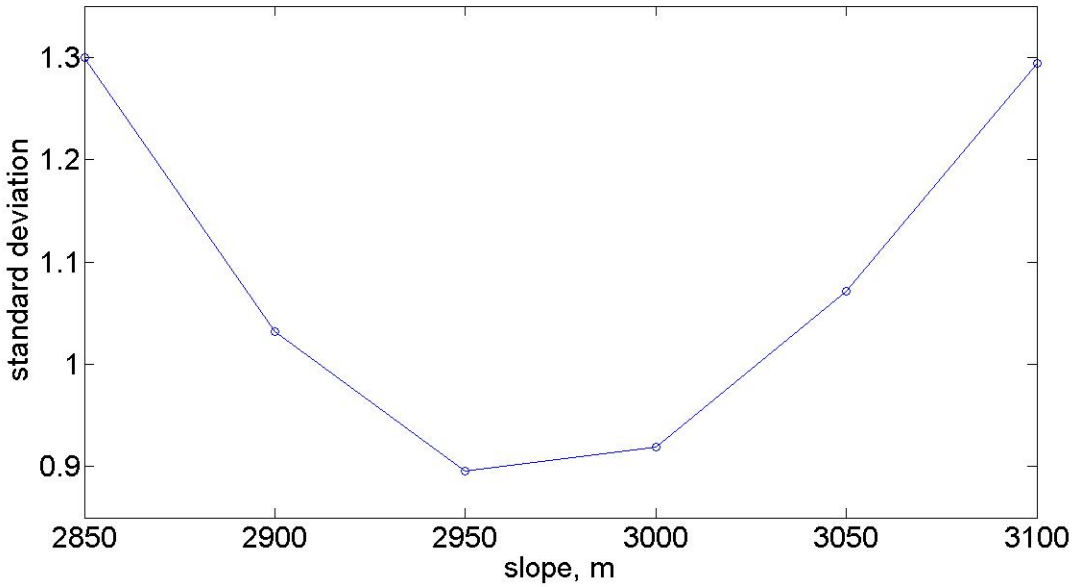

Figure 4-23: Standard deviation of lines with various slopes, m

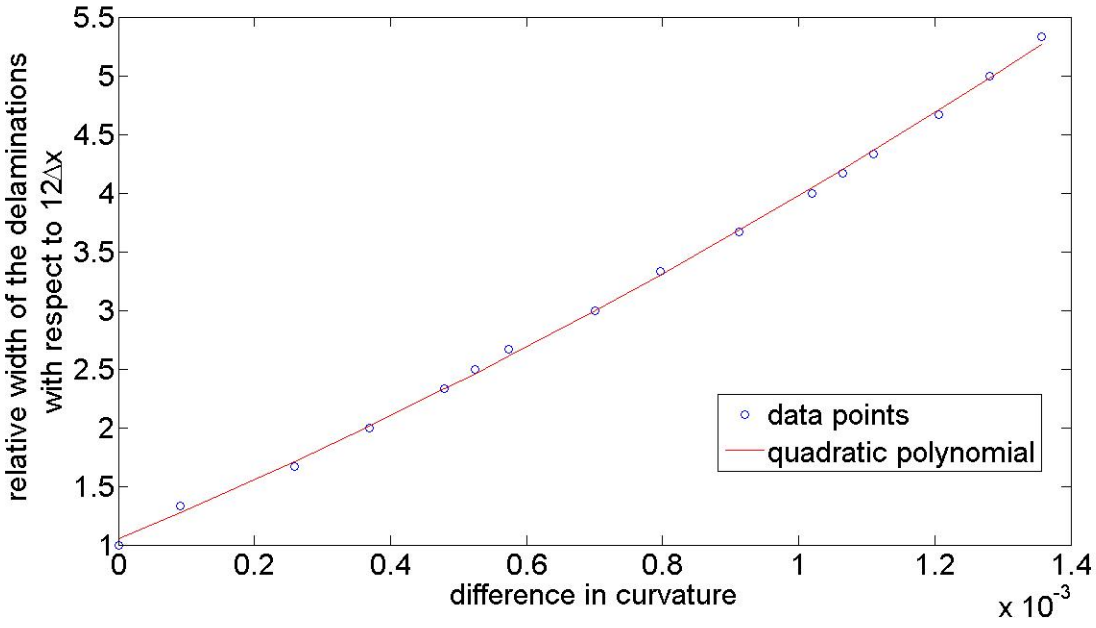

Figure 4-24: Fitted quadratic polynomial

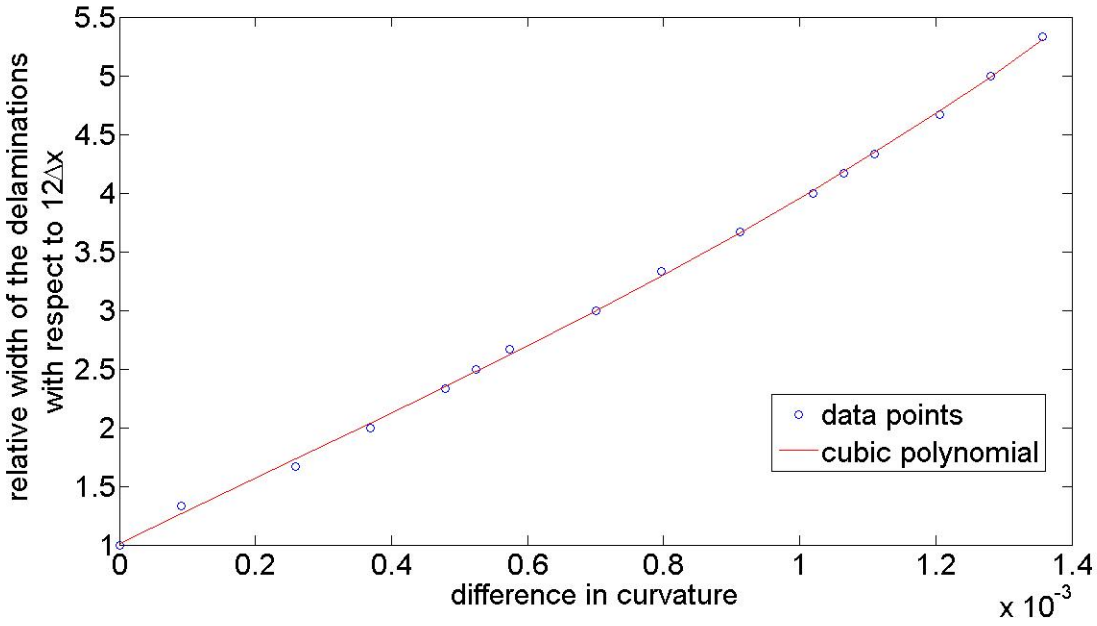

Figure 4-25: Fitted cubic polynomial

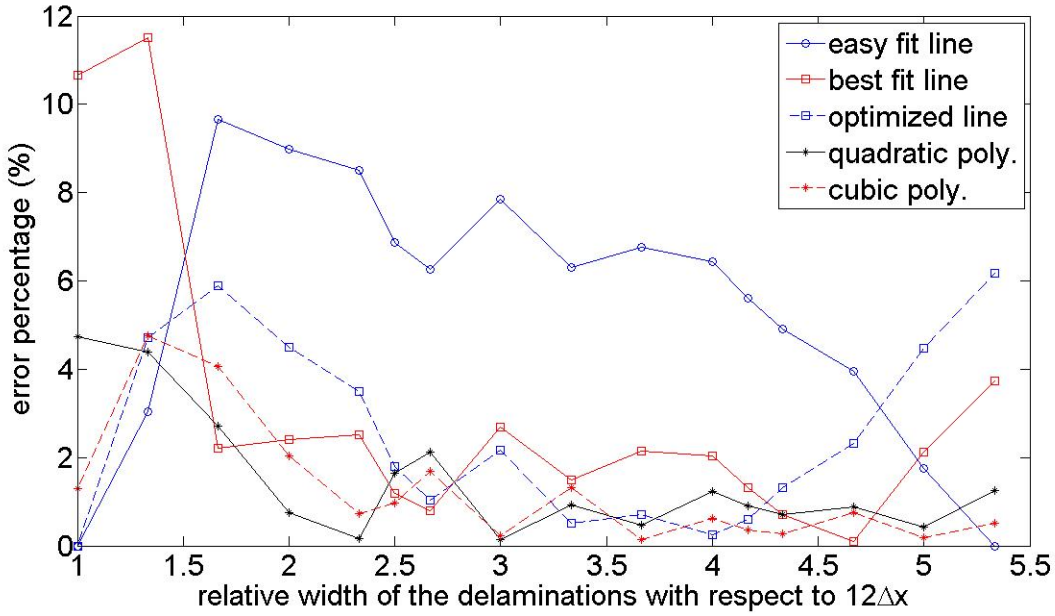

Figure 4-26: Error percentages of the fitted line and polynomials

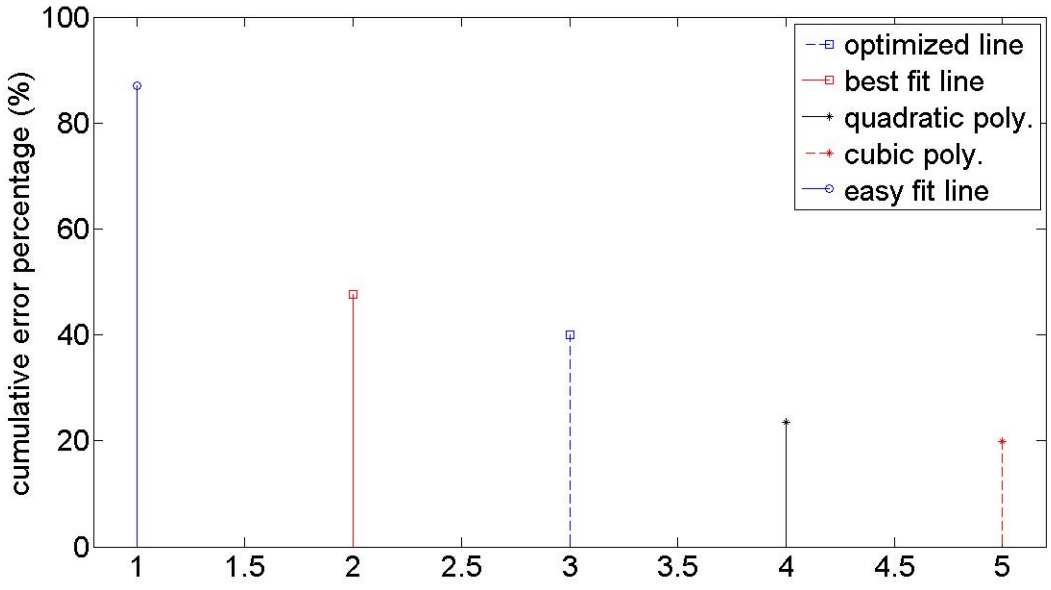

Figure 4-27: Cumulative error percentages of the fitted line and polynomials

Chapter 5

Summary, Conclusions and Future Work

5.1 Summary and Conclusions

In this thesis, geometric analysis of the finite difference time domain (FDTD) simulation for defect size estimation in ground penetrating radar (GPR) applications is performed, and the results are presented with discussions.

- Relationship between the difference in curvature values of the arch-like shapes and relative width of the delaminations are almost linear regardless of the depth of the delamination.

- To illustrate the relationship between the curvature values (k) of delaminations with different widths and the width of delaminations, linear and higher order curve fittings are performed. According to their performance, a line (optimized

line) model and a polynomial (cubic polynomial) model are chosen to represent the relationship. The equations of the linear estimation (Eq.(5.1) and the cubic (Eq.(5.2) estimation are provided in the followings.

$$W_r = 2950 \times \Delta k + 1 \qquad (5.1)$$

$$W_r = 3.719 \times 10^8 \times \Delta k^3 - 2.553 \times 10^5 \times \Delta k^2 + 2825 \times \Delta k + 1.013 \qquad (5.2)$$

where W_r is the relative width of delamination (with respect to the reference delamination) and Δk is the difference in the curvature value of the delamination in question and the curvature value of the reference delamination. The maximum error associated with the linear estimation is less than 10% and the one associated with the cubic estimation is less than 5%.

- A procedure for estimating the width of subsurface delaminations in concrete slabs is proposed for GPR applications. Steps are listed in the followings.

    1. Obtain the B-scan image of the concrete slab with a delamination inside it.
    2. Obtain the B-scan image of the concrete slab without delamination.
    3. Subtract the B-scan image of the concrete slab without delamination from the B-scan image of the concrete slab with a delamination to have a B-scan image without undesired reflections.
    4. Extract the arch-like shape from the modified B-scan image by plotting the data points with maximum amplitude.

5. Apply a low-pass filter to smoothen the arch-like shape.

6. Calculate the curvature value (k) of arch-like shapes using three data points (one at the peak and other two at 30 cm away from the peak in -x and +x directions).

7. Estimate the width of the delamination by calculating the curvature value (k) of reference delamination with a known width and using one of the following equations.

   $W_r = 2950 \times \Delta k + 1$

   $W_r = 3.719 \times 10^8 \times \Delta k^3 - 2.553 \times 10^5 \times \Delta k^2 + 2825 \times \Delta k + 1.013$

   For example, if the difference in curvatures of the reference delamination and unknown delamination is $\Delta k = 5 \times 10^{-4}$, the linear estimation provides $W_r = 2.475$ and the cubic estimation provides $W_r \cong 2.363$. Therefore, linear estimation suggests that unknown delamination is 2.475 times wider than the reference delamination and cubic estimation suggests that this ratio is 2.363. In other words, if a reference delamination is chosen as 3 cm, the estimated delamination width is $2.475 \times 3 = 7.425$ cm and $2.363 \times 3 = 7.089$ cm according to the linear estimation and cubic estimation, respectively. Note that the curvature values are computed from the time history response (B-scan images), rather than conventional spatial images.

- To apply the procedure above, the curvature value of arch-like shape must to be calculated by using the coordinates of the two points at least 30 cm away from the peak in -x and +x directions and using the coordinates of the peak point of

the arch-like shape. In other words, concrete slab must be scanned from at least 30 cm before and until 30 cm away from the center of the delamination. This is because the curvature values show a settled behaviour at scanning distances higher than 30 cm.

5.2 Future Work

In this thesis, only horizontally aligned rectangular delaminations inside concrete slabs are considered. Further studies examining the B-scan images of delaminations with different orientations are needed. Moreover, different dielectric constants of concrete can be considered. The relationship between curvature values and the width of delamination can be investigated in order to develope a more general procedure. Beside these, circle scatterers representing steel reinforcement (rebars) can be defined inside the concrete slab to develop another set of estimation equations for predicting the size of steel rebars.

Appendix A

Clean B-scan Images of Slabs

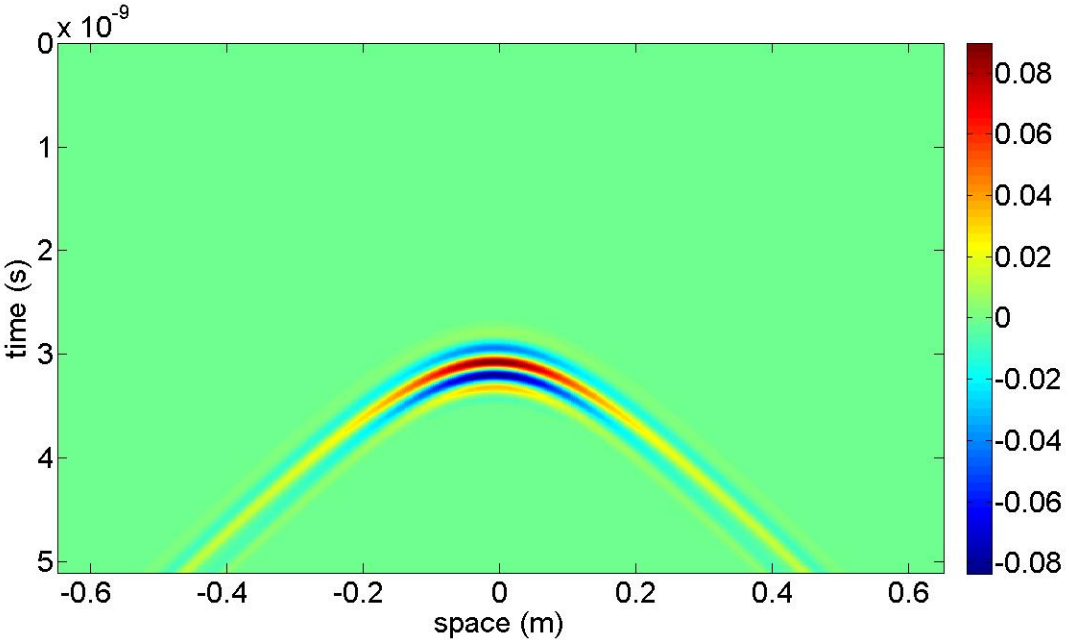

Figure A-1: Clean B-scan image of slab D149W16

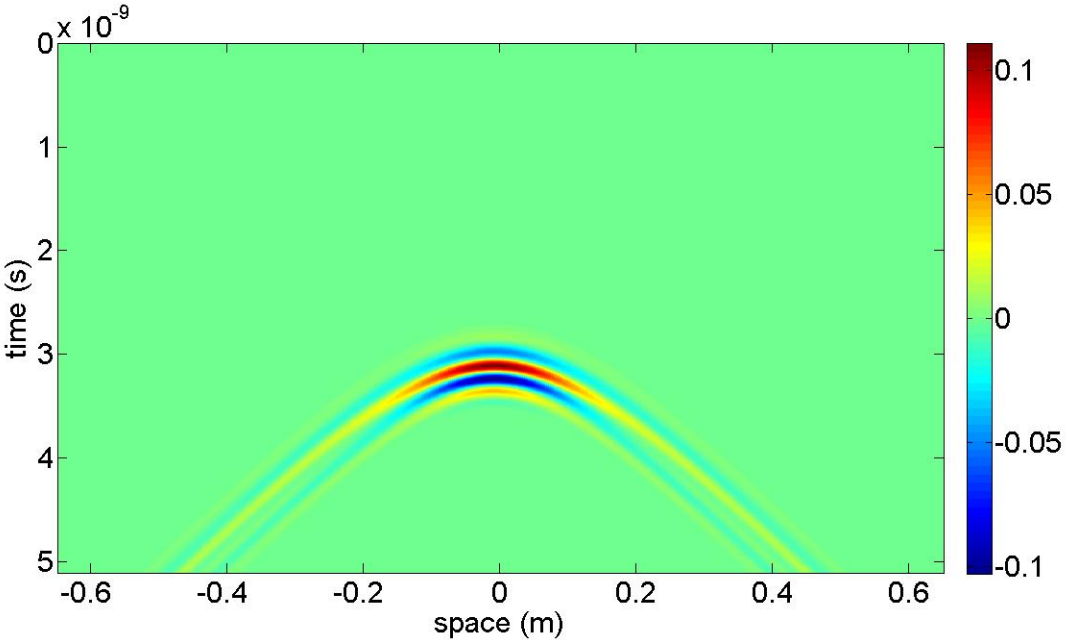

Figure A-2: Clean B-scan image of slab D149W20

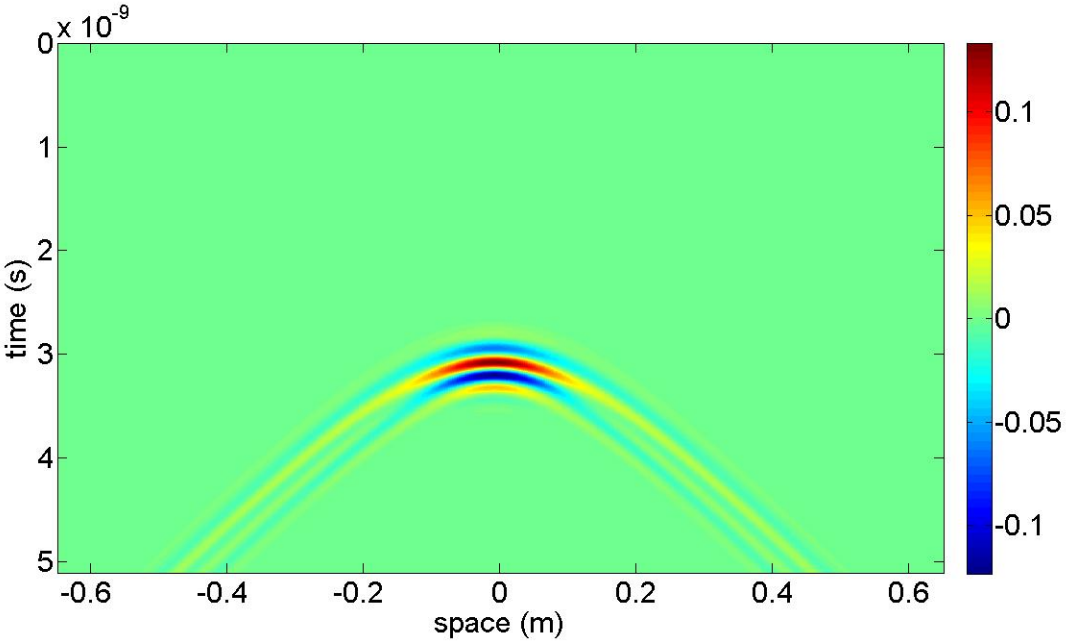

Figure A-3: Clean B-scan image of slab D149W24

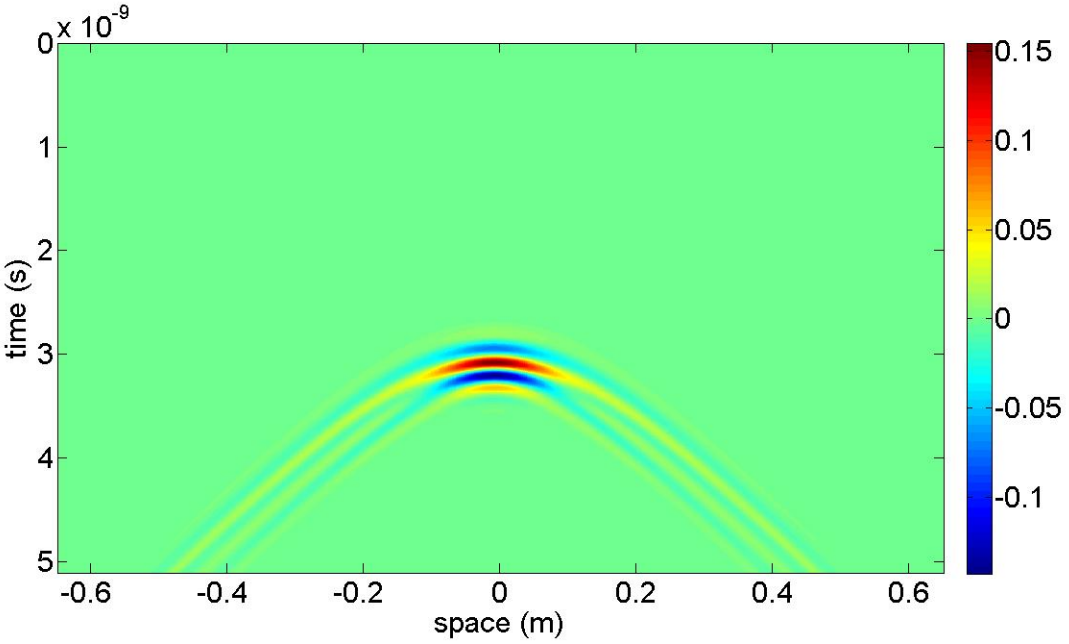

Figure A-4: Clean B-scan image of slab D149W28

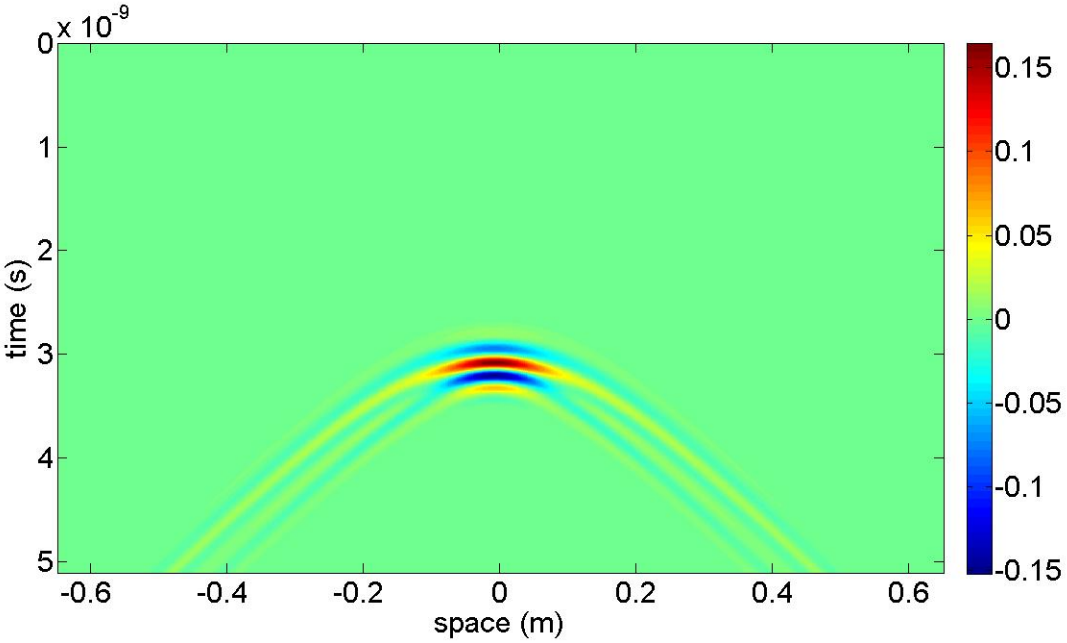

Figure A-5: Clean B-scan image of slab D149W30

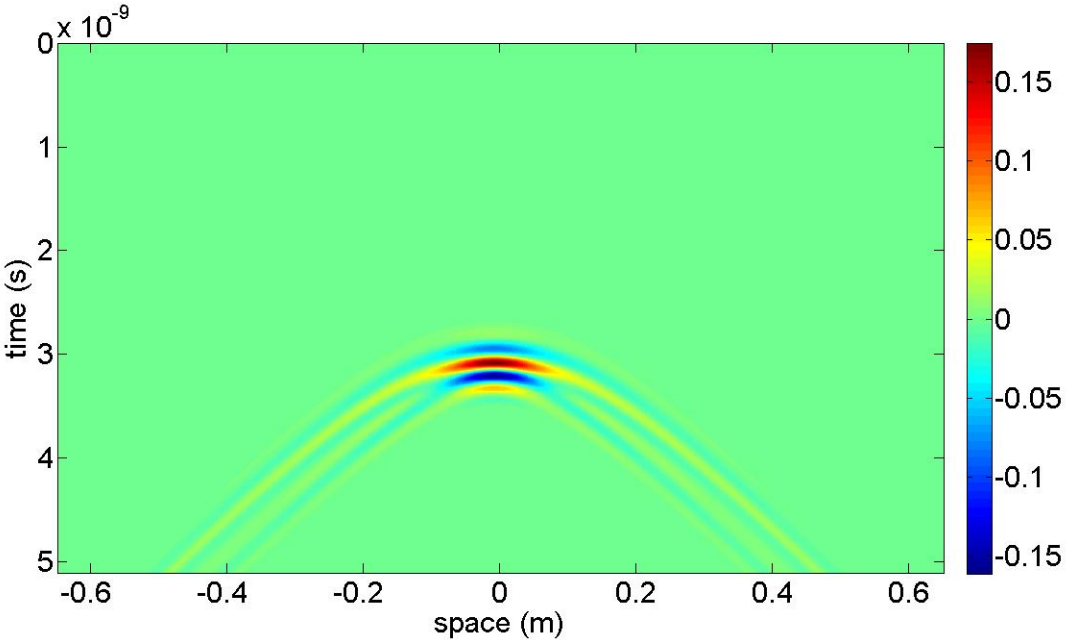

Figure A-6: Clean B-scan image of slab D149W32

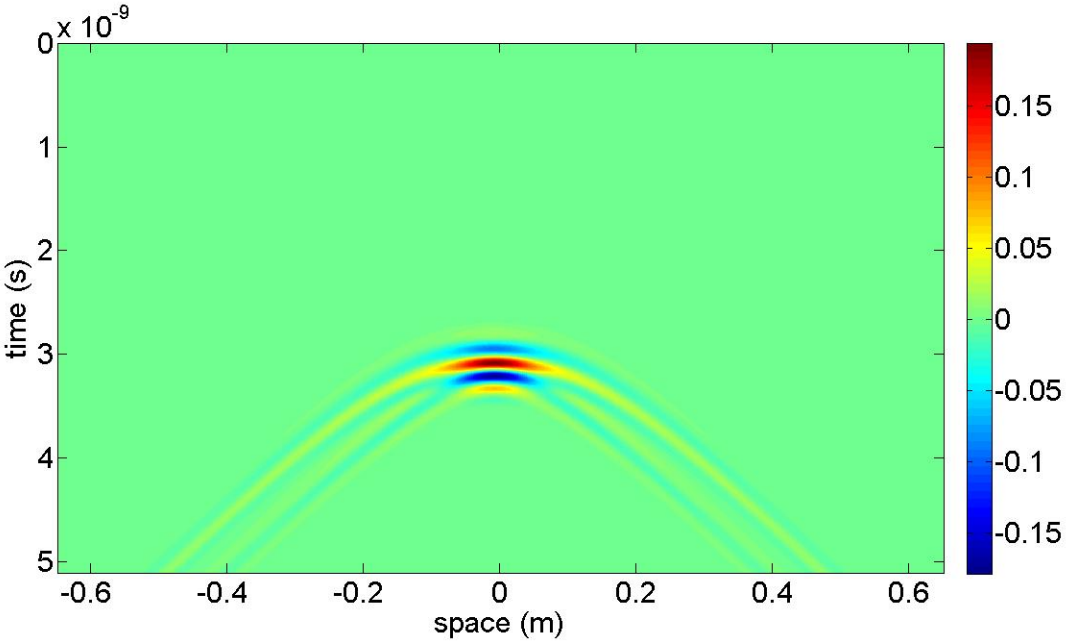

Figure A-7: Clean B-scan image of slab D149W36

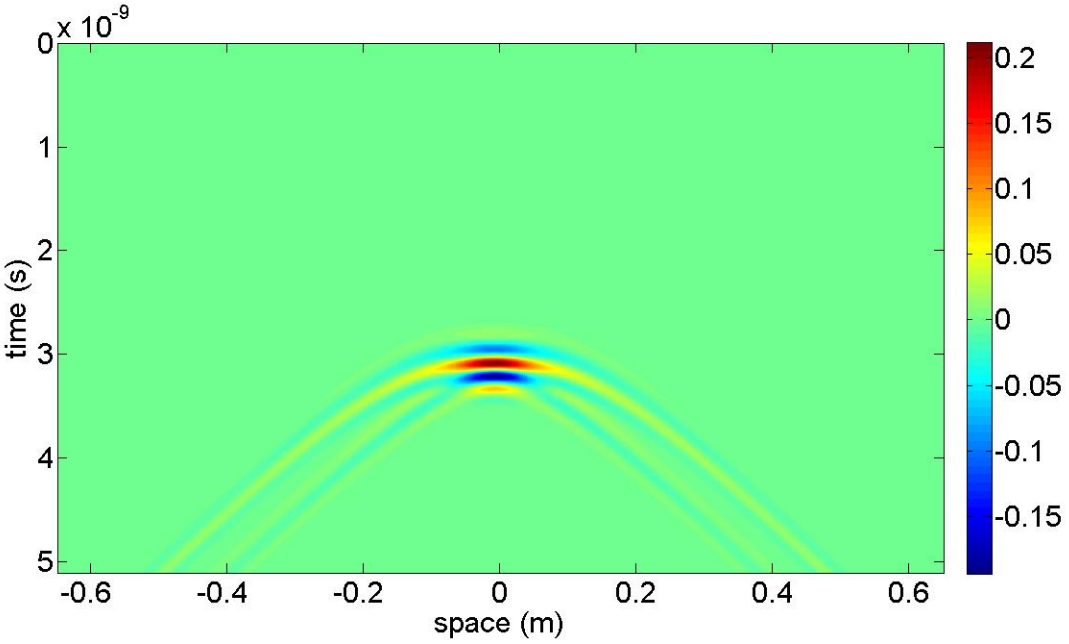

Figure A-8: Clean B-scan image of slab D149W40

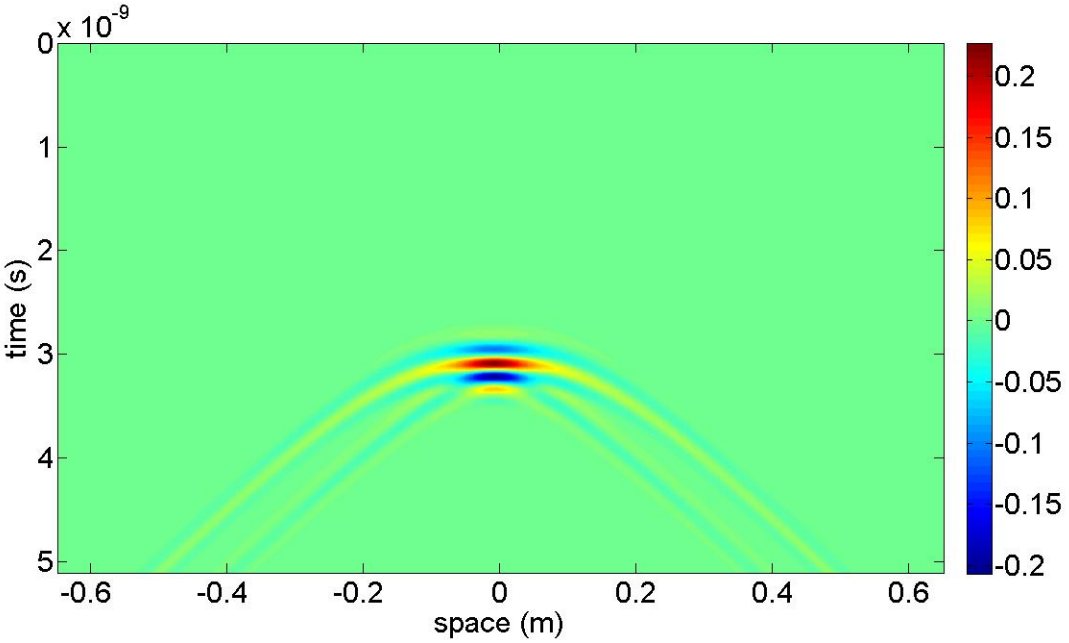

Figure A-9: Clean B-scan image of slab D149W44

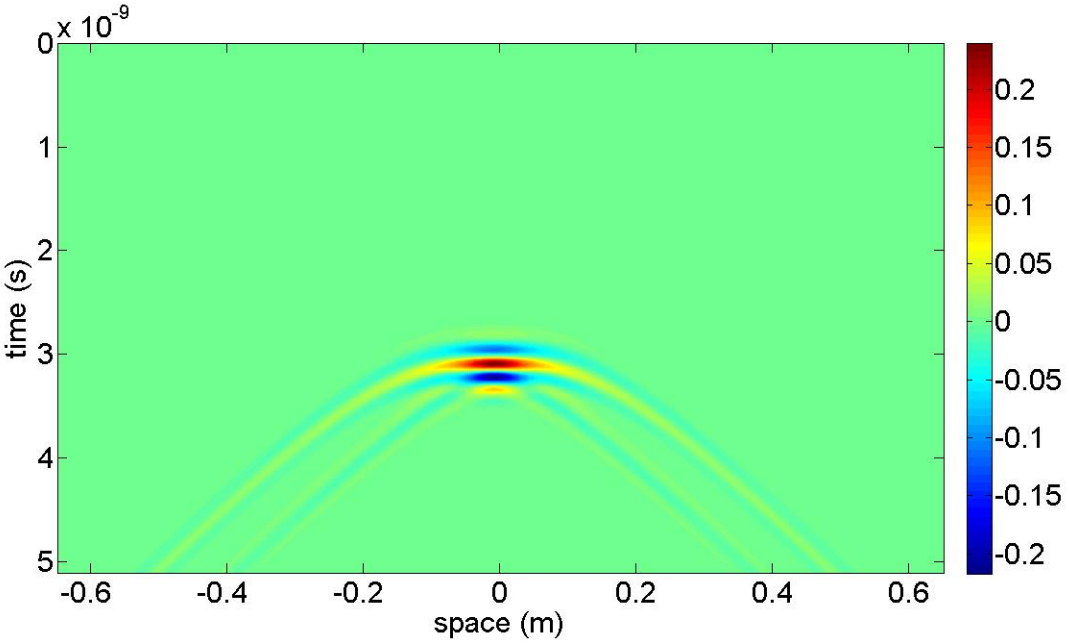

Figure A-10: Clean B-scan image of slab D149W48

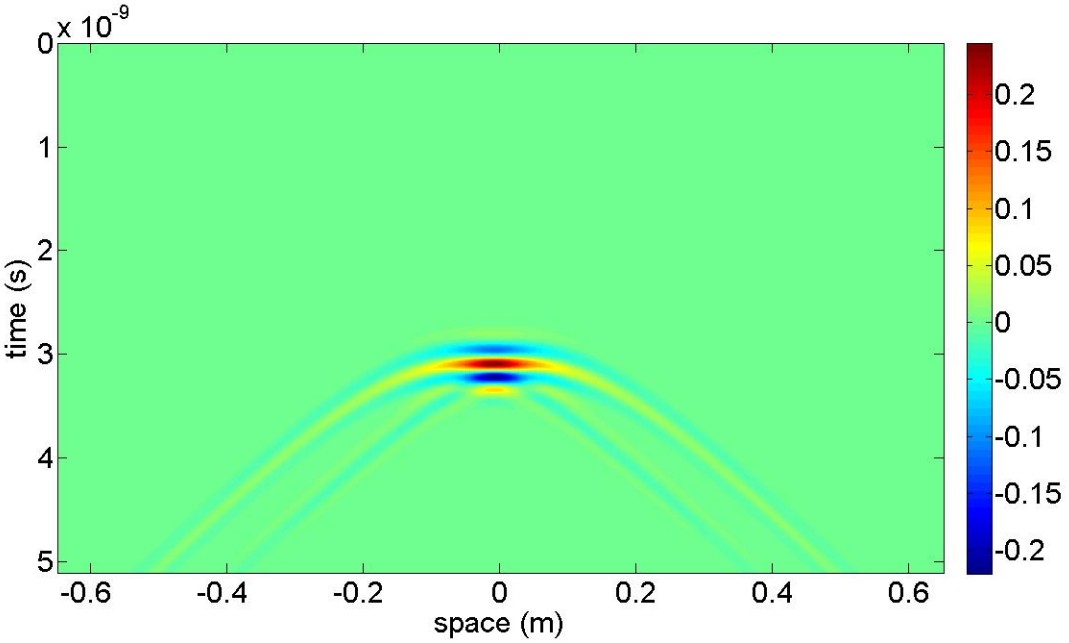

Figure A-11: Clean B-scan image of slab D149W50

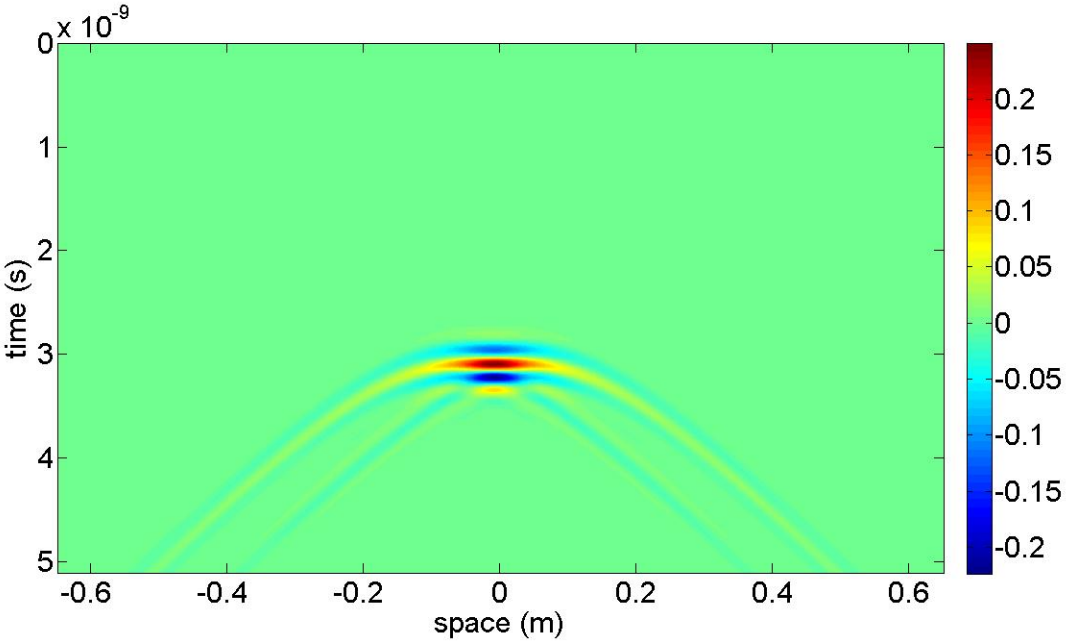

Figure A-12: Clean B-scan image of slab D149W52

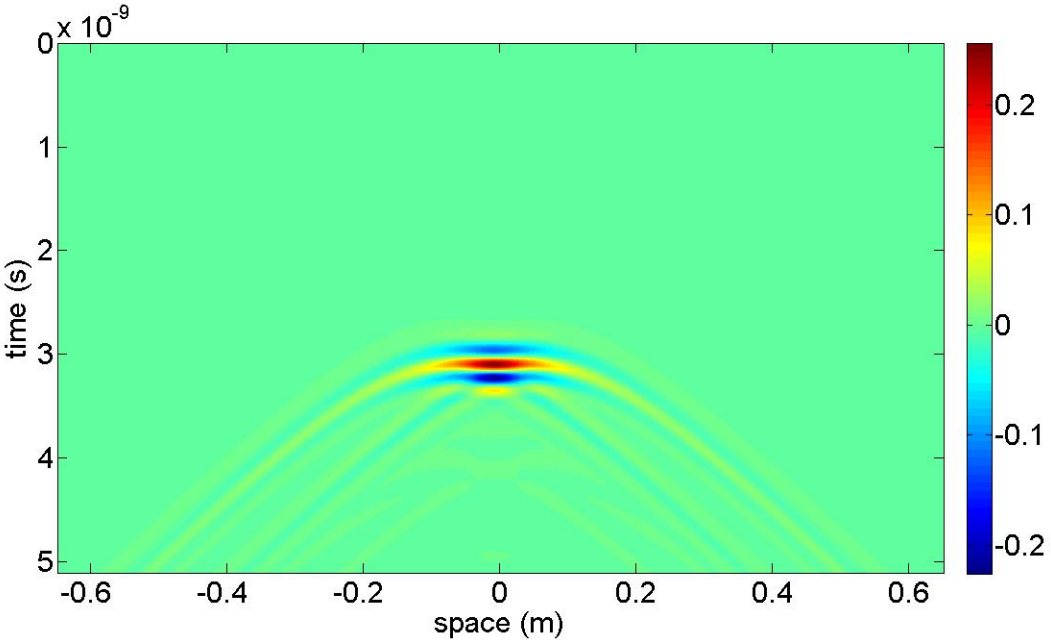

Figure A-13: Clean B-scan image of slab D149W56

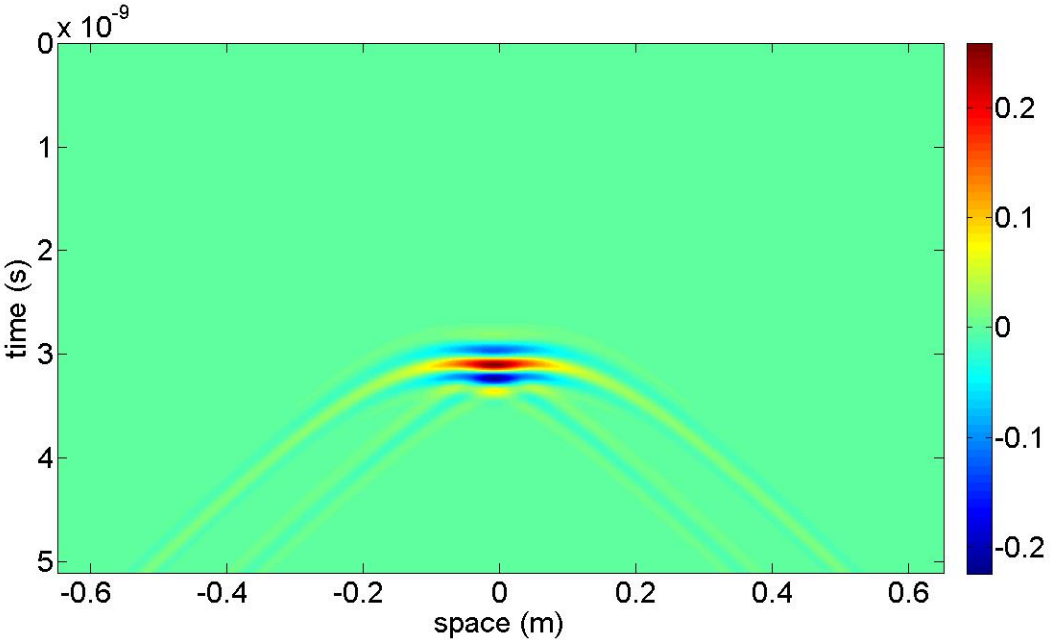

Figure A-14: Clean B-scan image of slab D149W60

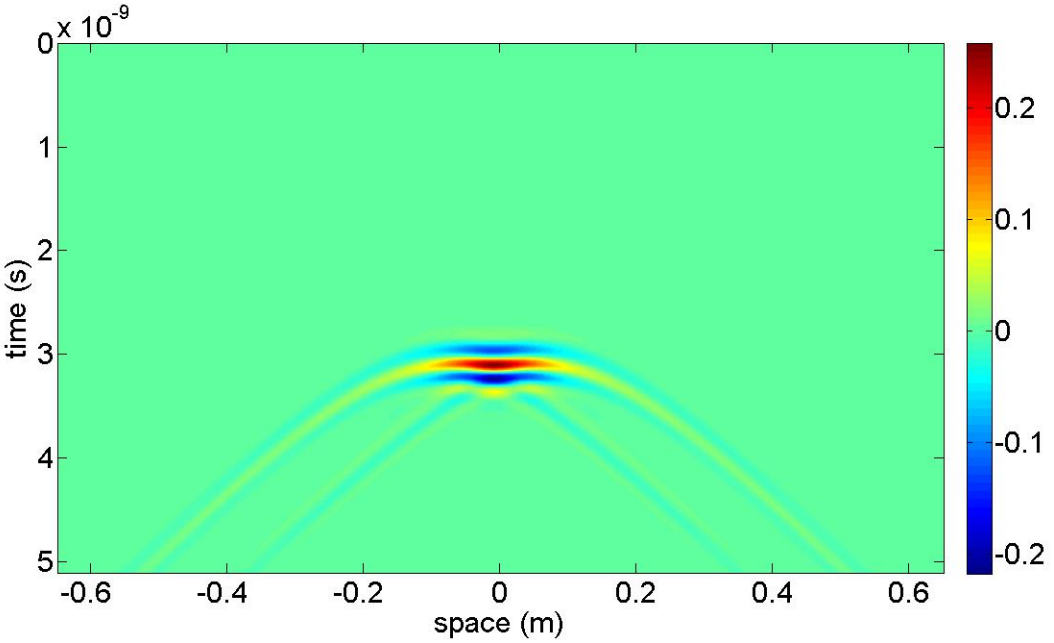

Figure A-15: Clean B-scan image of slab D149W64

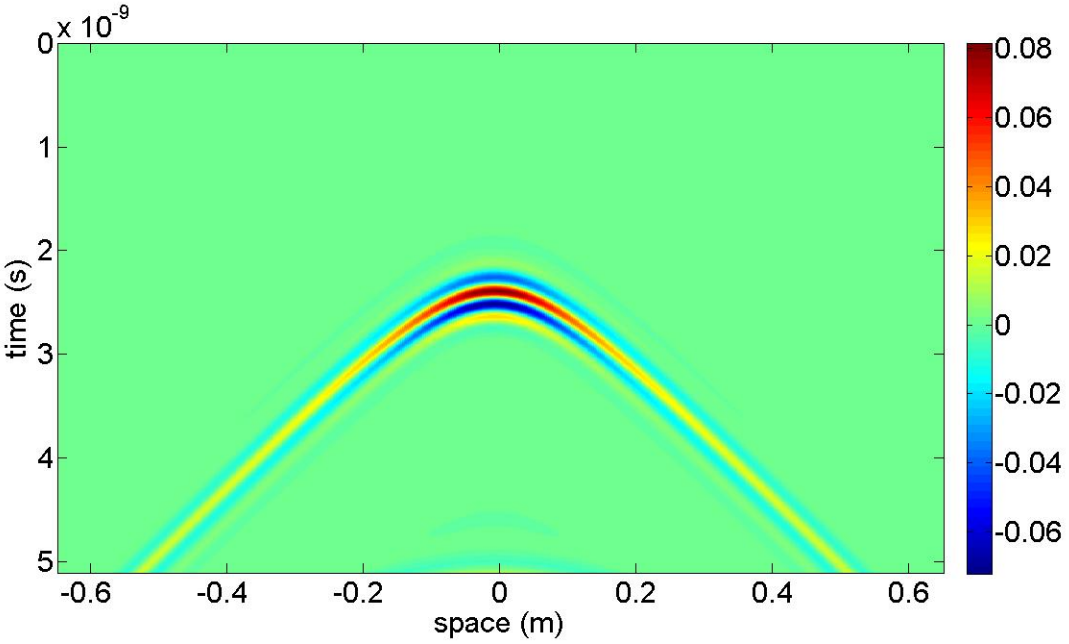

Figure A-16: Clean B-scan image of slab D129W12

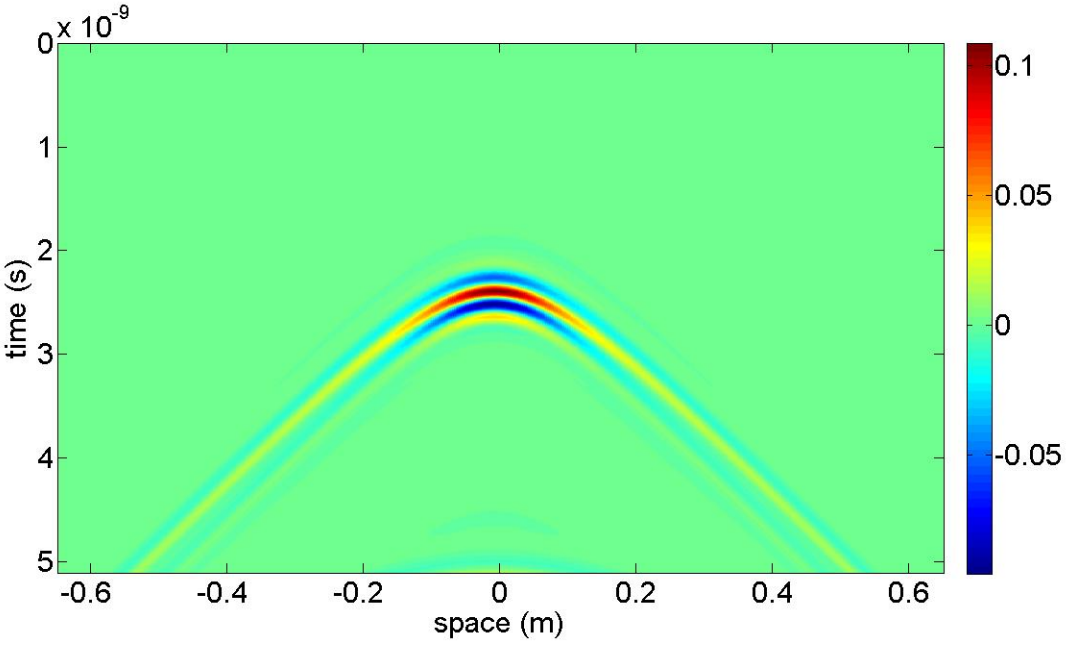

Figure A-17: Clean B-scan image of slab D129W16

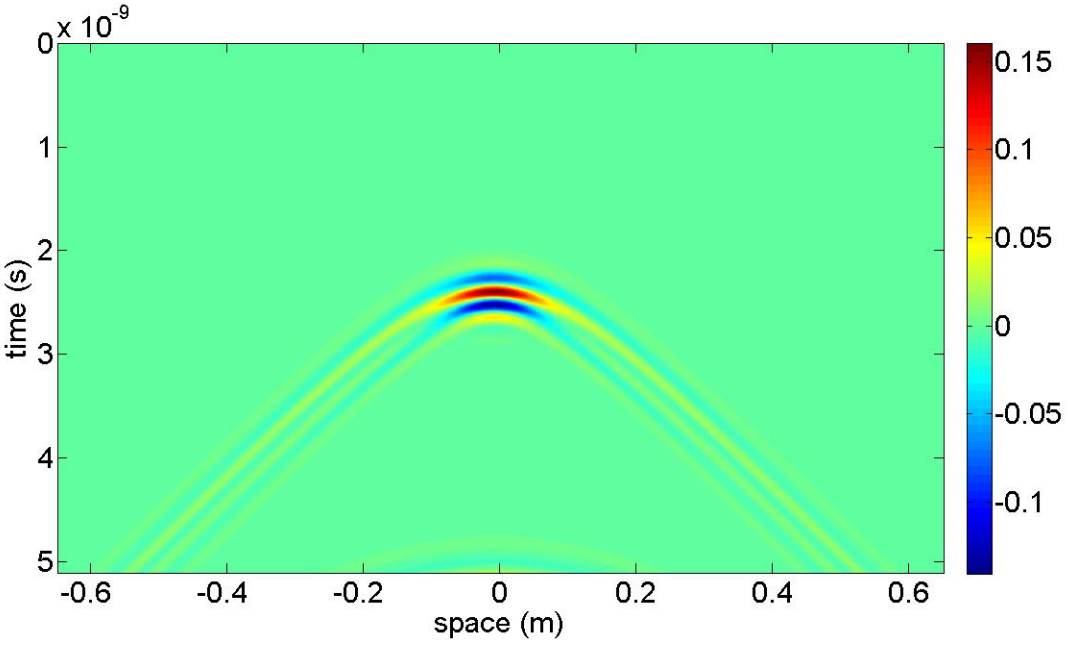

Figure A-18: Clean B-scan image of slab D129W24

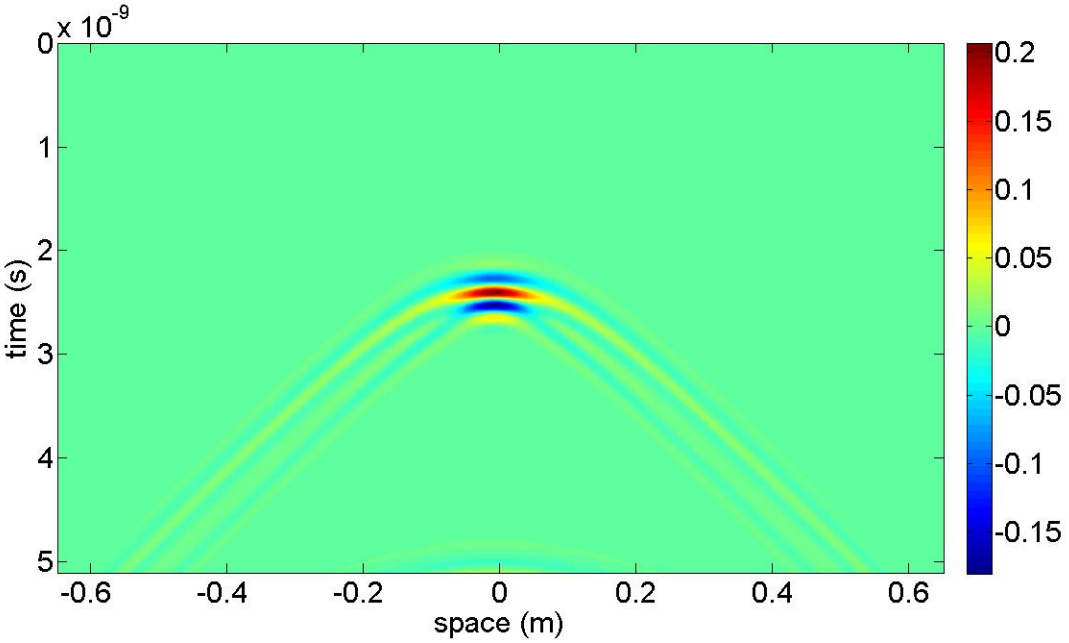

Figure A-19: Clean B-scan image of slab D129W32

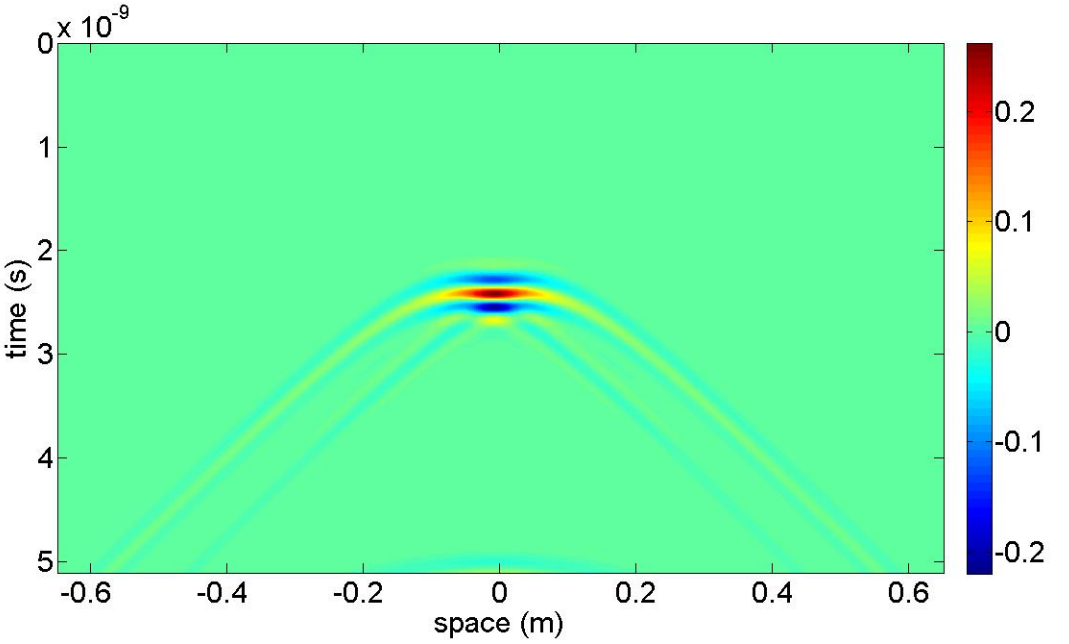

Figure A-20: Clean B-scan image of slab D129W48

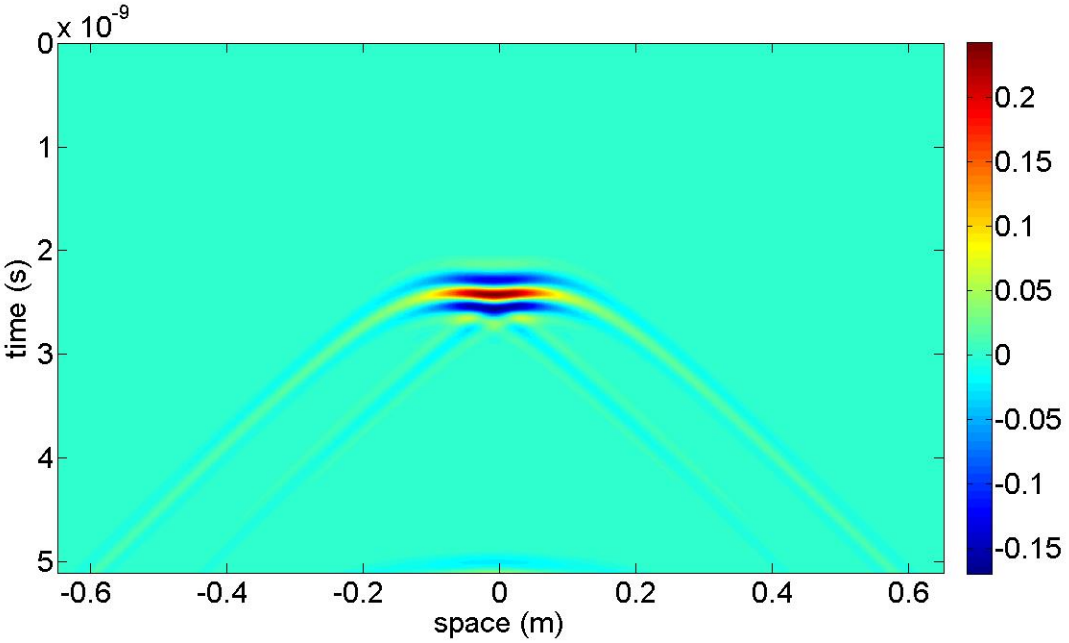

Figure A-21: Clean B-scan image of slab D129W64

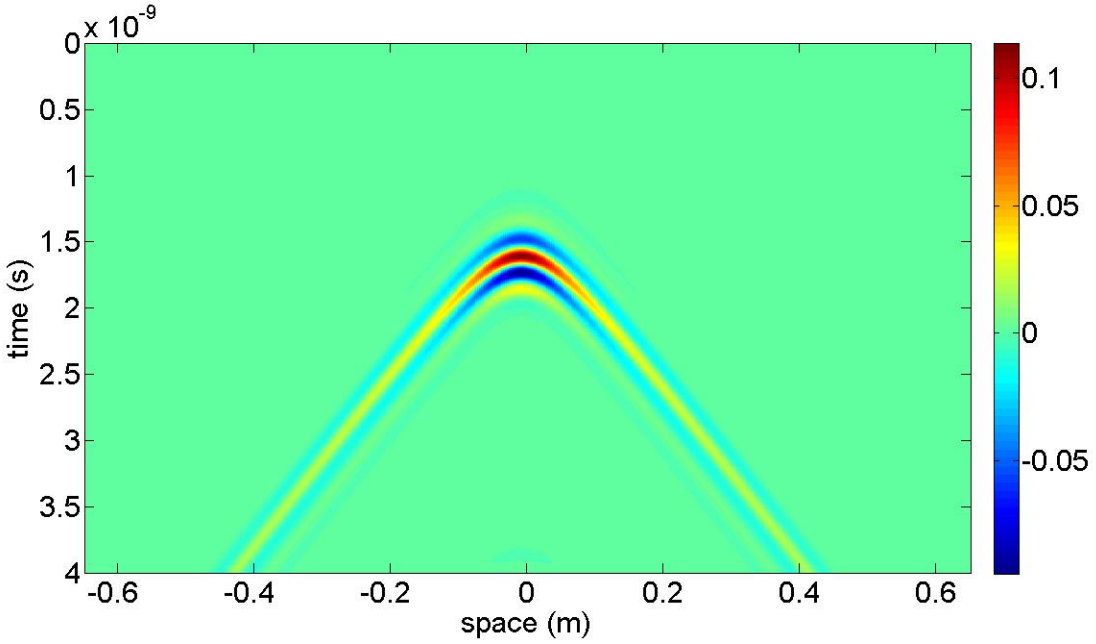

Figure A-22: Clean B-scan image of slab D109W12

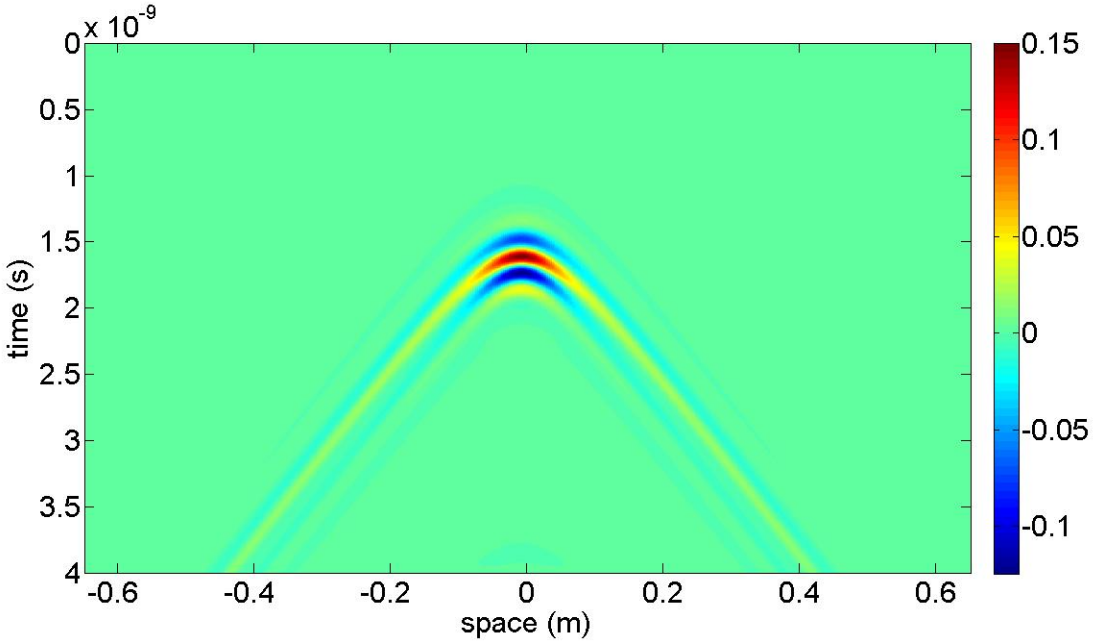

Figure A-23: Clean B-scan image of slab D109W16

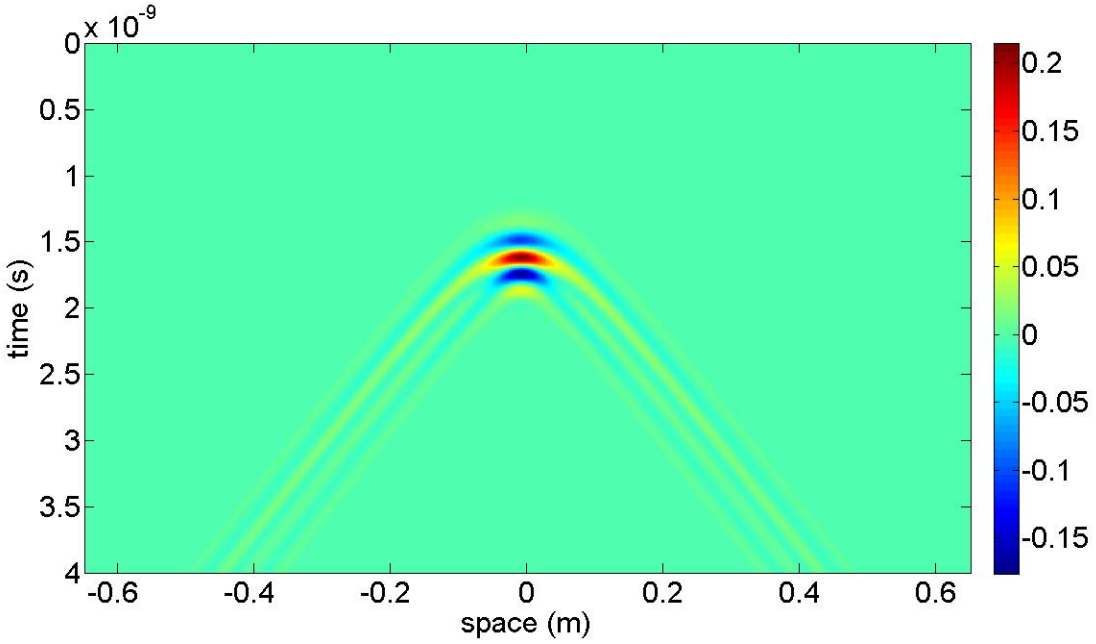

Figure A-24: Clean B-scan image of slab D109W24

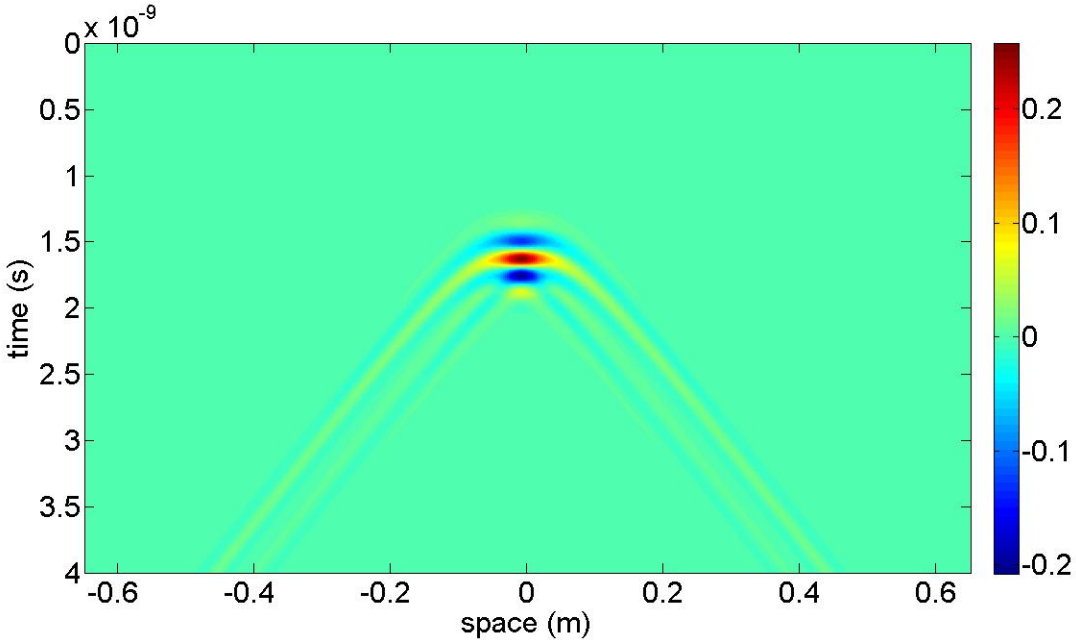

Figure A-25: Clean B-scan image of slab D109W32

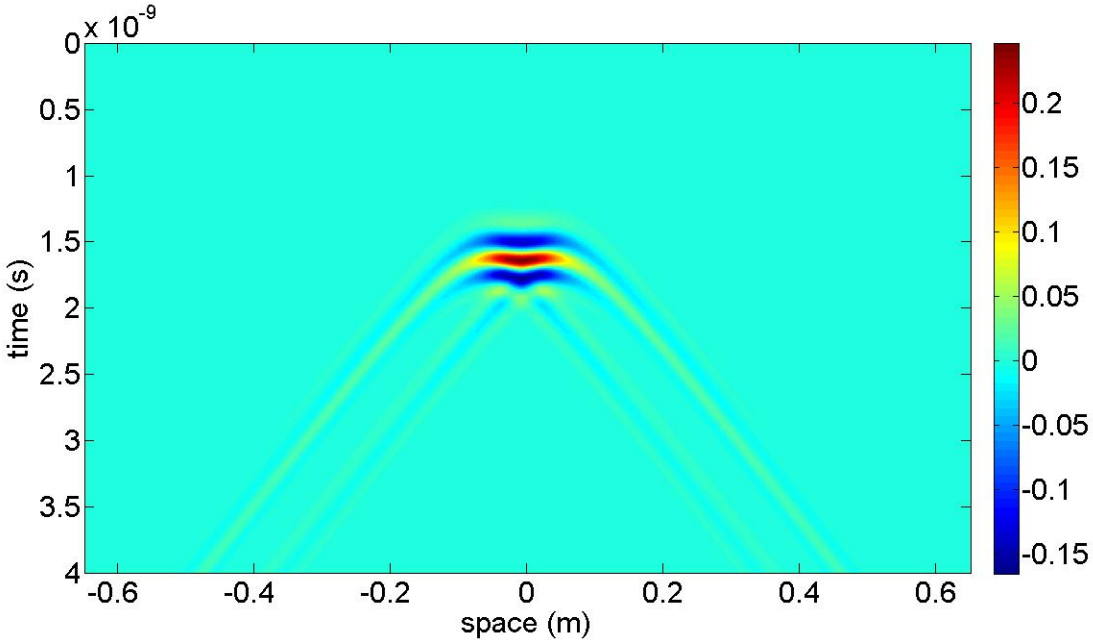

Figure A-26: Clean B-scan image of slab D109W48

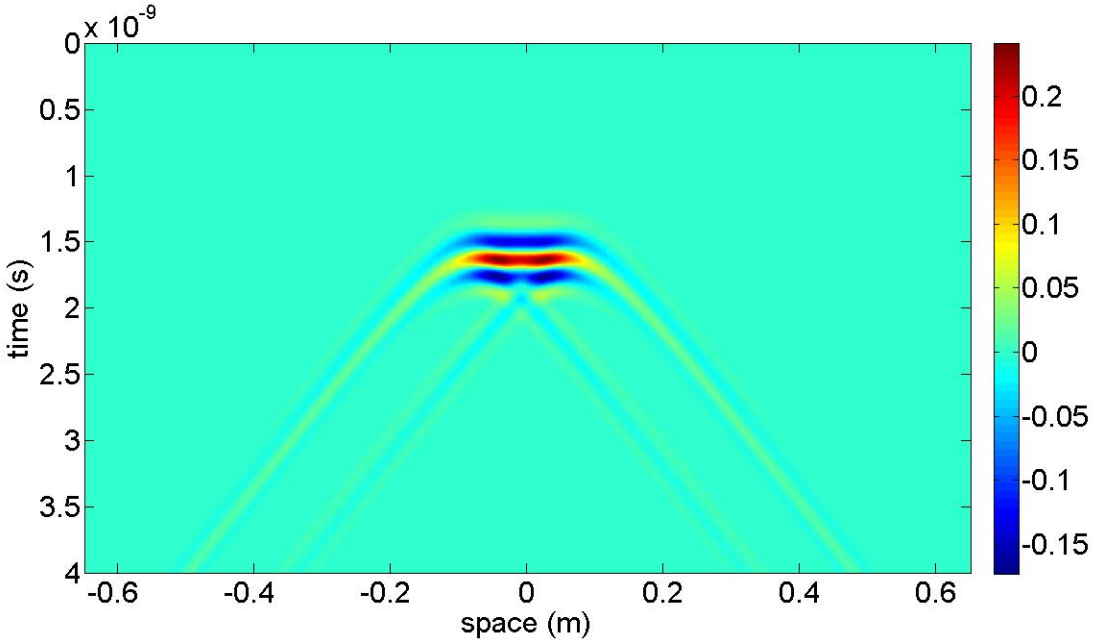

Figure A-27: Clean B-scan image of slab D109W64

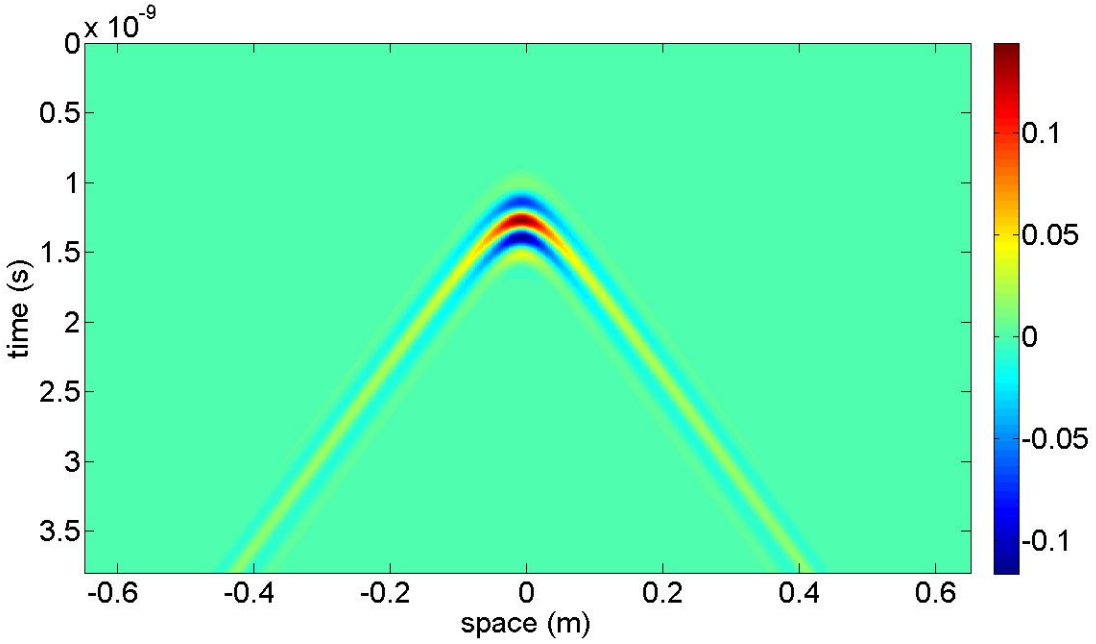

Figure A-28: Clean B-scan image of slab D99W12

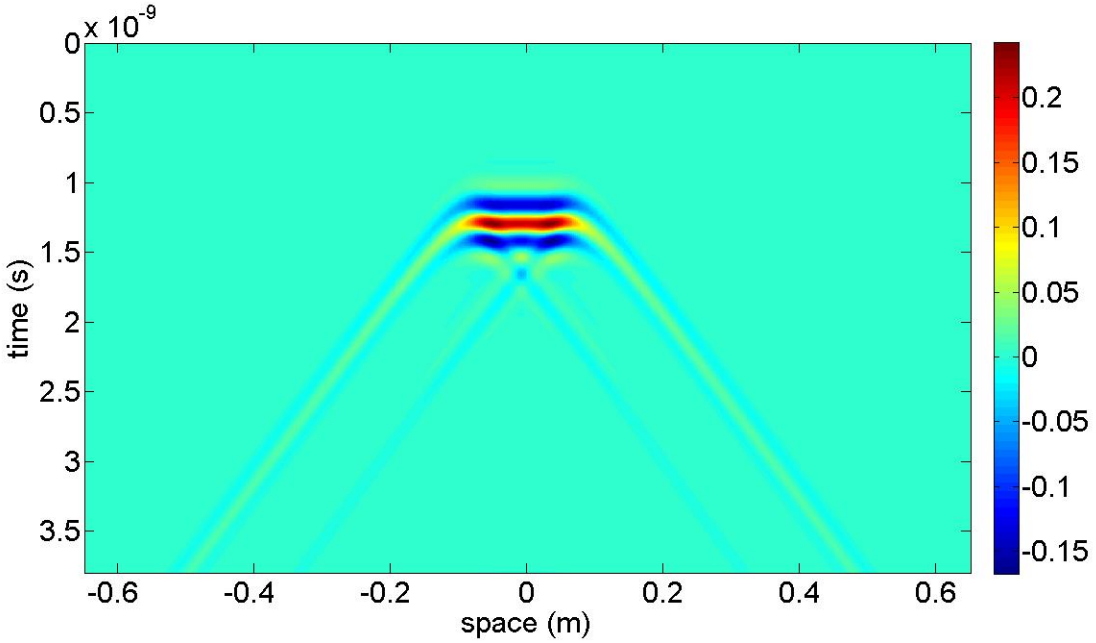

Figure A-29: Clean B-scan image of slab D99W64

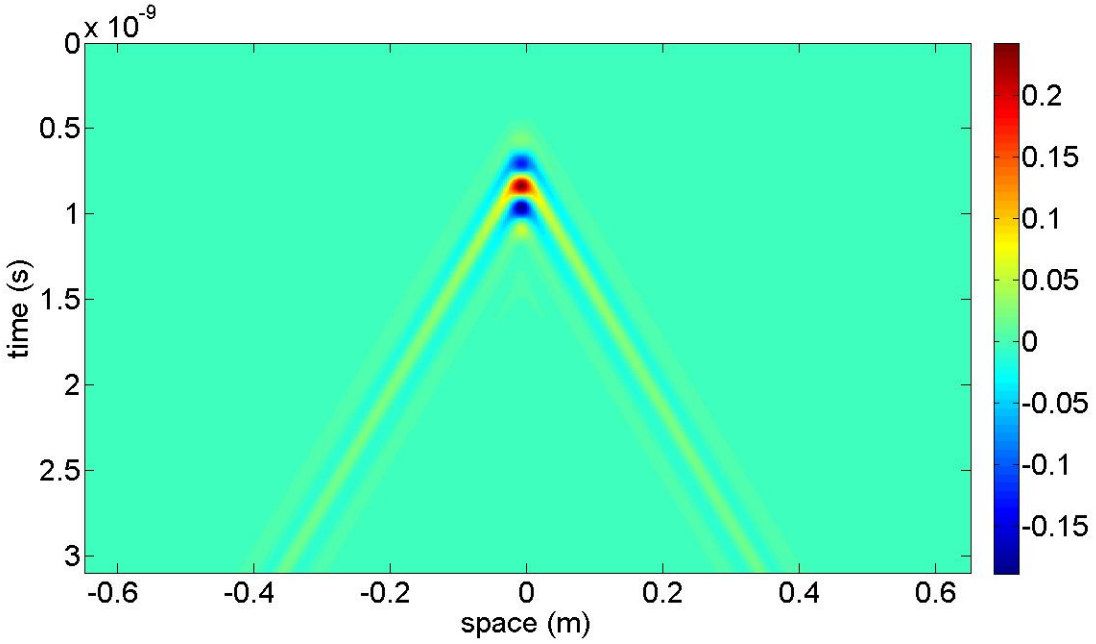

Figure A-30: Clean B-scan image of slab D89W12

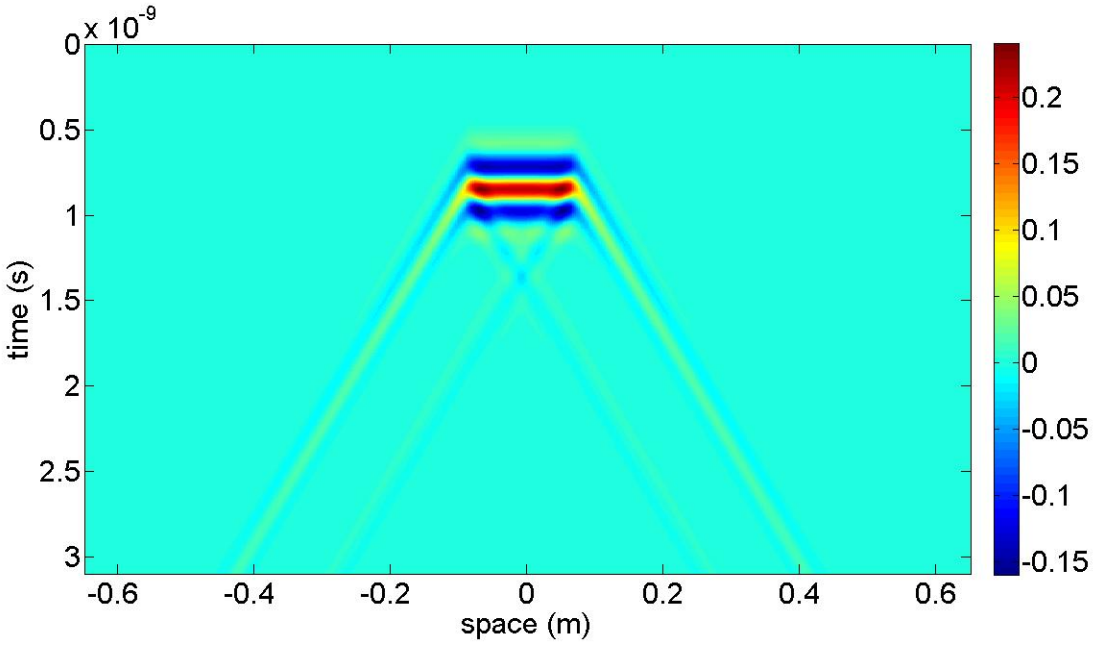

Figure A-31: Clean B-scan image of slab D89W64

Appendix B

Arch-Like Shapes

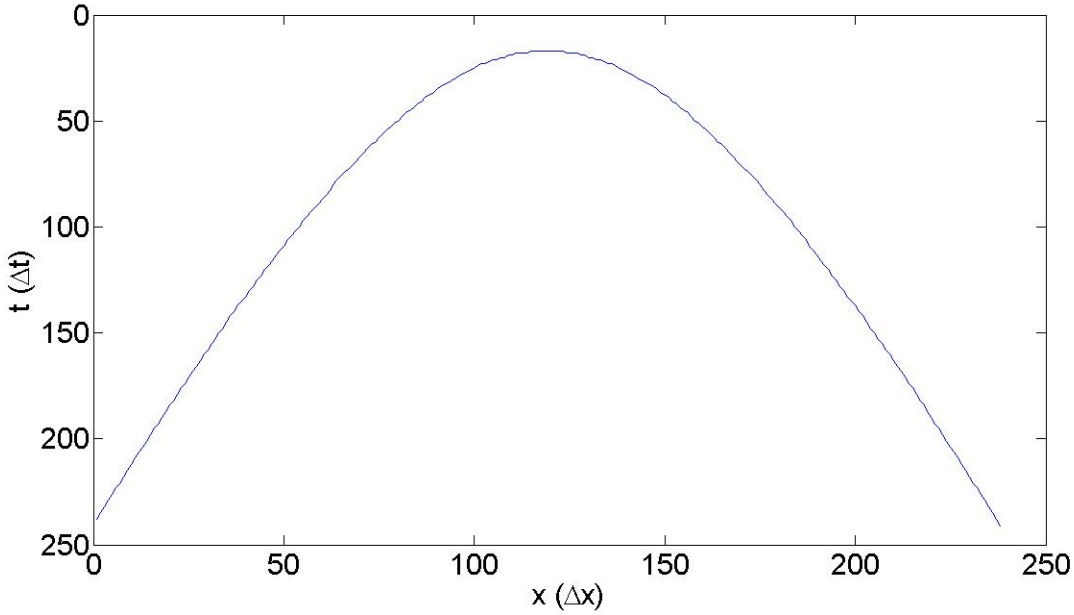

Figure B-1: Arch-like shape extracted from the B-scan image of slab D149W16

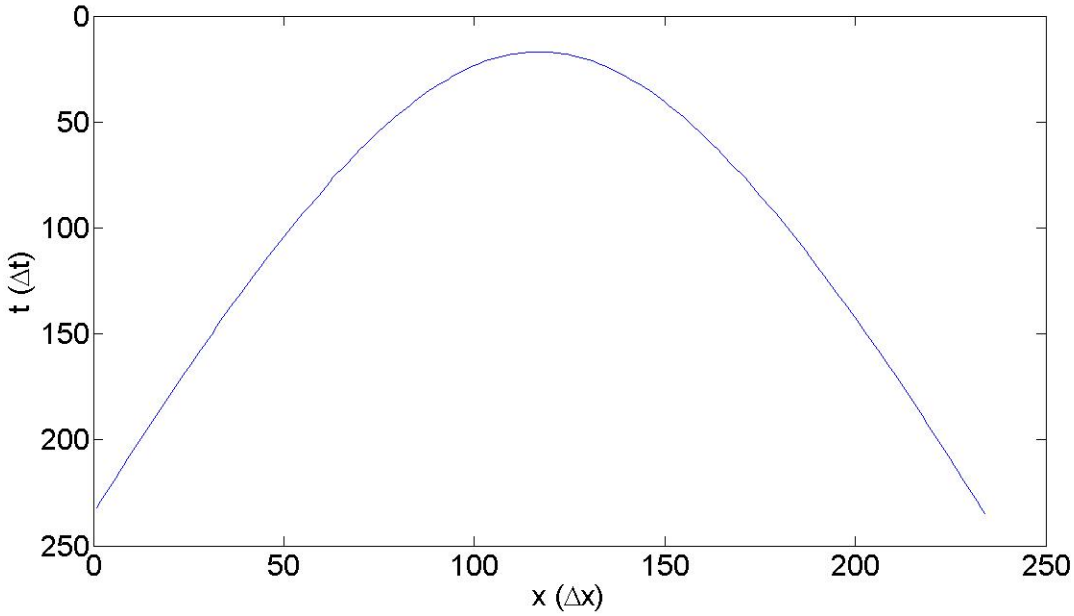

Figure B-2: Smoothened arch-like shape extracted from the B-scan image of slab D149W16

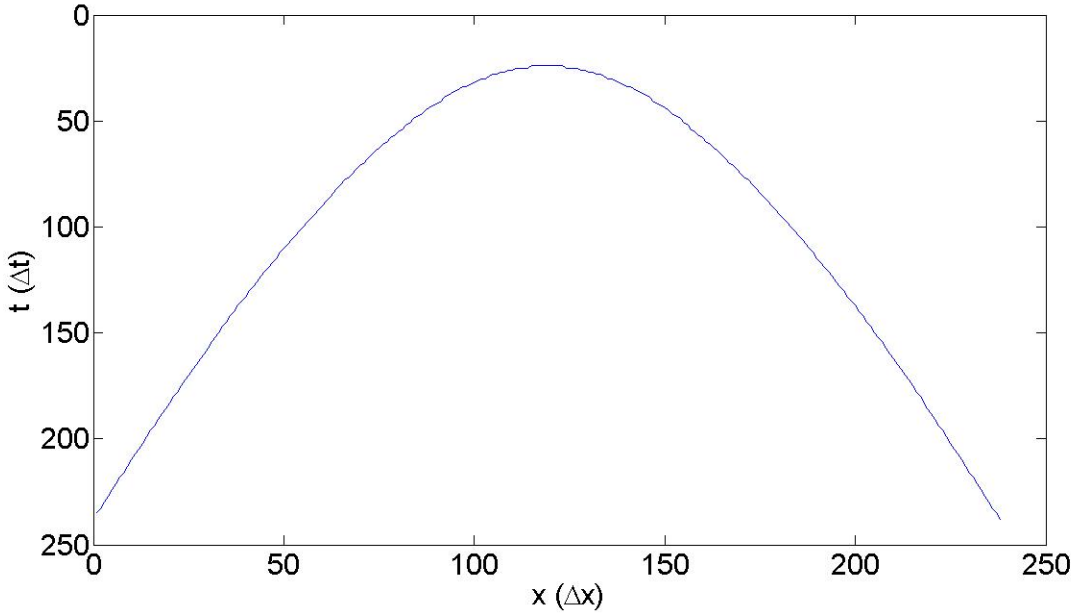

Figure B-3: Arch-like shape extracted from the B-scan image of slab D149W20

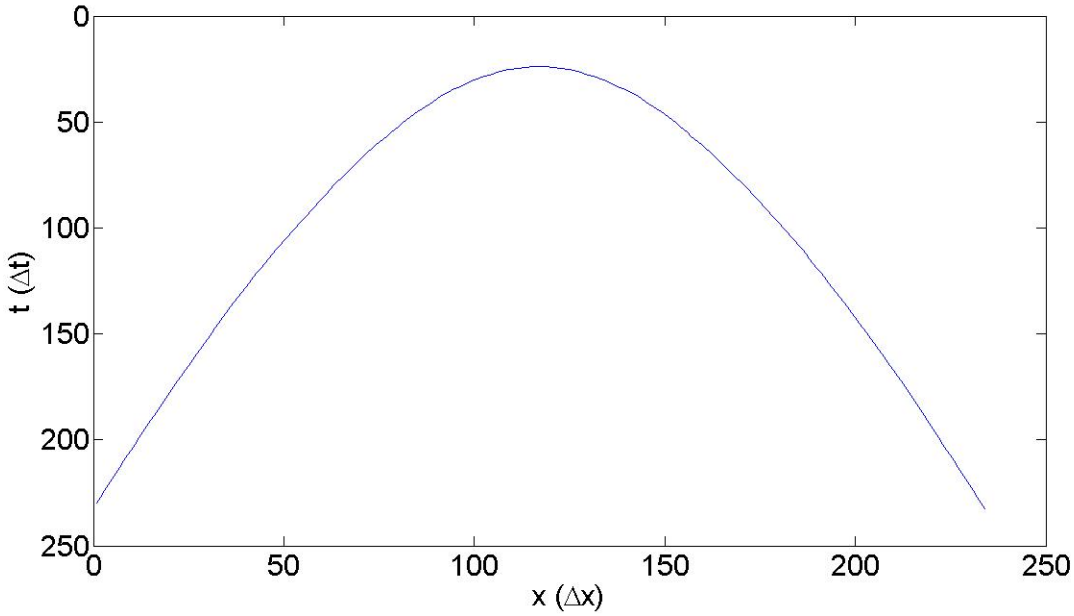

Figure B-4: Smoothened arch-like shape extracted from the B-scan image of slab D149W20

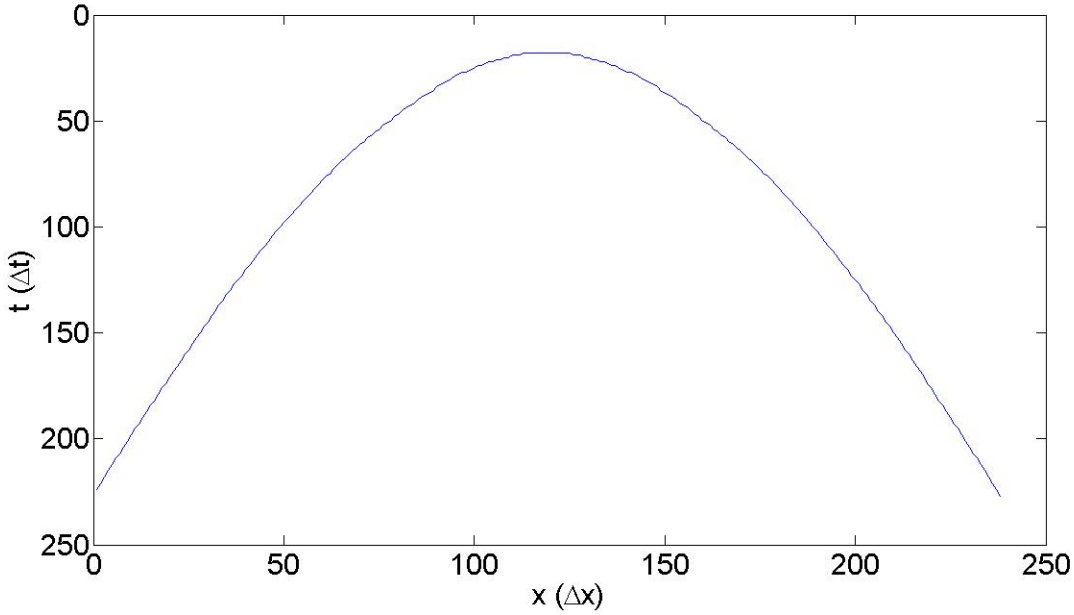

Figure B-5: Arch-like shape extracted from the B-scan image of slab D149W24

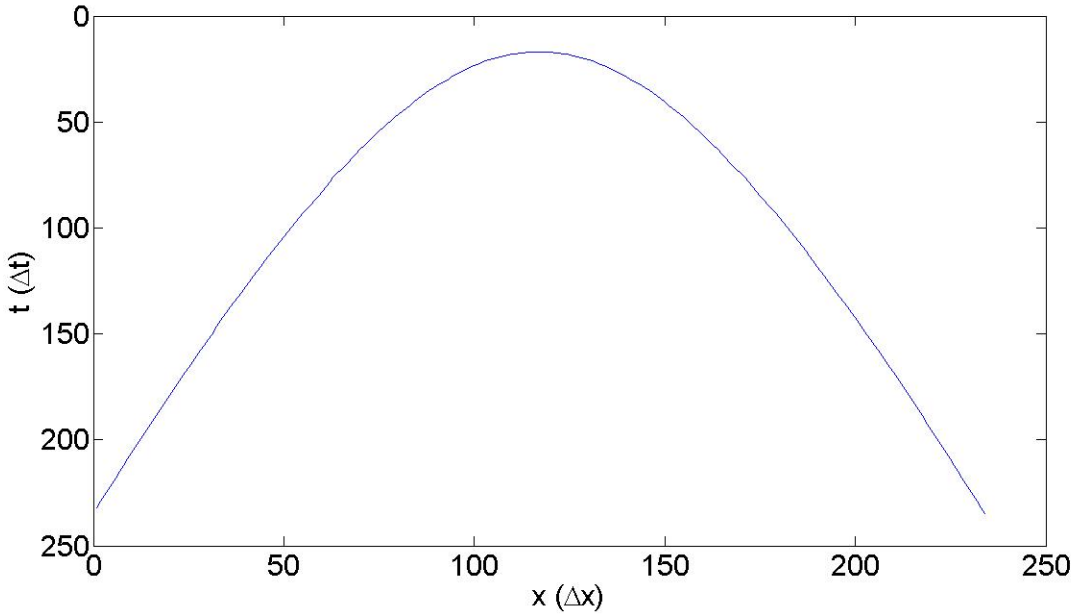

Figure B-6: Smoothened arch-like shape extracted from the B-scan image of slab D149W24

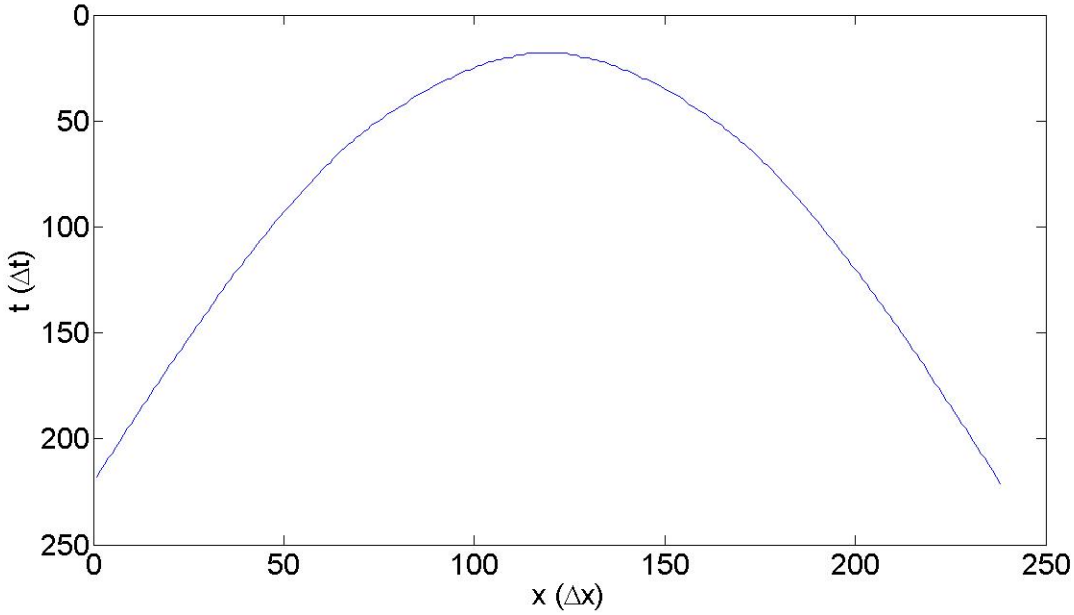

Figure B-7: Arch-like shape extracted from the B-scan image of slab D149W28

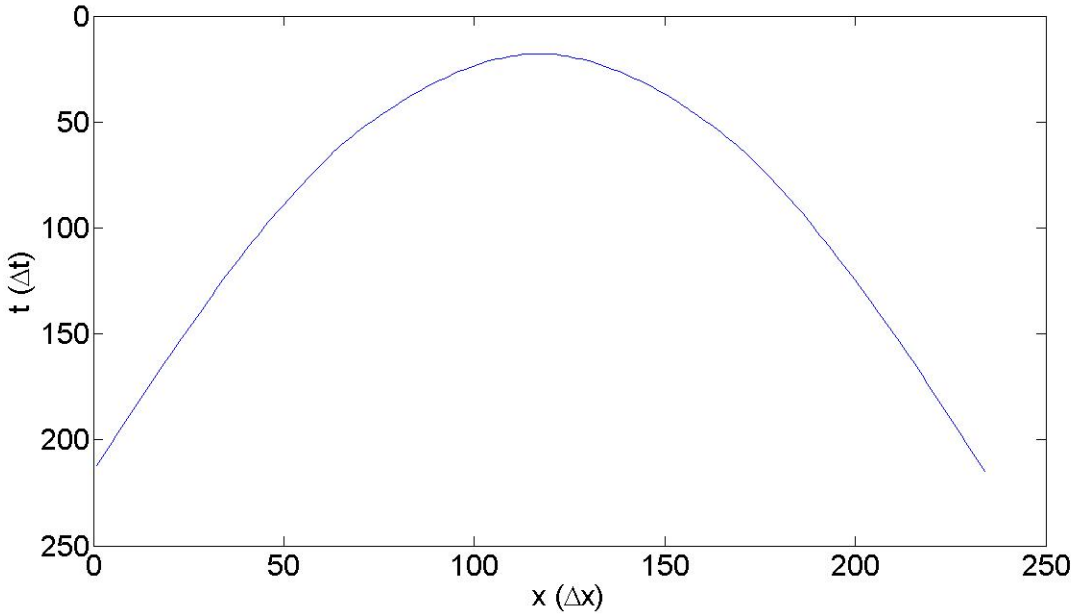

Figure B-8: Smoothened arch-like shape extracted from the B-scan image of slab D149W28

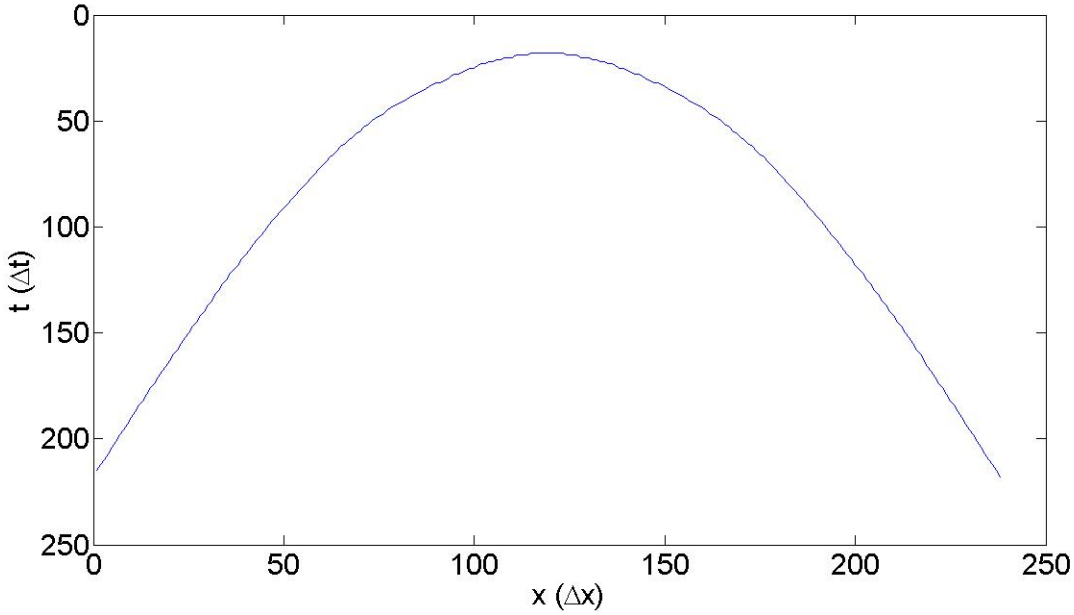

Figure B-9: Arch-like shape extracted from the B-scan image of slab D149W30

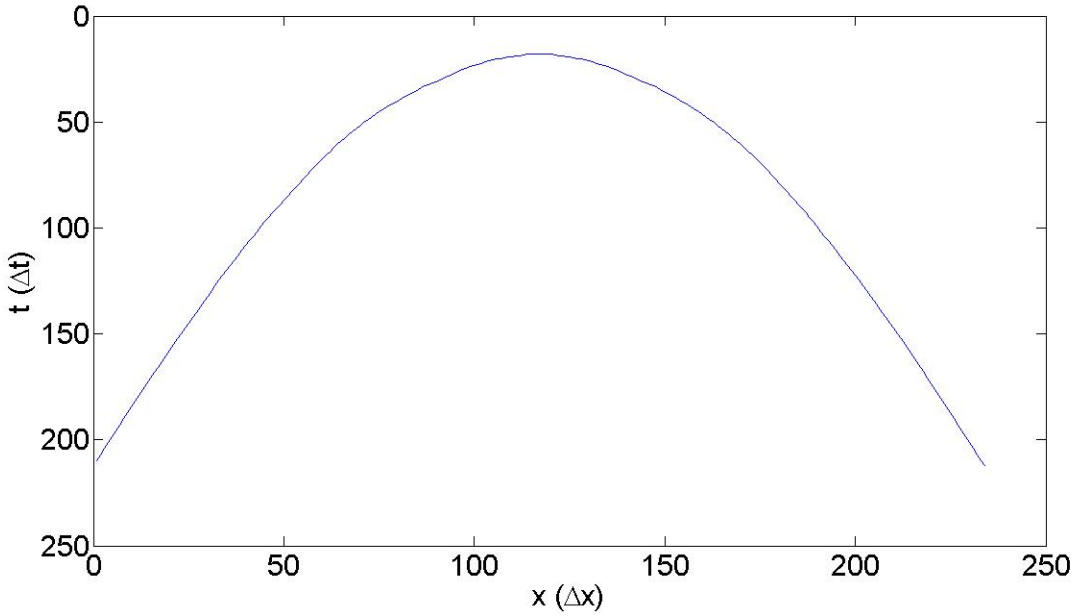

Figure B-10: Smoothened arch-like shape extracted from the B-scan image of slab D149W30

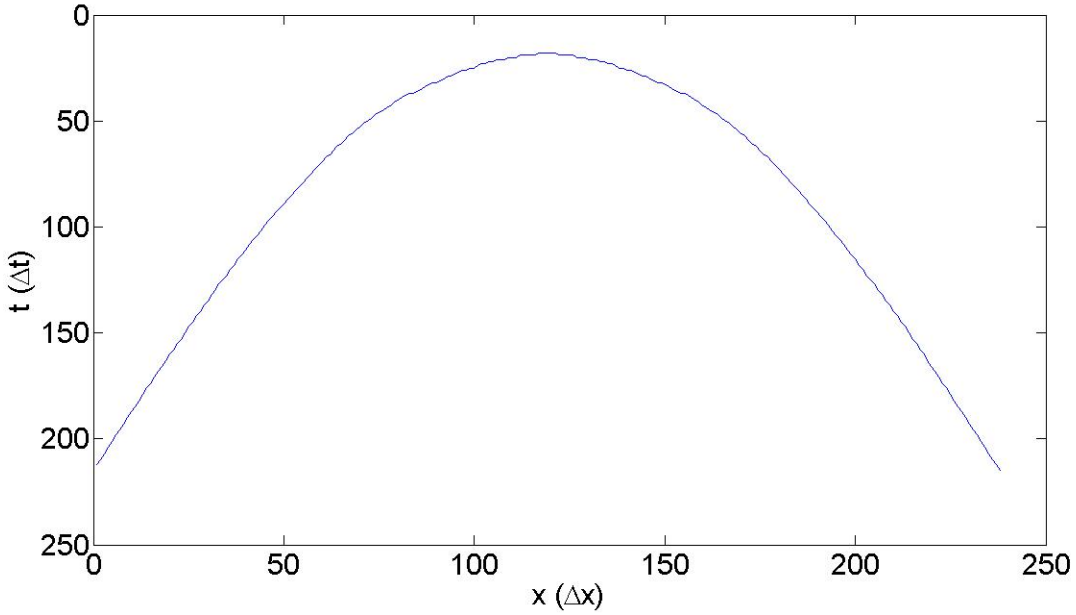

Figure B-11: Arch-like shape extracted from the B-scan image of slab D149W32

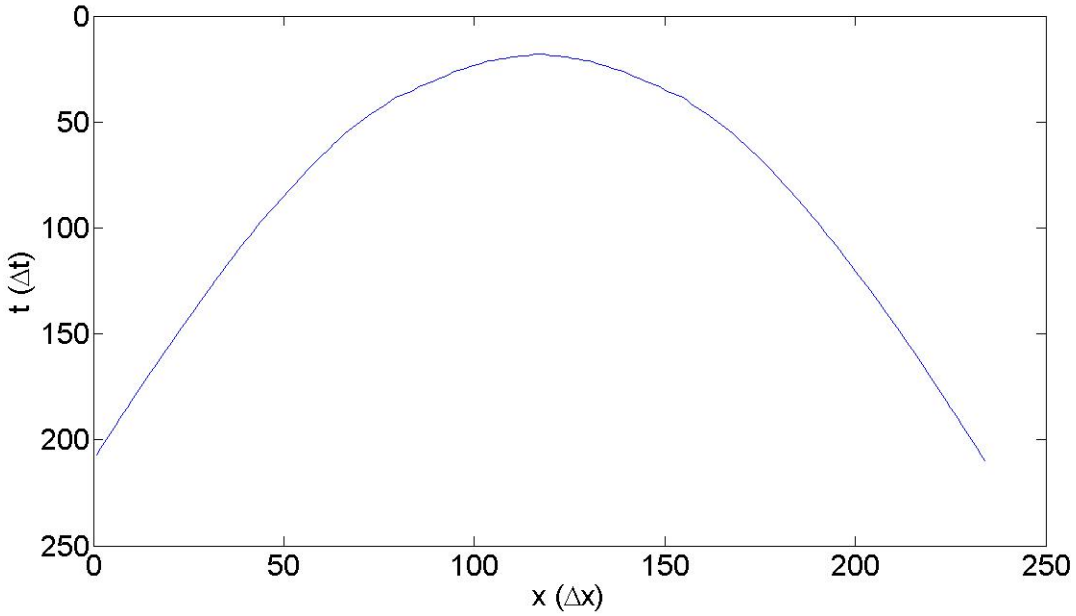

Figure B-12: Smoothened arch-like shape extracted from the B-scan image of slab D149W32

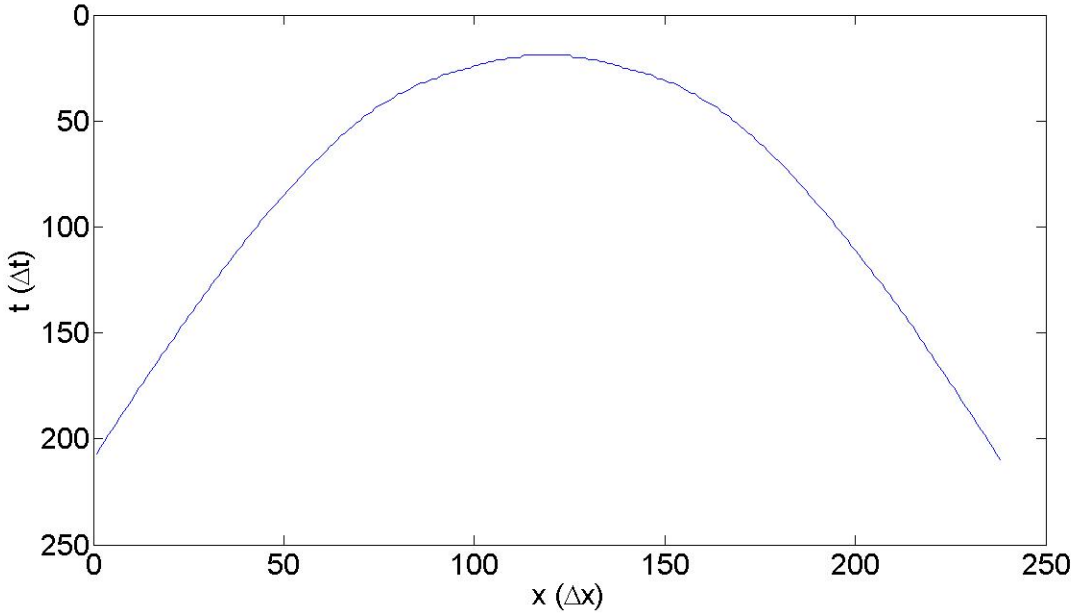

Figure B-13: Arch-like shape extracted from the B-scan image of slab D149W36

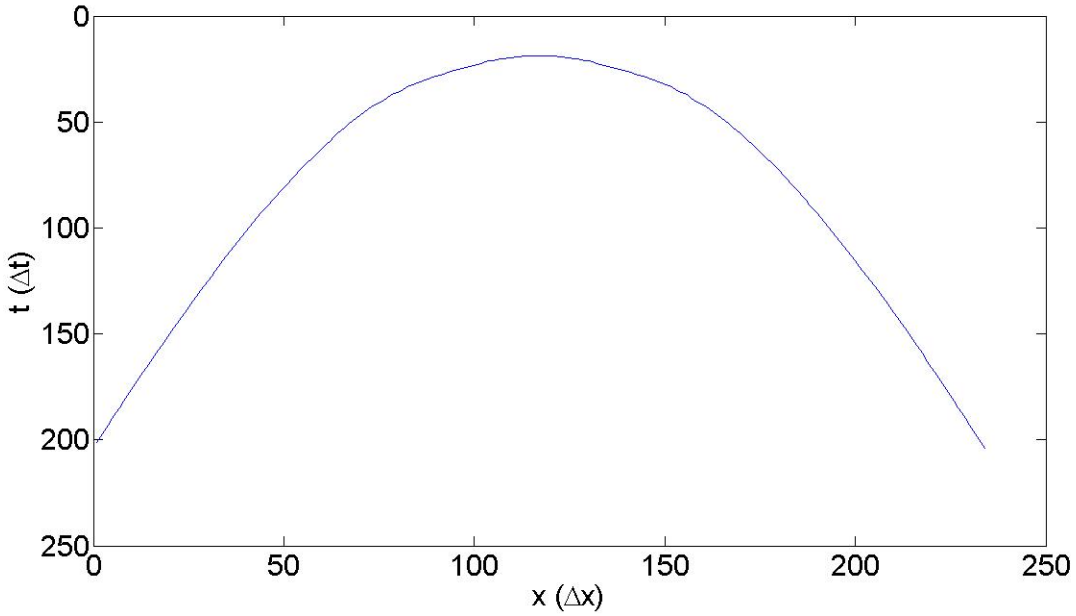

Figure B-14: Smoothened arch-like shape extracted from the B-scan image of slab D149W36

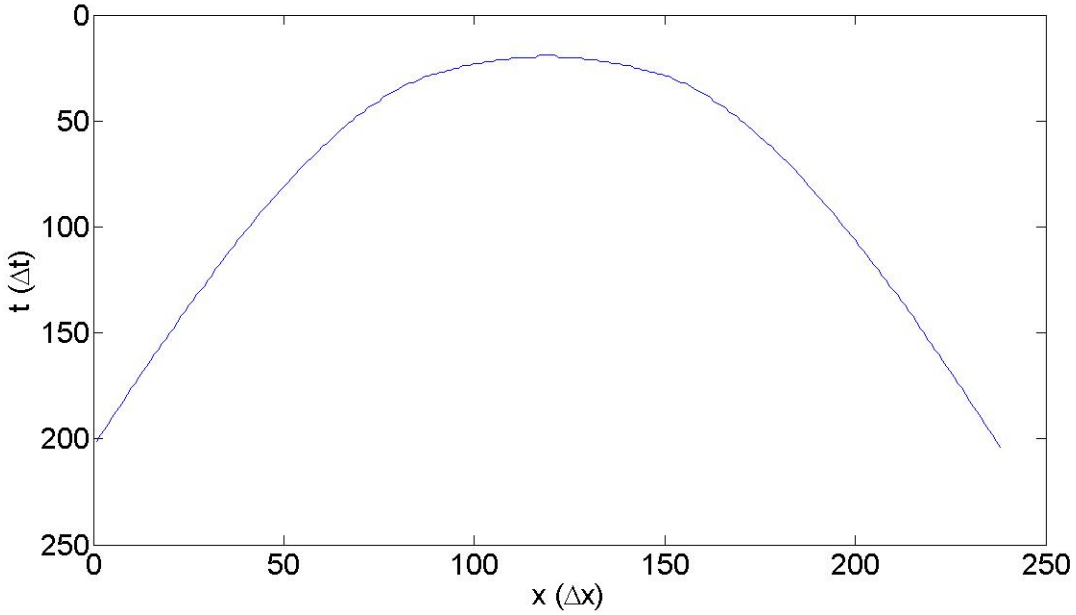

Figure B-15: Arch-like shape extracted from the B-scan image of slab D149W40

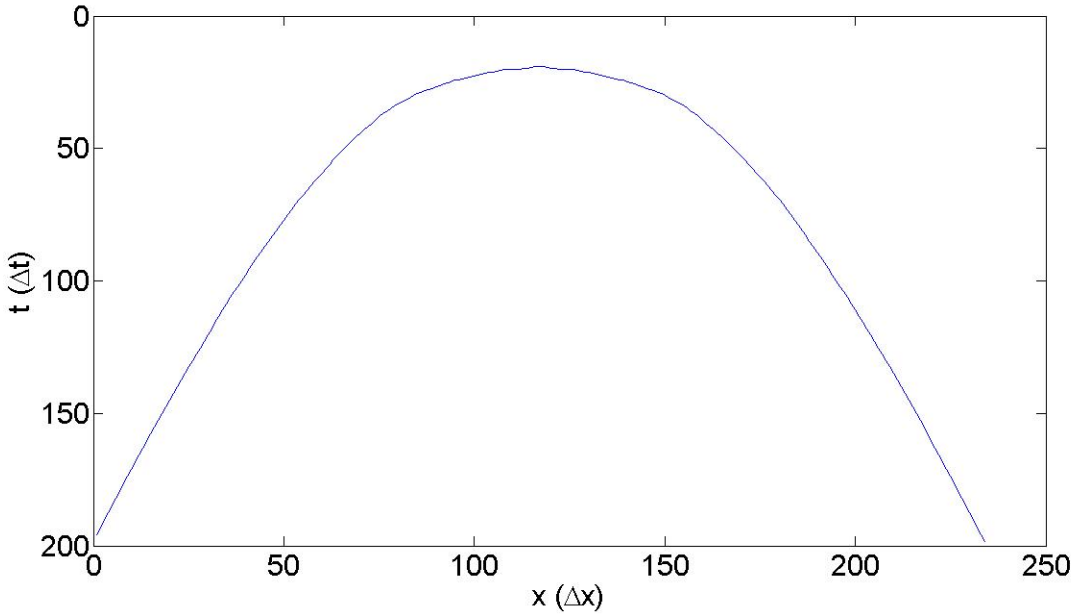

Figure B-16: Smoothened arch-like shape extracted from the B-scan image of slab D149W40

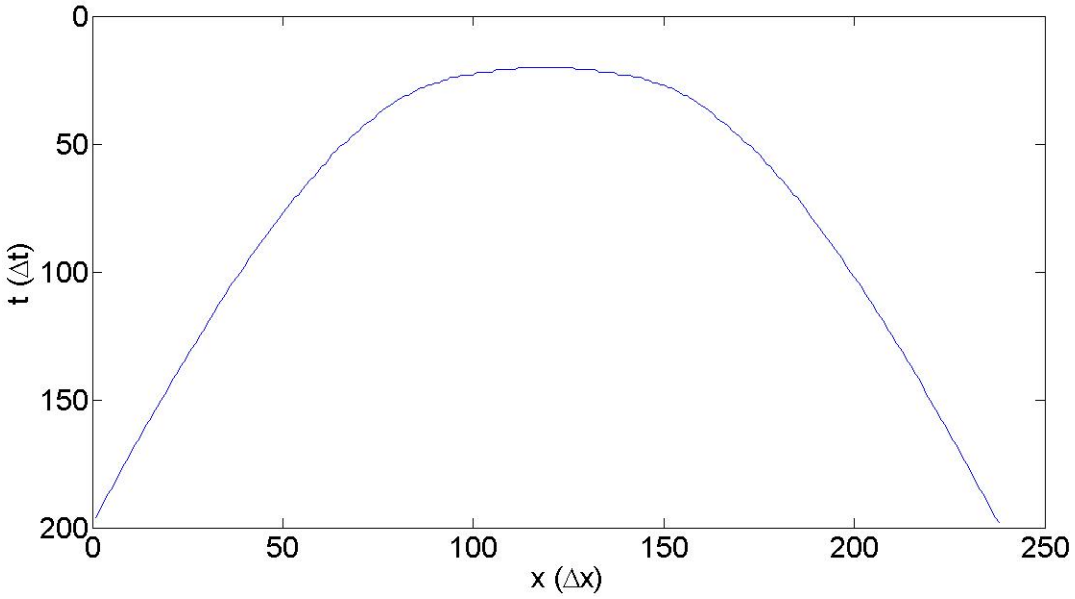

Figure B-17: Arch-like shape extracted from the B-scan image of slab D149W44

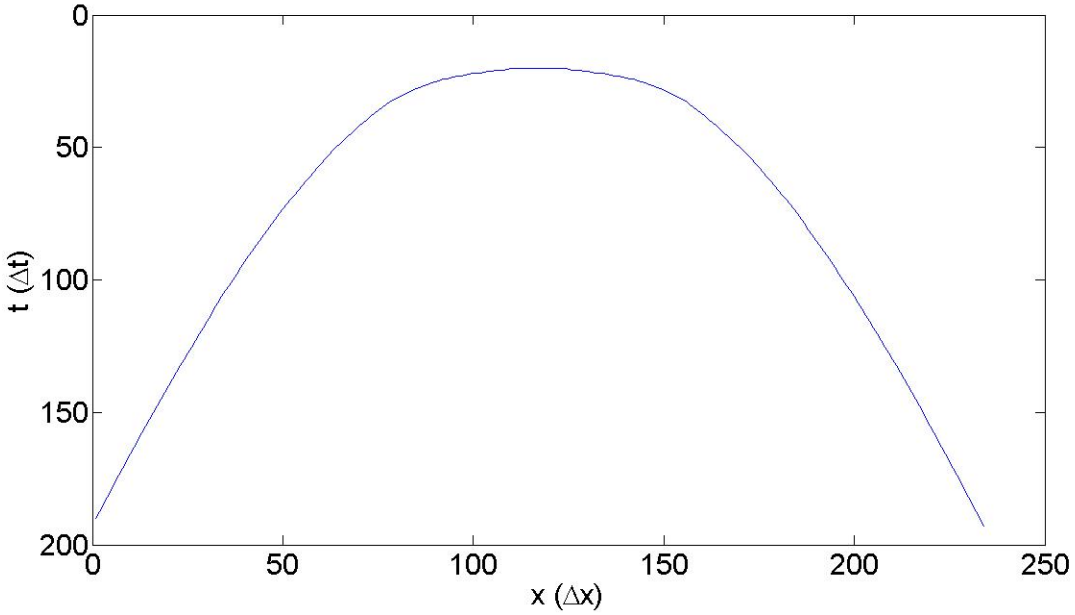

Figure B-18: Smoothened arch-like shape extracted from the B-scan image of slab D149W44

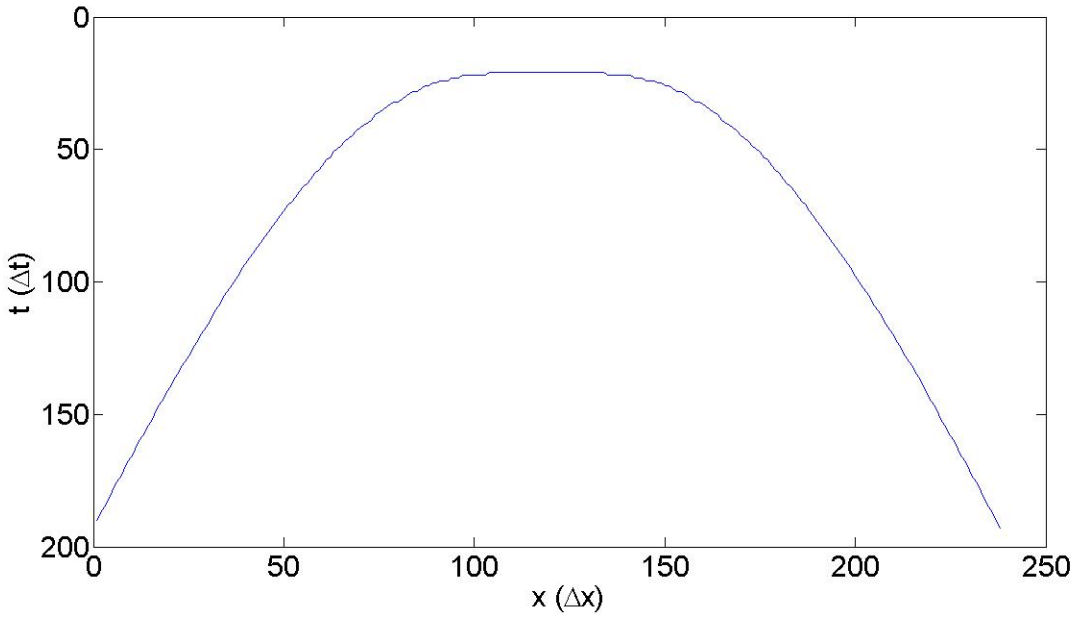

Figure B-19: Arch-like shape extracted from the B-scan image of slab D149W48

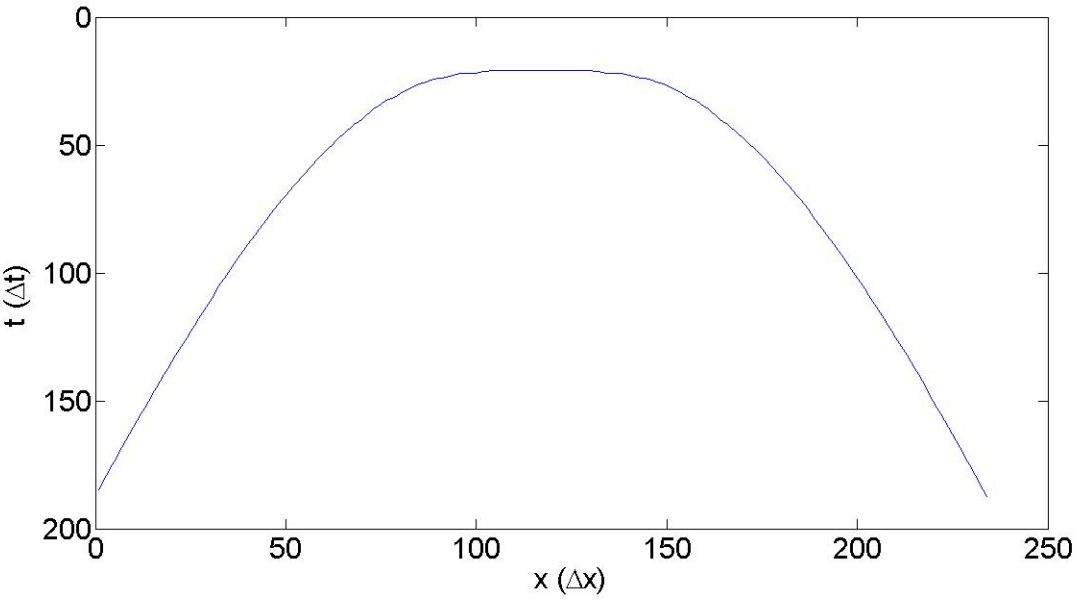

Figure B-20: Smoothened arch-like shape extracted from the B-scan image of slab D149W48

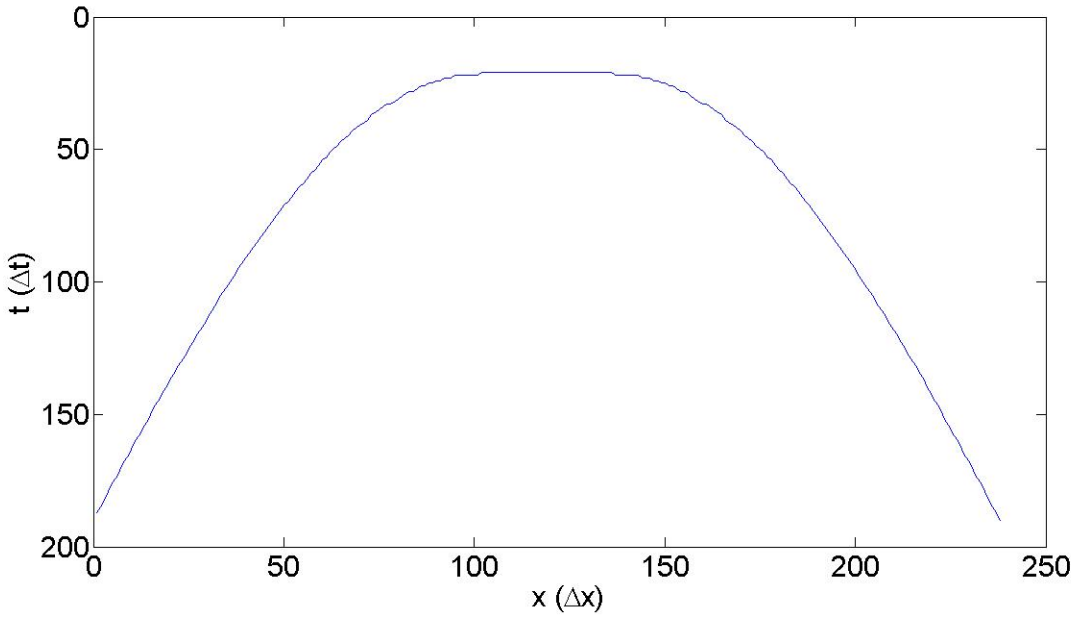

Figure B-21: Arch-like shape extracted from the B-scan image of slab D149W50

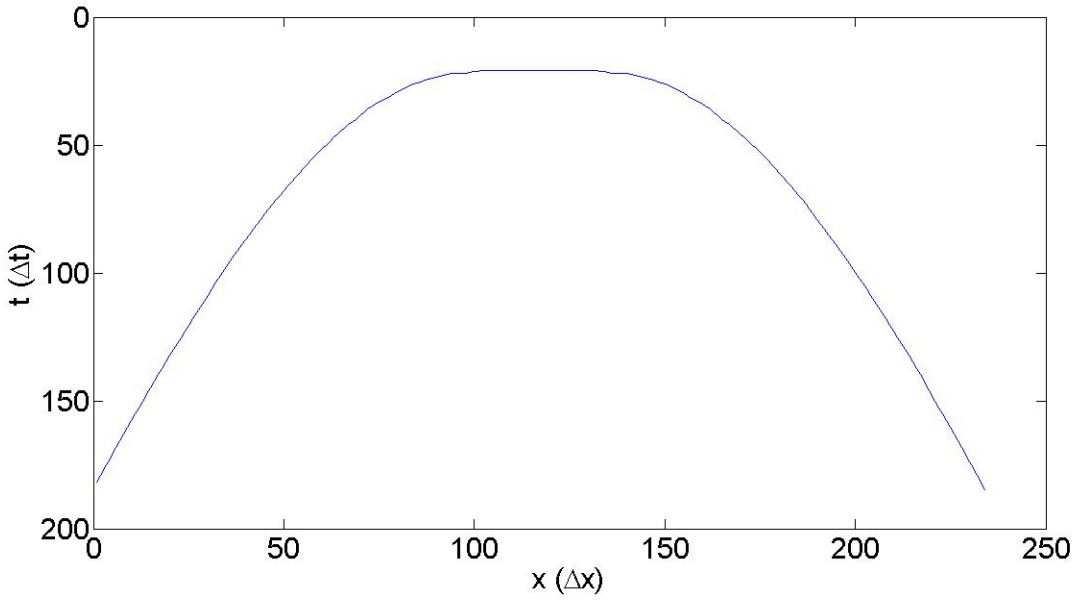

Figure B-22: Smoothened arch-like shape extracted from the B-scan image of slab D149W50

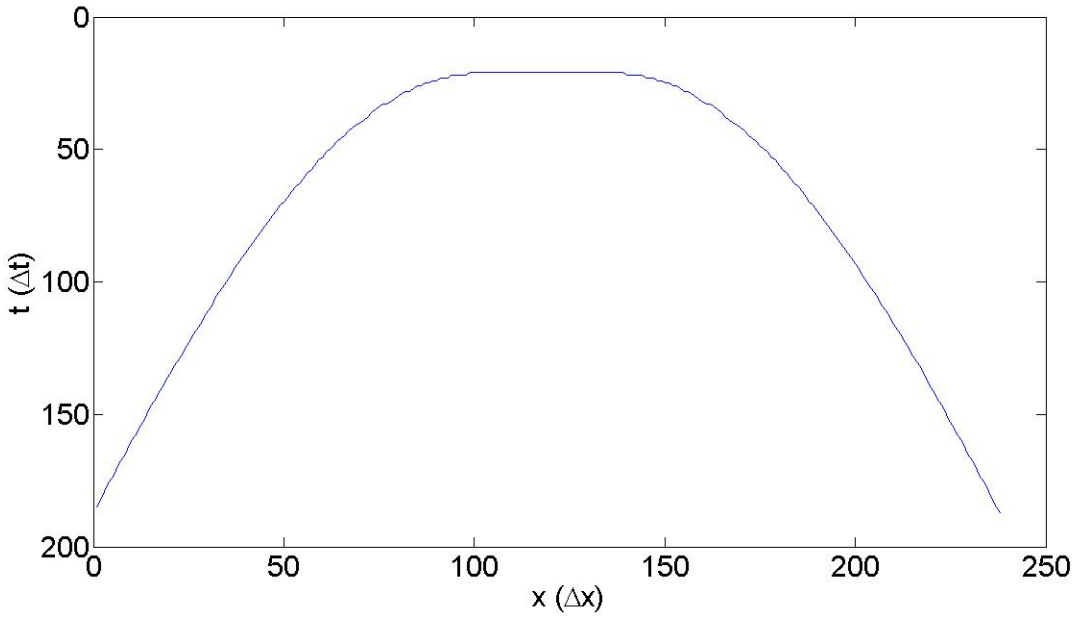

Figure B-23: Arch-like shape extracted from the B-scan image of slab D149W52

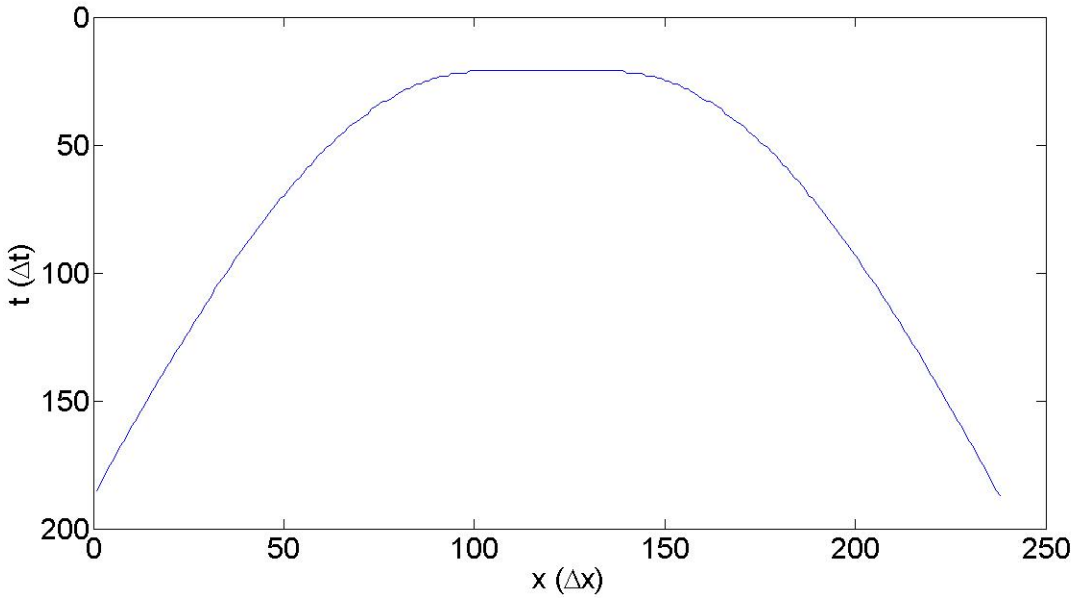

Figure B-24: Smoothened arch-like shape extracted from the B-scan image of slab D149W52

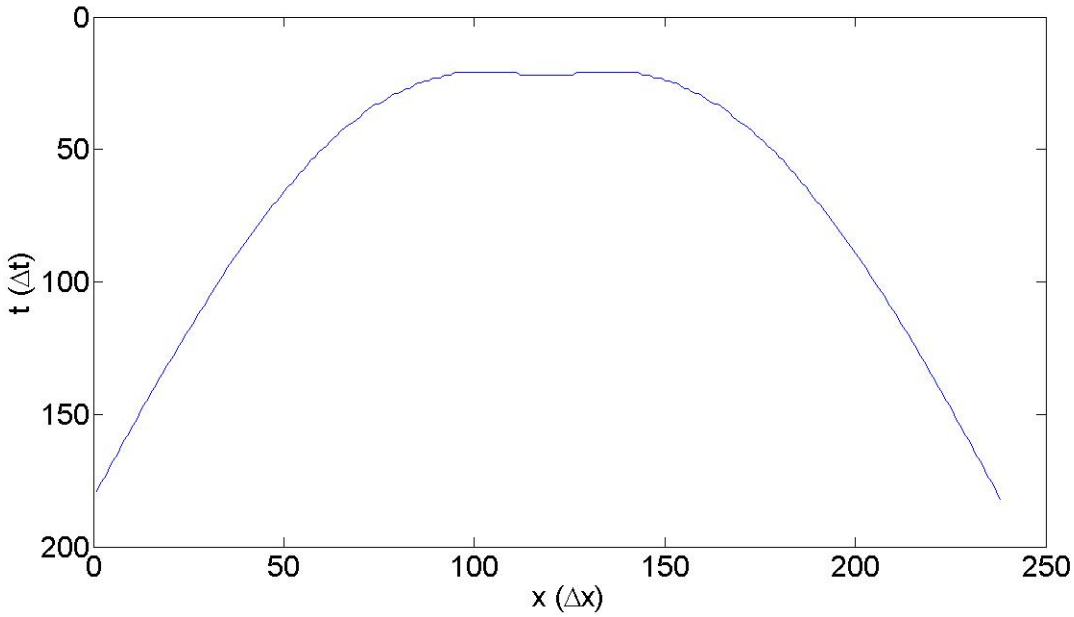

Figure B-25: Arch-like shape extracted from the B-scan image of slab D149W56

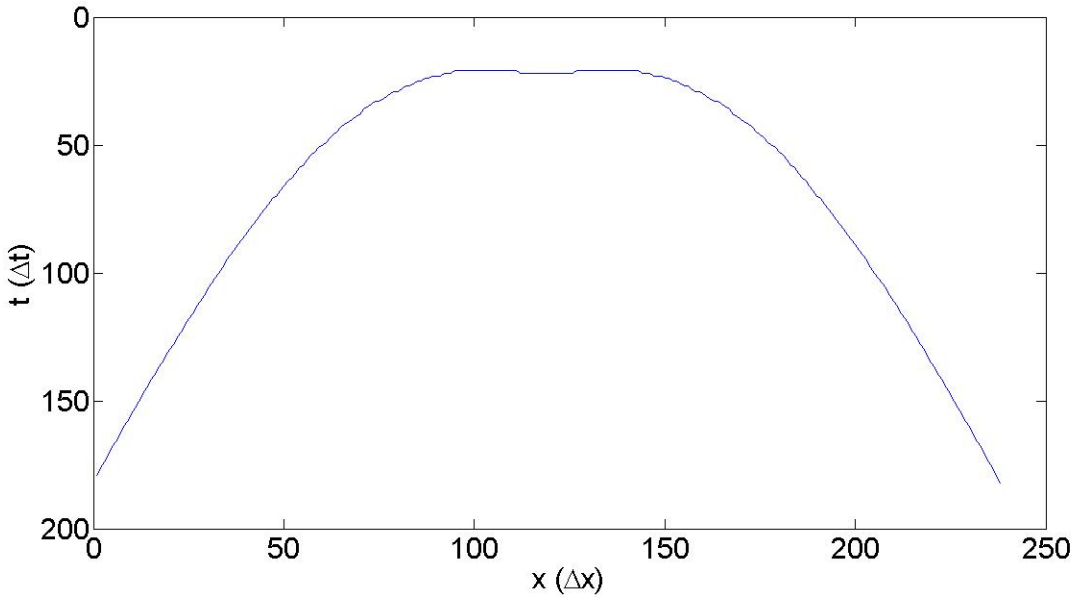

Figure B-26: Smoothened arch-like shape extracted from the B-scan image of slab D149W56

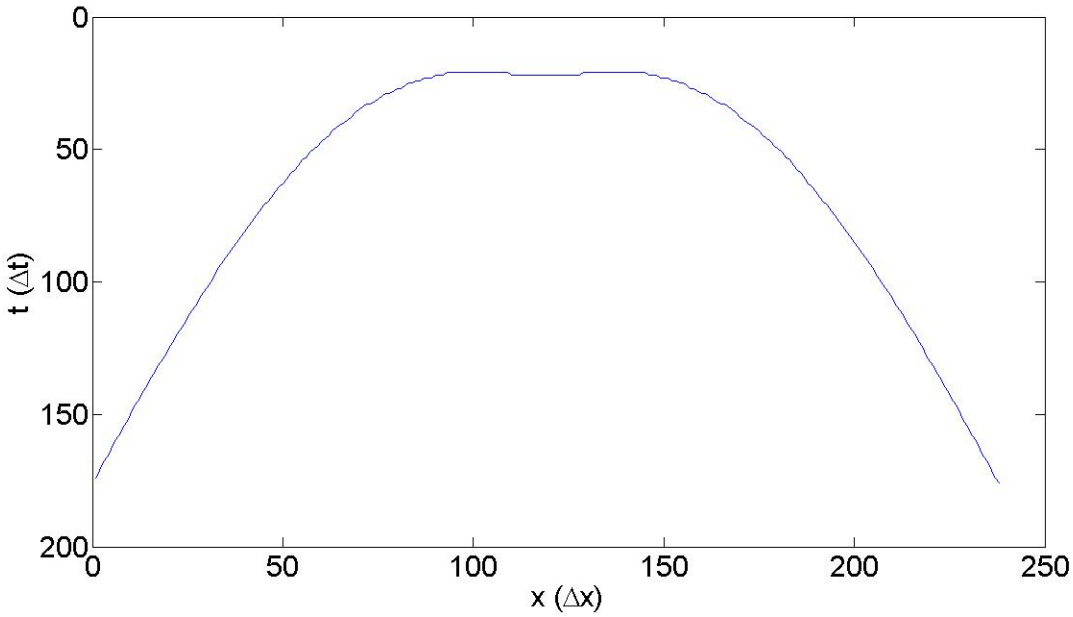

Figure B-27: Arch-like shape extracted from the B-scan image of slab D149W60

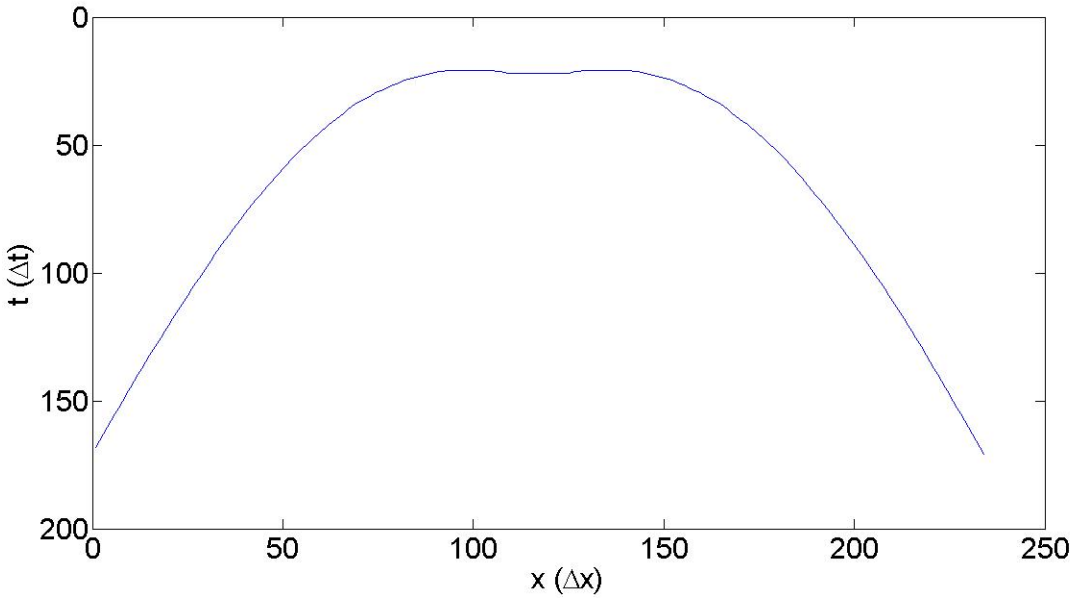

Figure B-28: Smoothened arch-like shape extracted from the B-scan image of slab D149W60

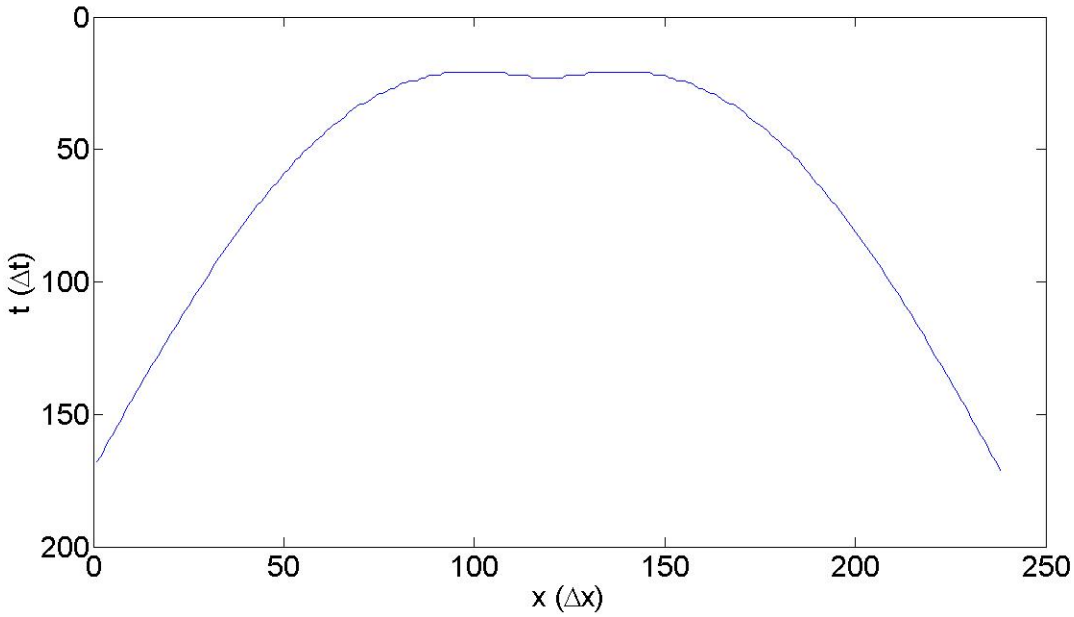

Figure B-29: Arch-like shape extracted from the B-scan image of slab D149W64

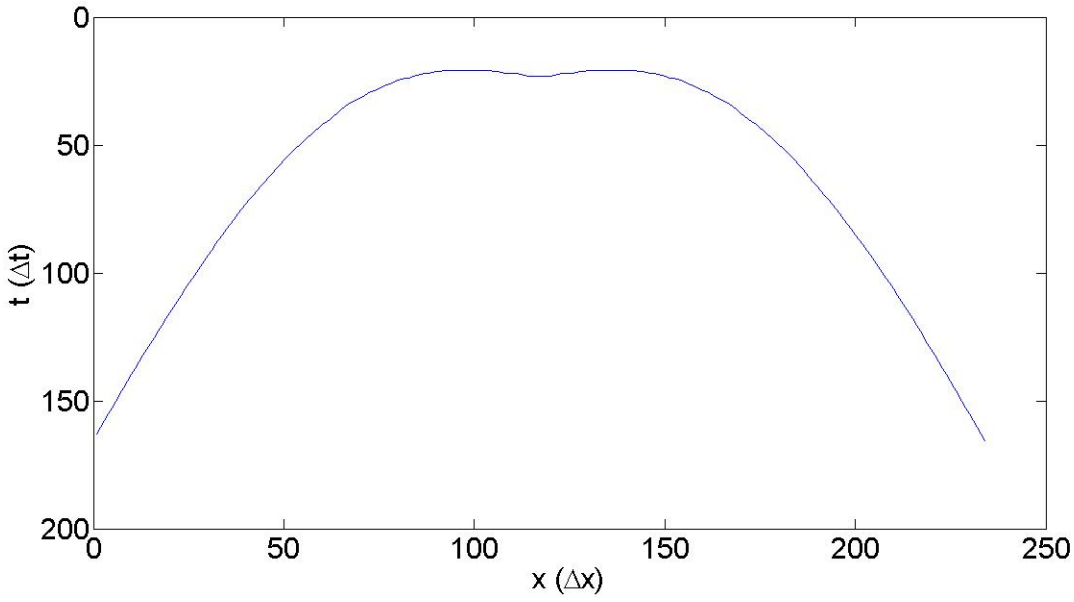

Figure B-30: Smoothened arch-like shape extracted from the B-scan image of slab D149W64

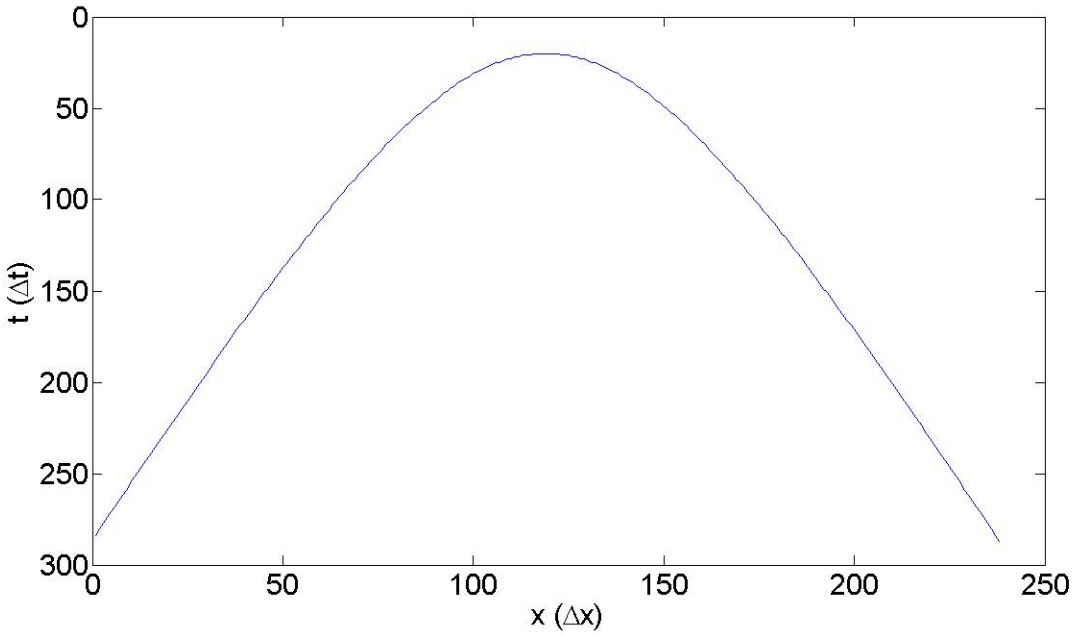

Figure B-31: Arch-like shape extracted from the B-scan image of slab D129W12

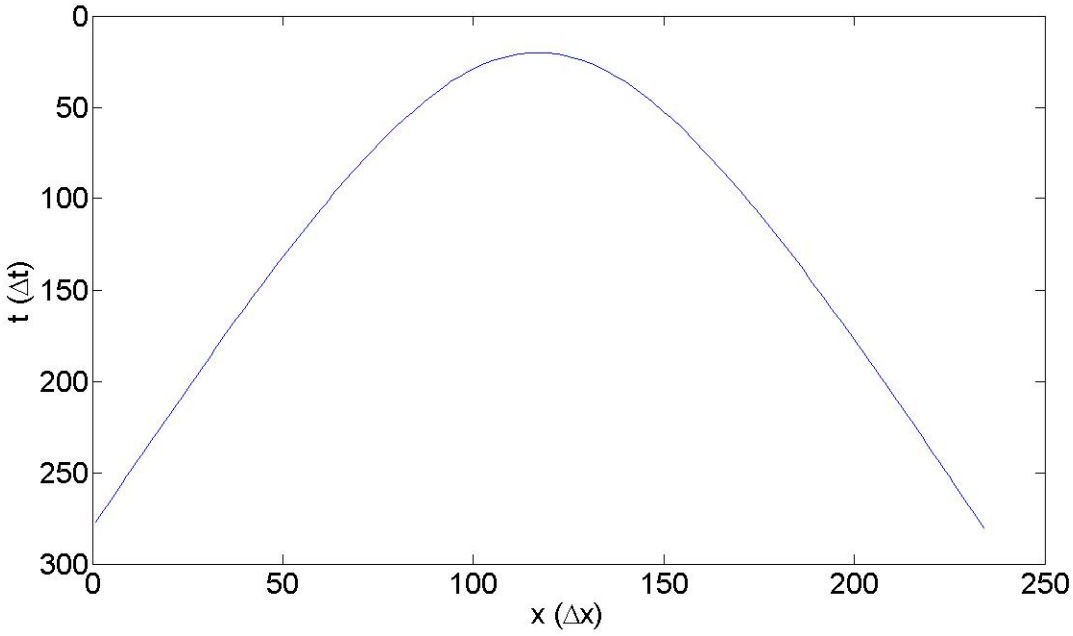

Figure B-32: Smoothened arch-like shape extracted from the B-scan image of slab D129W12

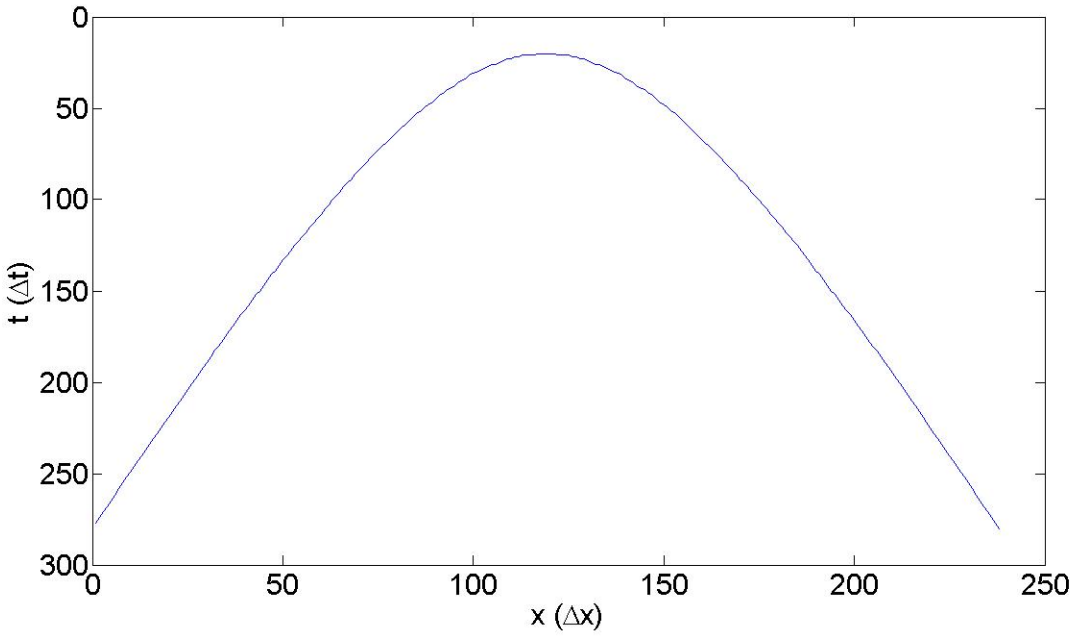

Figure B-33: Arch-like shape extracted from the B-scan image of slab D129W16

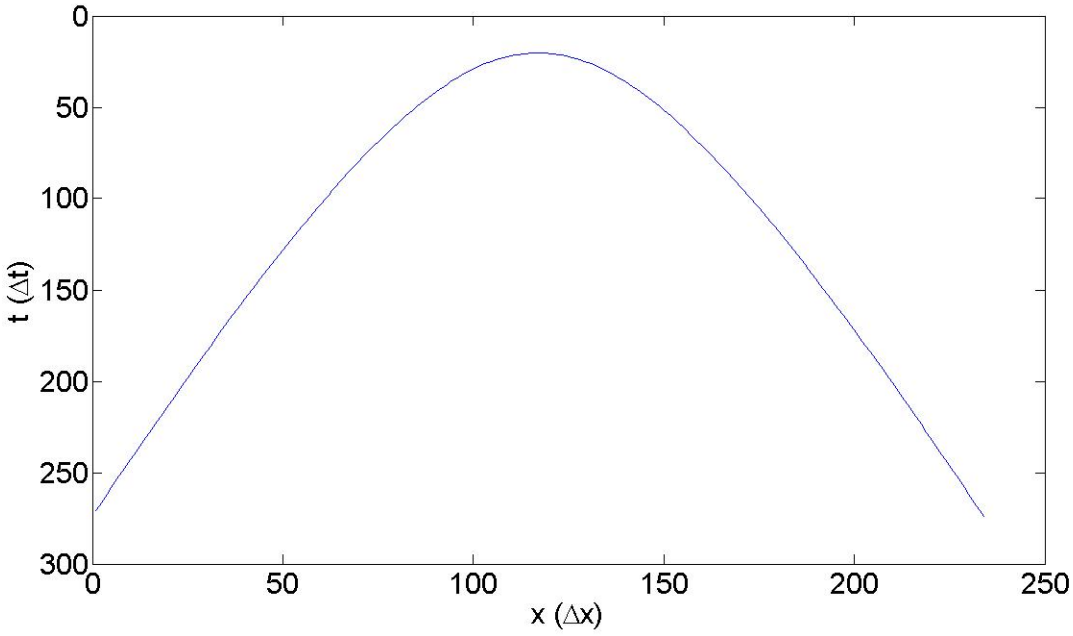

Figure B-34: Smoothened arch-like shape extracted from the B-scan image of slab D129W16

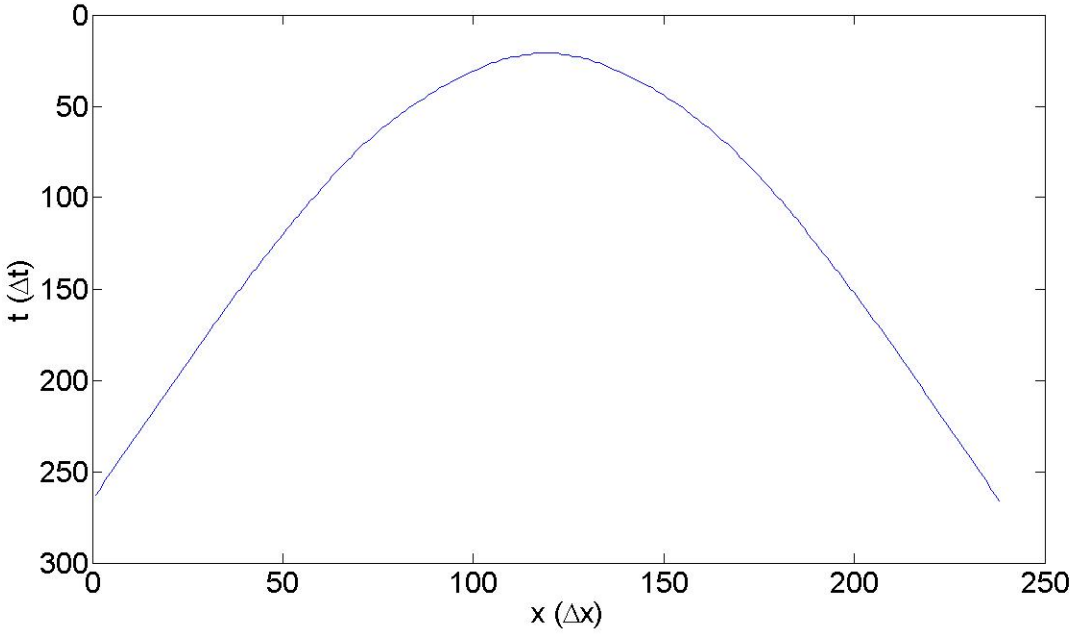

Figure B-35: Arch-like shape extracted from the B-scan image of slab D129W24

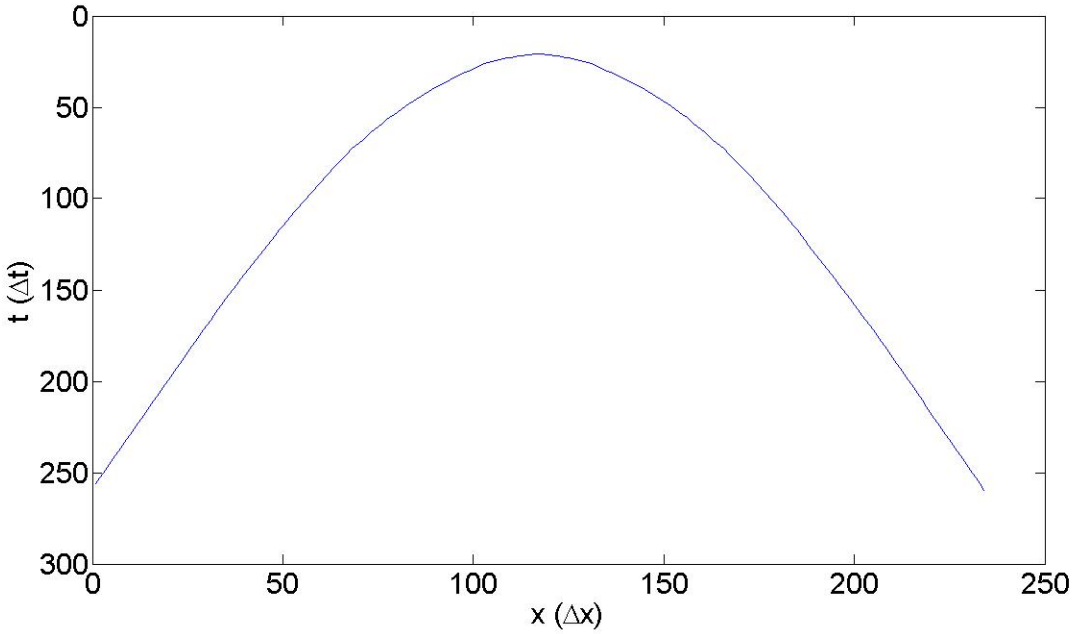

Figure B-36: Smoothened arch-like shape extracted from the B-scan image of slab D129W24

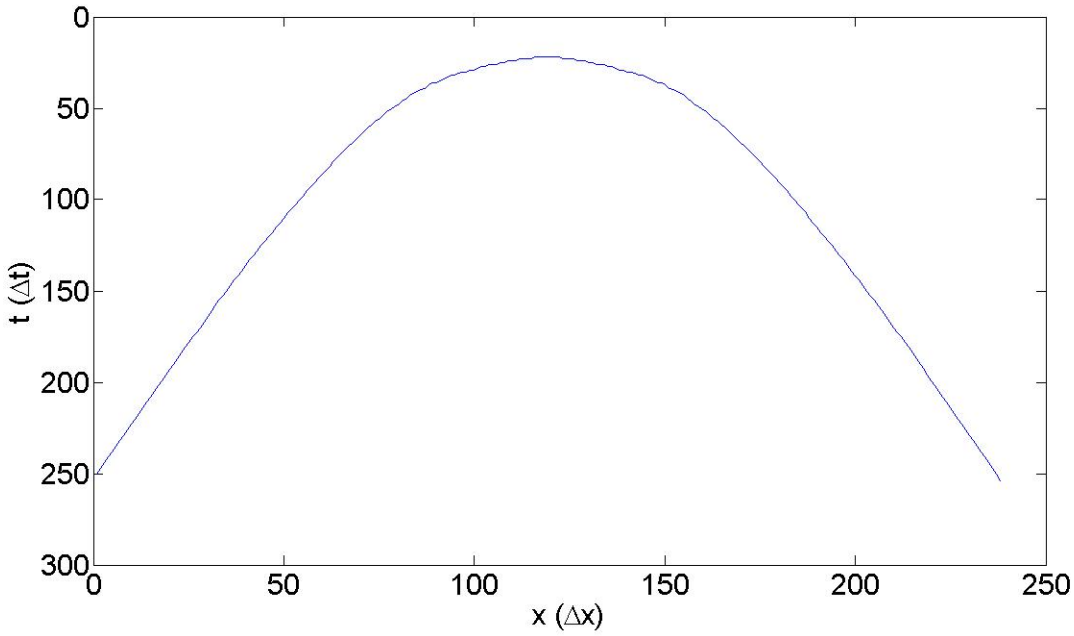

Figure B-37: Arch-like shape extracted from the B-scan image of slab D129W32

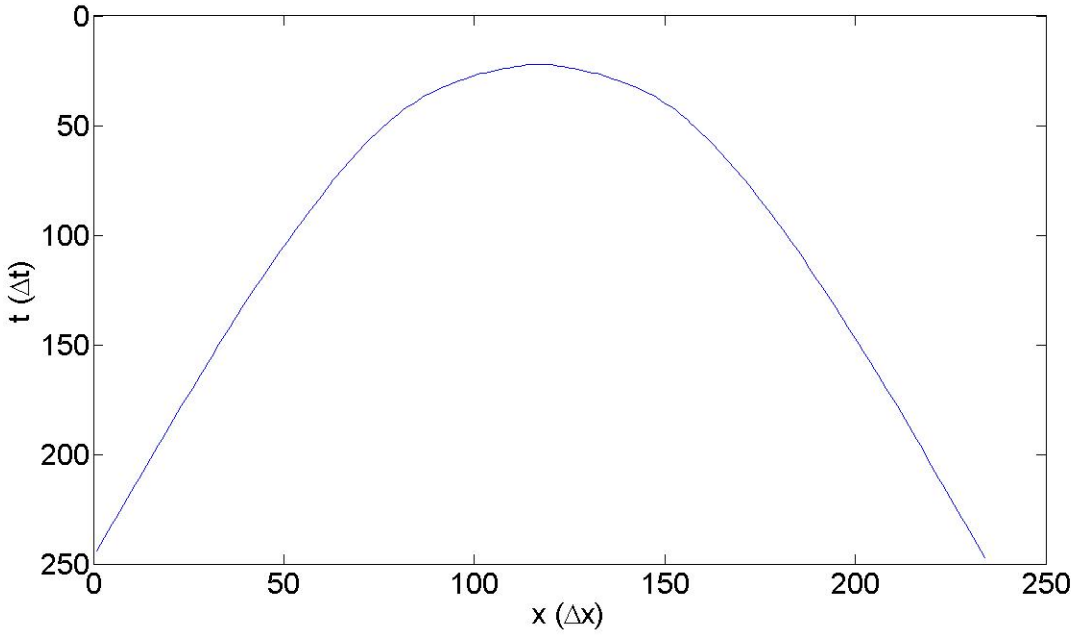

Figure B-38: Smoothened arch-like shape extracted from the B-scan image of slab D129W36

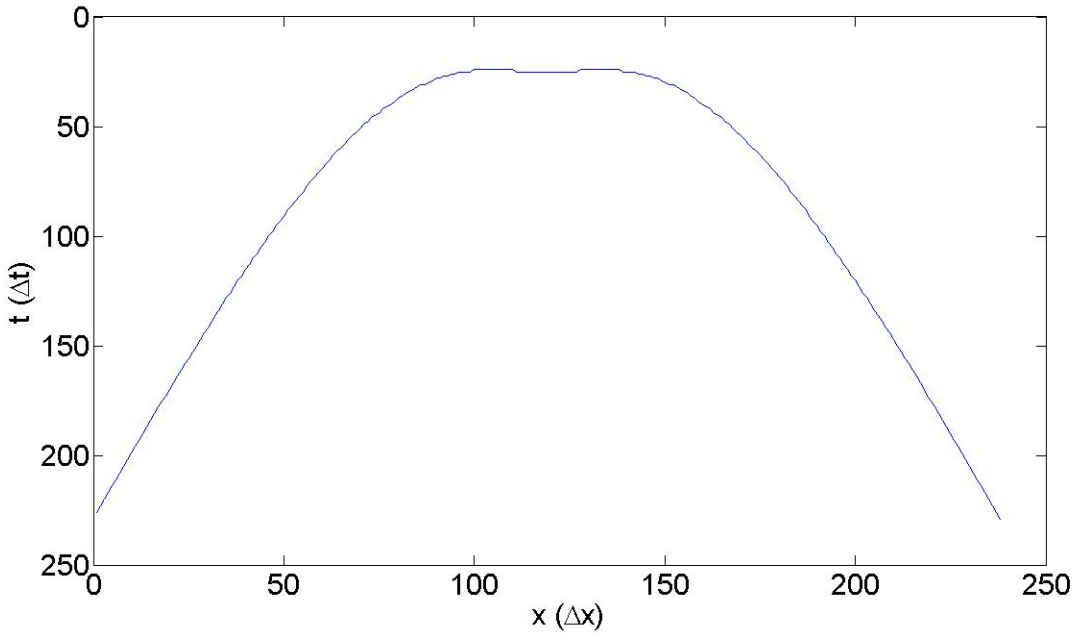

Figure B-39: Arch-like shape extracted from the B-scan image of slab D129W48

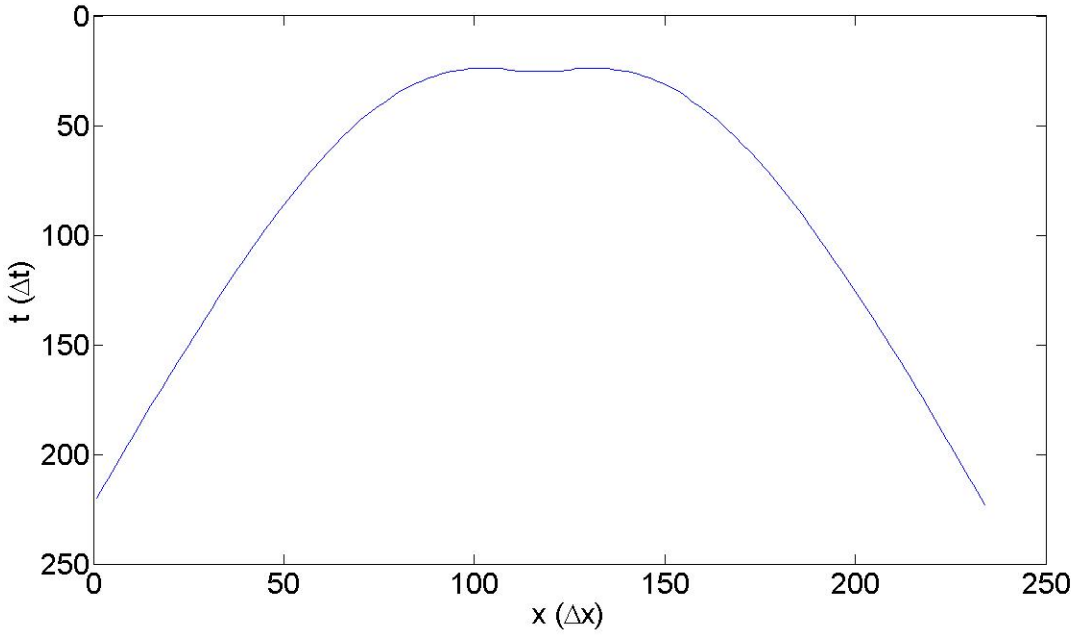

Figure B-40: Smoothened arch-like shape extracted from the B-scan image of slab D129W48

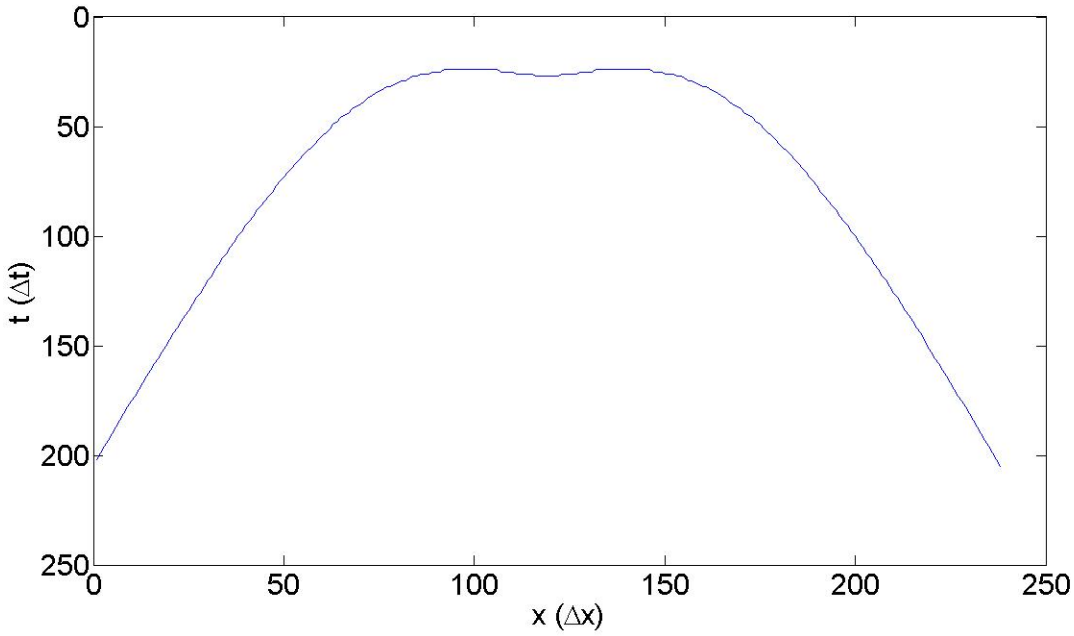

Figure B-41: Arch-like shape extracted from the B-scan image of slab D129W64

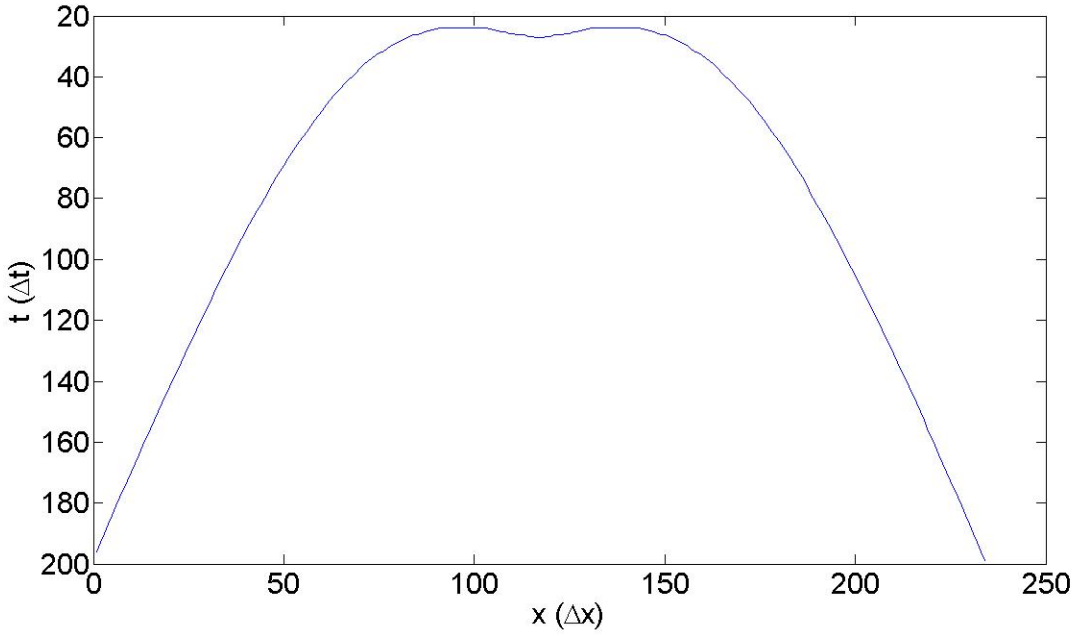

Figure B-42: Smoothened arch-like shape extracted from the B-scan image of slab D129W164

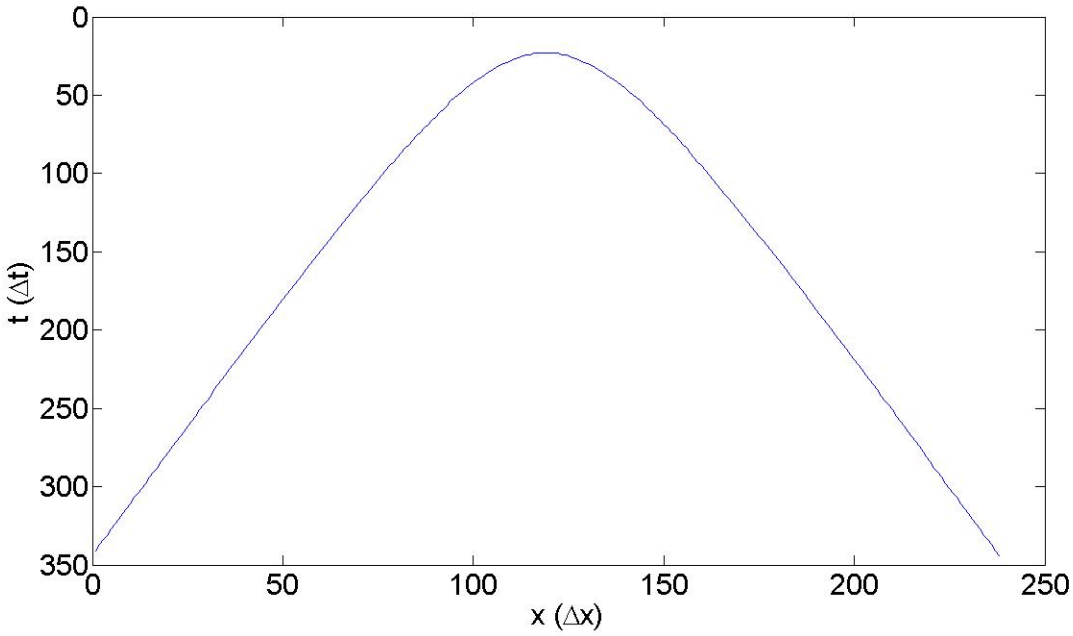

Figure B-43: Arch-like shape extracted from the B-scan image of slab D109W12

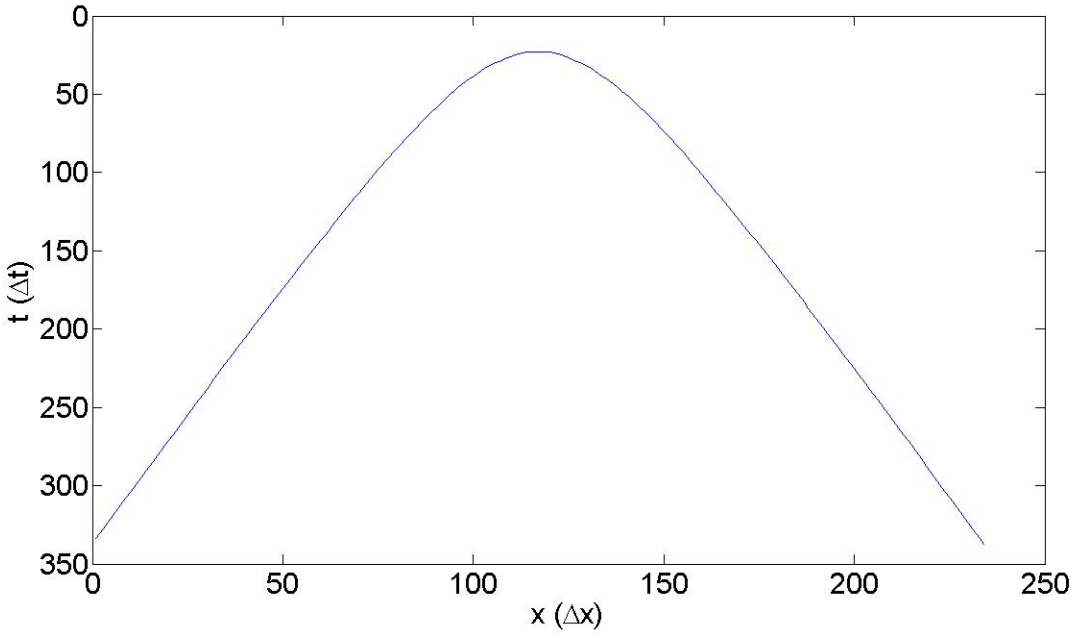

Figure B-44: Smoothened arch-like shape extracted from the B-scan image of slab D109W12

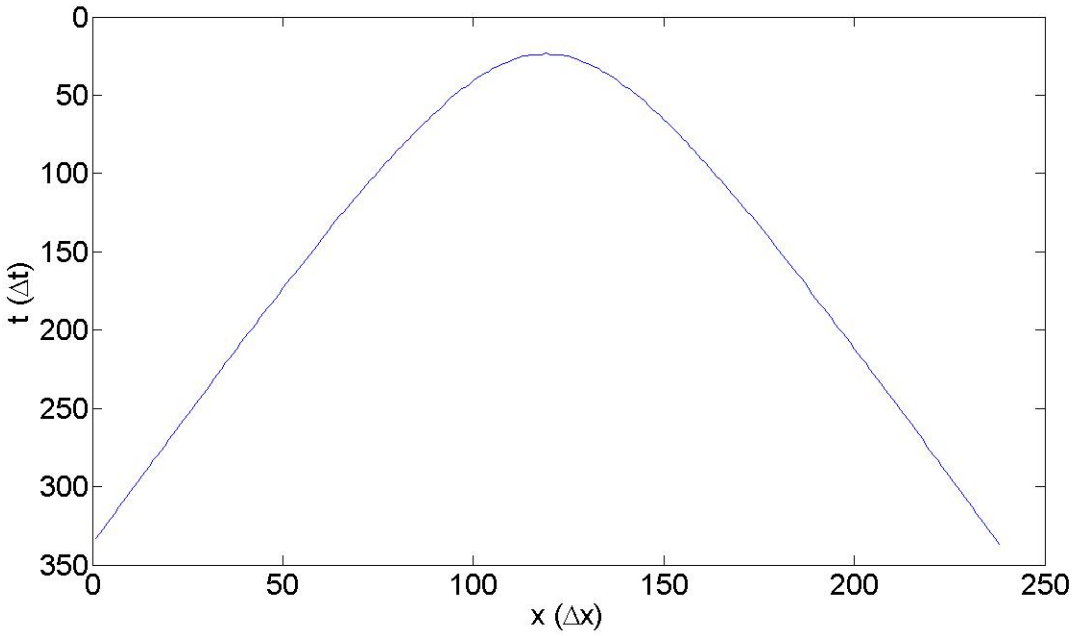

Figure B-45: Arch-like shape extracted from the B-scan image of slab D109W16

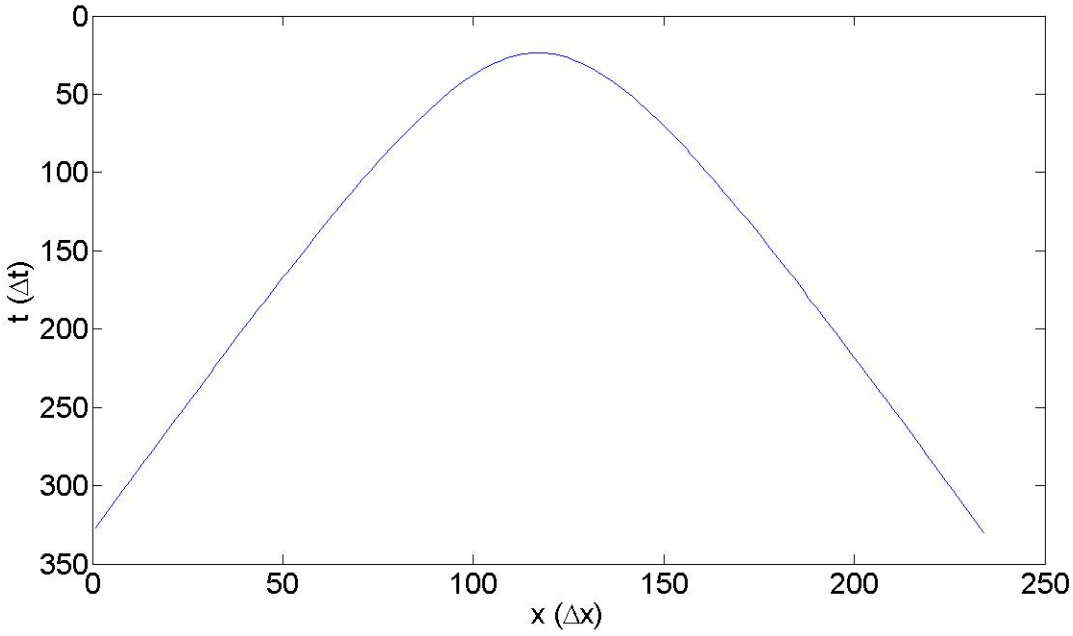

Figure B-46: Smoothened arch-like shape extracted from the B-scan image of slab D109W16

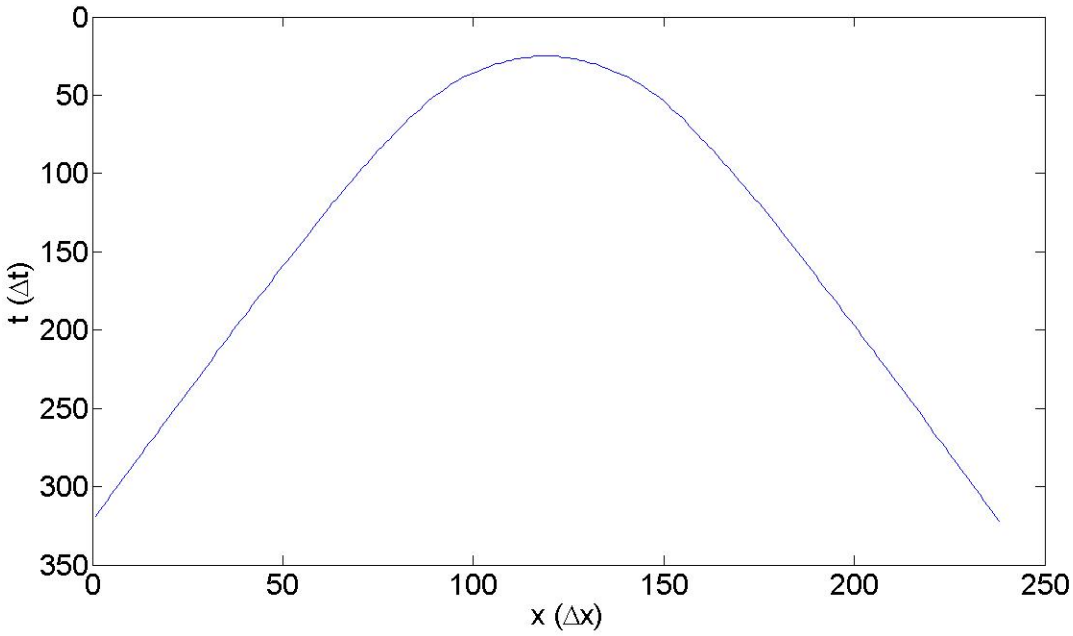

Figure B-47: Arch-like shape extracted from the B-scan image of slab D109W24

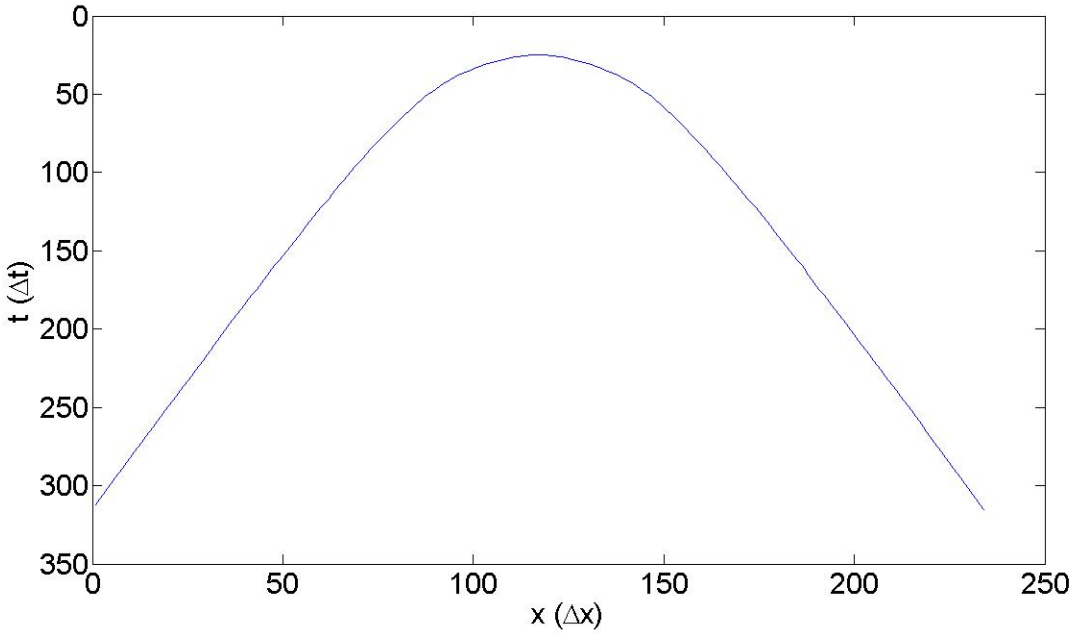

Figure B-48: Smoothened arch-like shape extracted from the B-scan image of slab D109W24

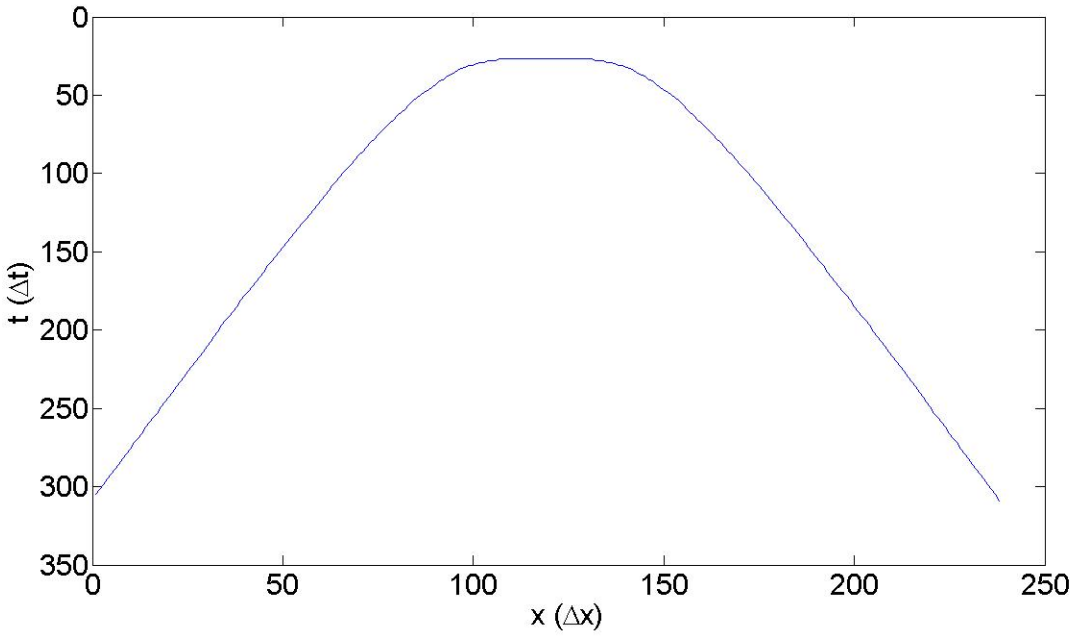

Figure B-49: Arch-like shape extracted from the B-scan image of slab D109W32

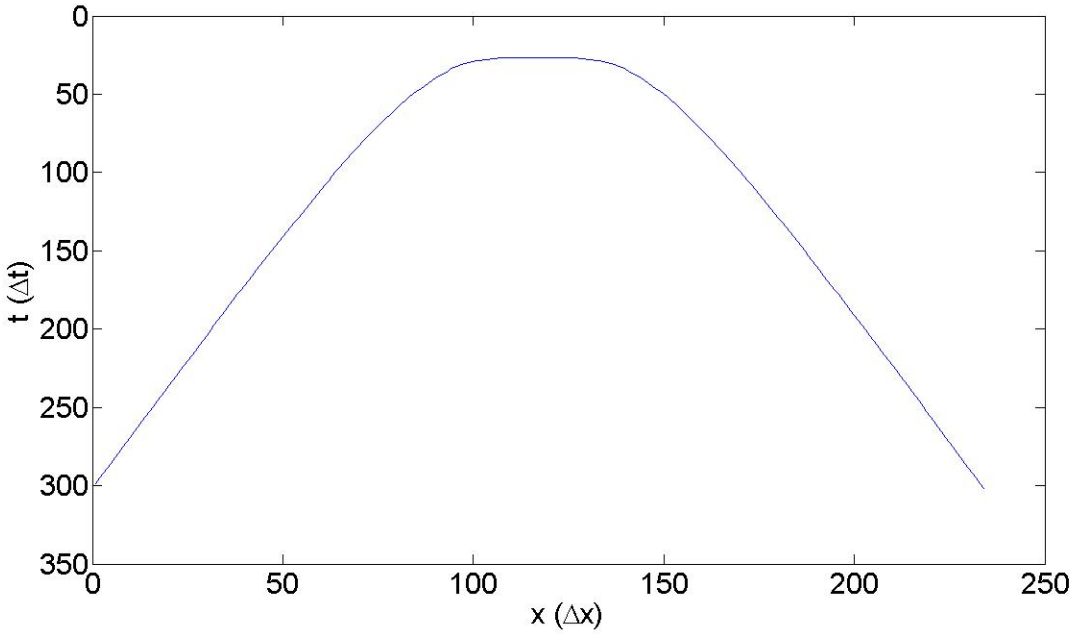

Figure B-50: Smoothened arch-like shape extracted from the B-scan image of slab D109W32

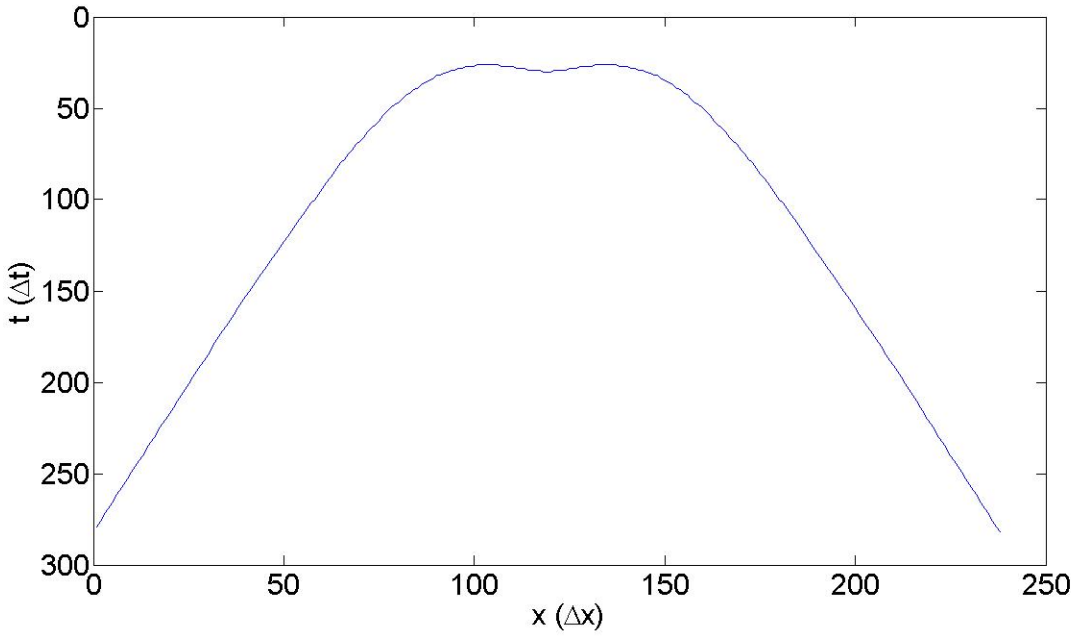

Figure B-51: Arch-like shape extracted from the B-scan image of slab D109W48

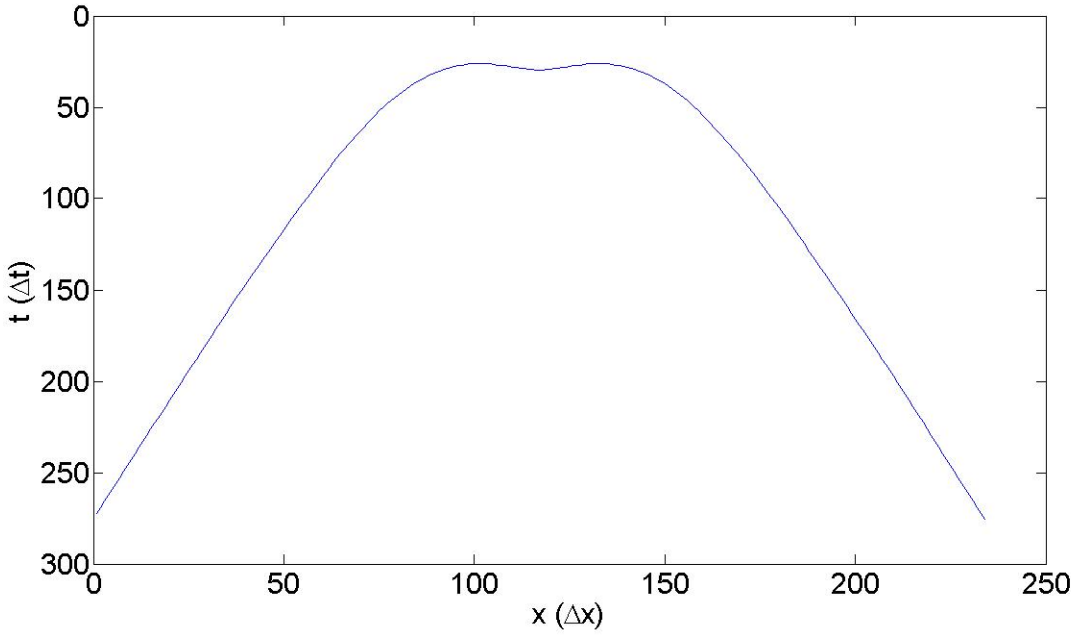

Figure B-52: Smoothened arch-like shape extracted from the B-scan image of slab D109W48

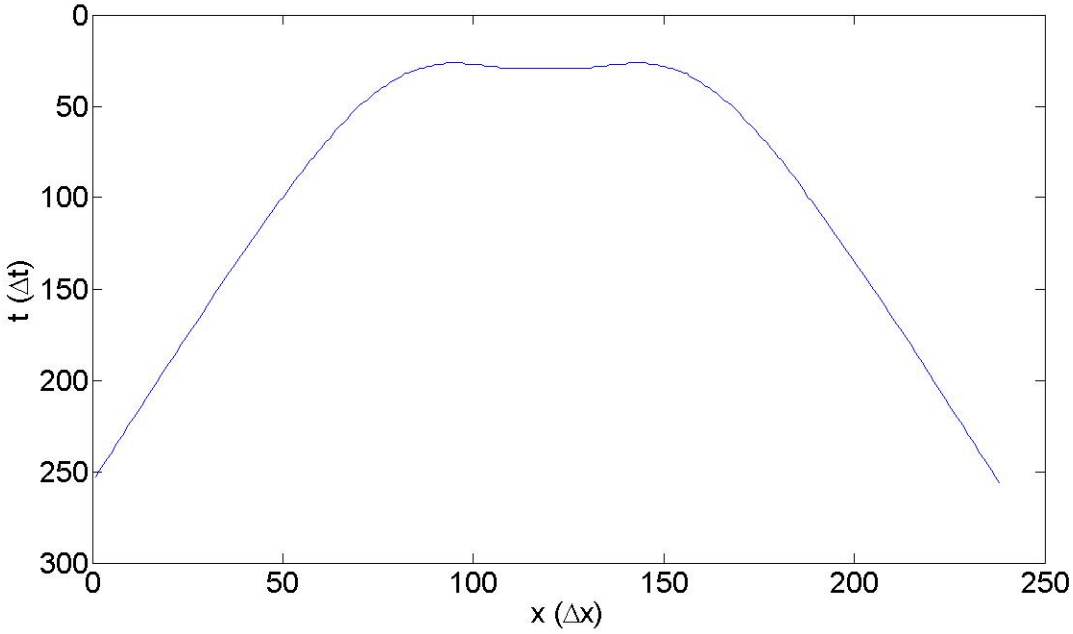

Figure B-53: Arch-like shape extracted from the B-scan image of slab D109W64

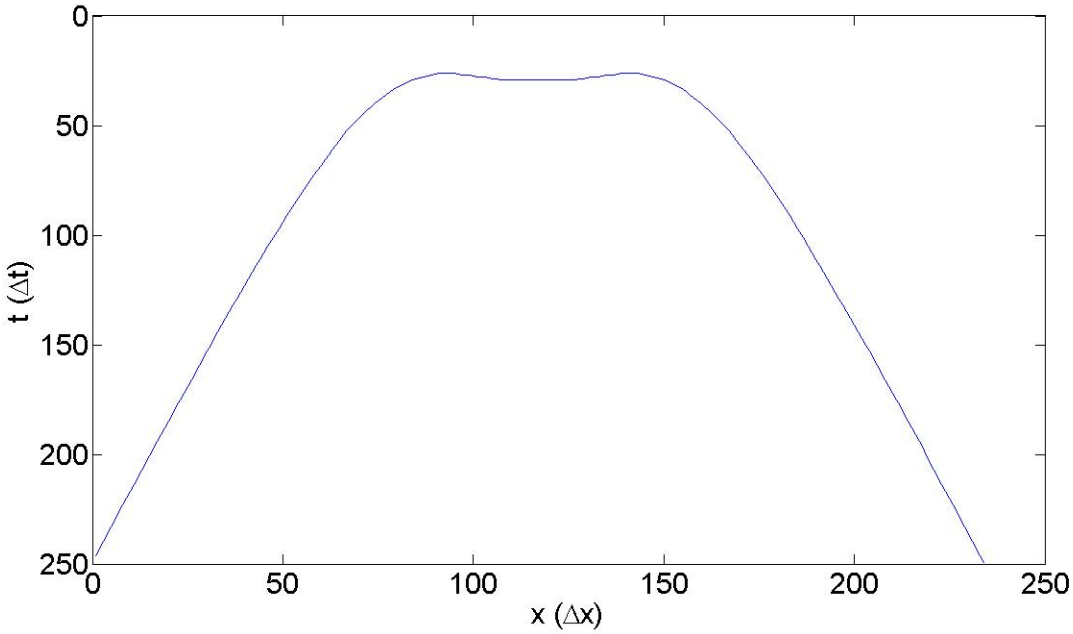

Figure B-54: Smoothened arch-like shape extracted from the B-scan image of slab D109W64

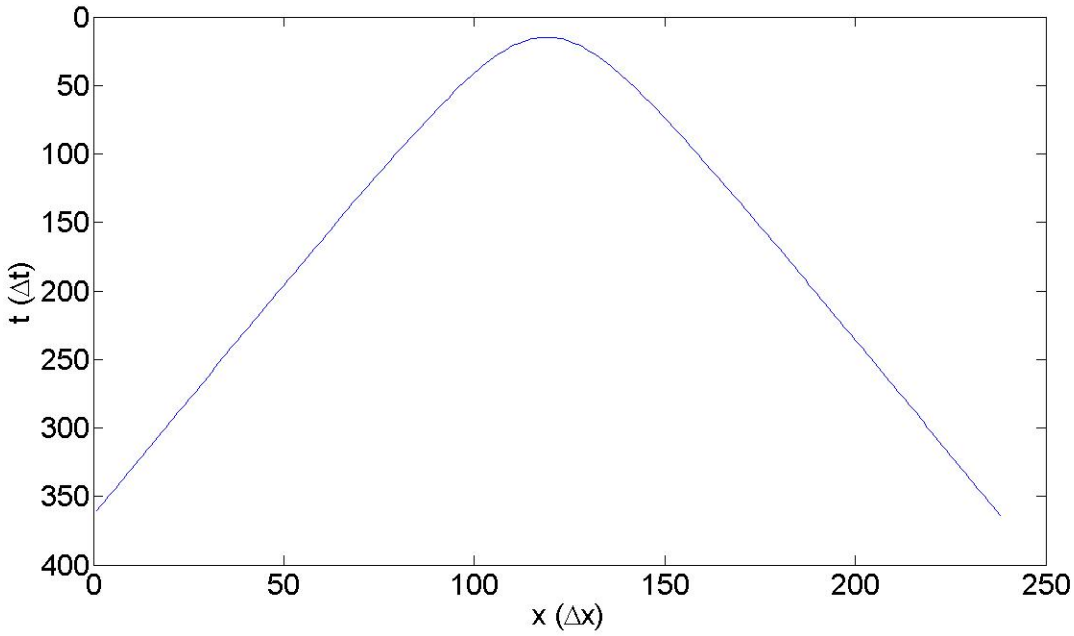

Figure B-55: Arch-like shape extracted from the B-scan image of slab D99W12

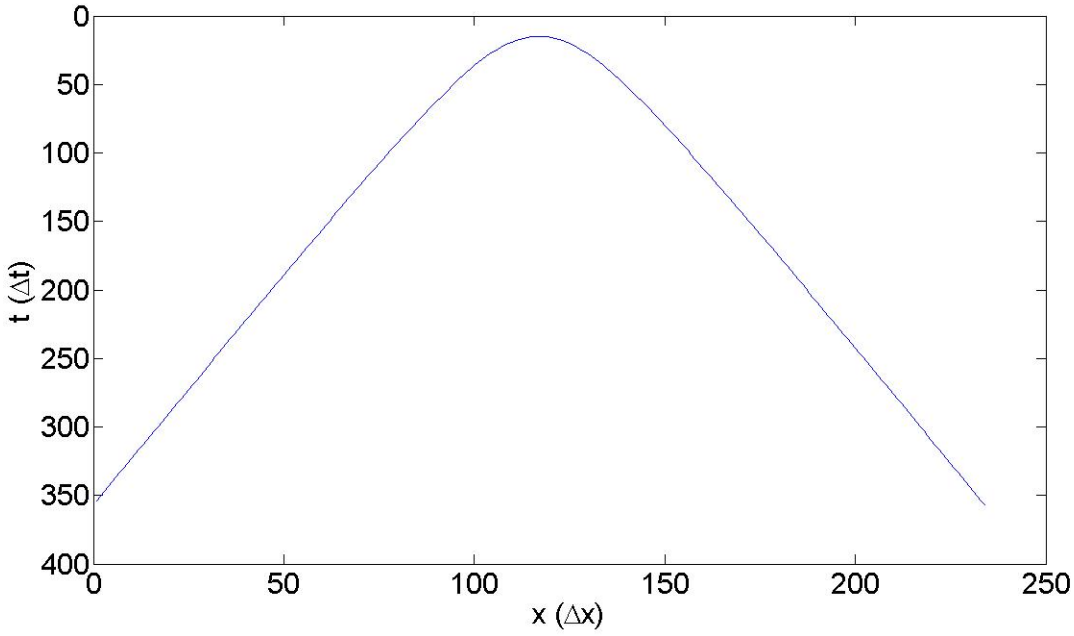

Figure B-56: Smoothened arch-like shape extracted from the B-scan image of slab D99W12

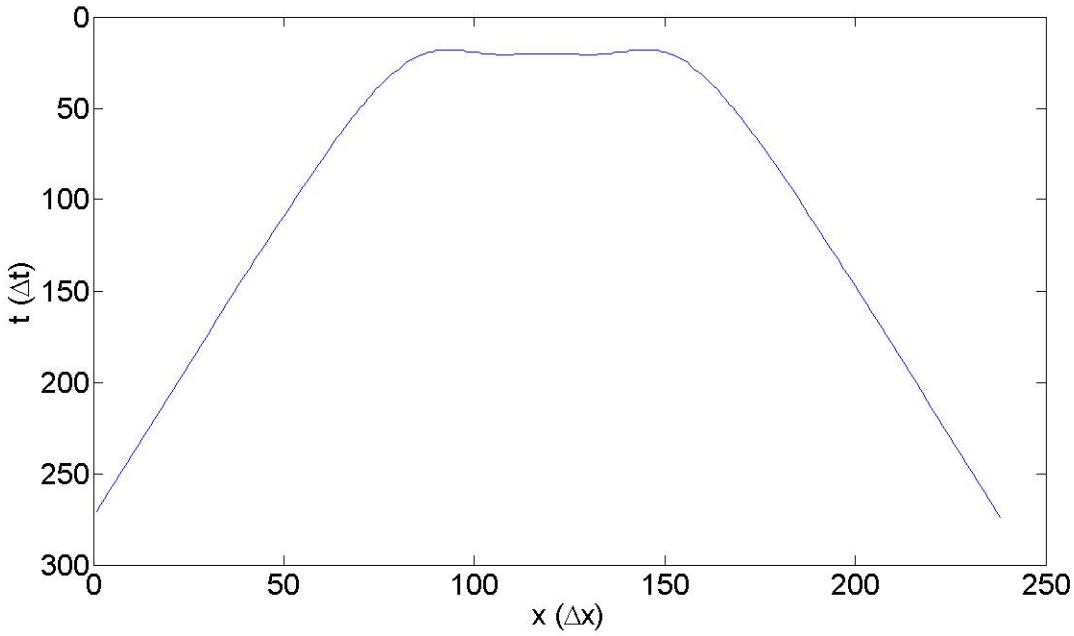

Figure B-57: Arch-like shape extracted from the B-scan image of slab D99W64

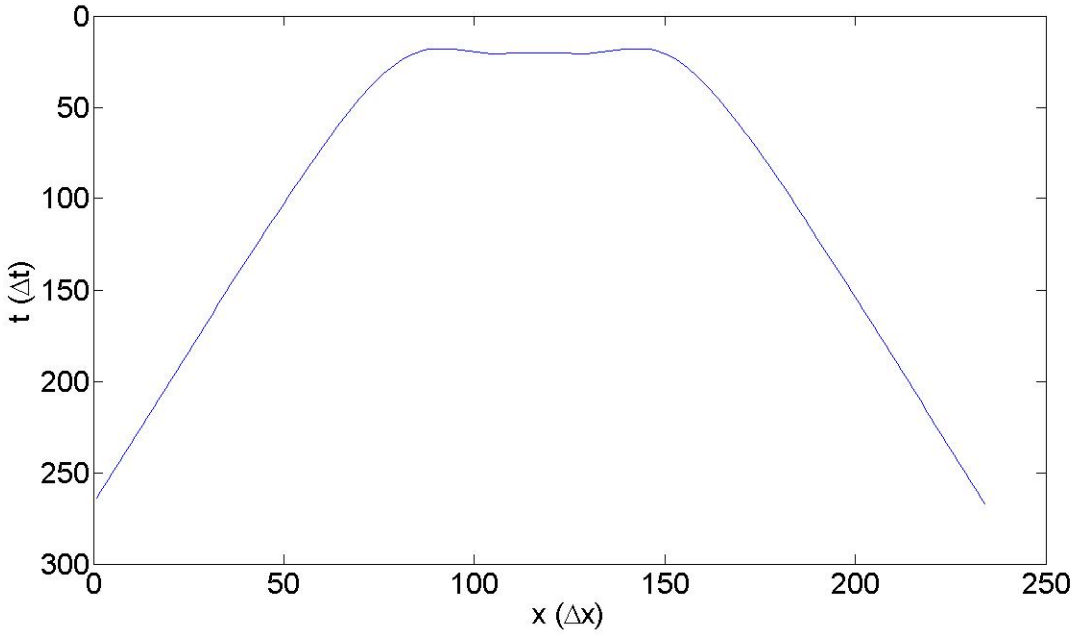

Figure B-58: Smoothened arch-like shape extracted from the B-scan image of slab D99W64

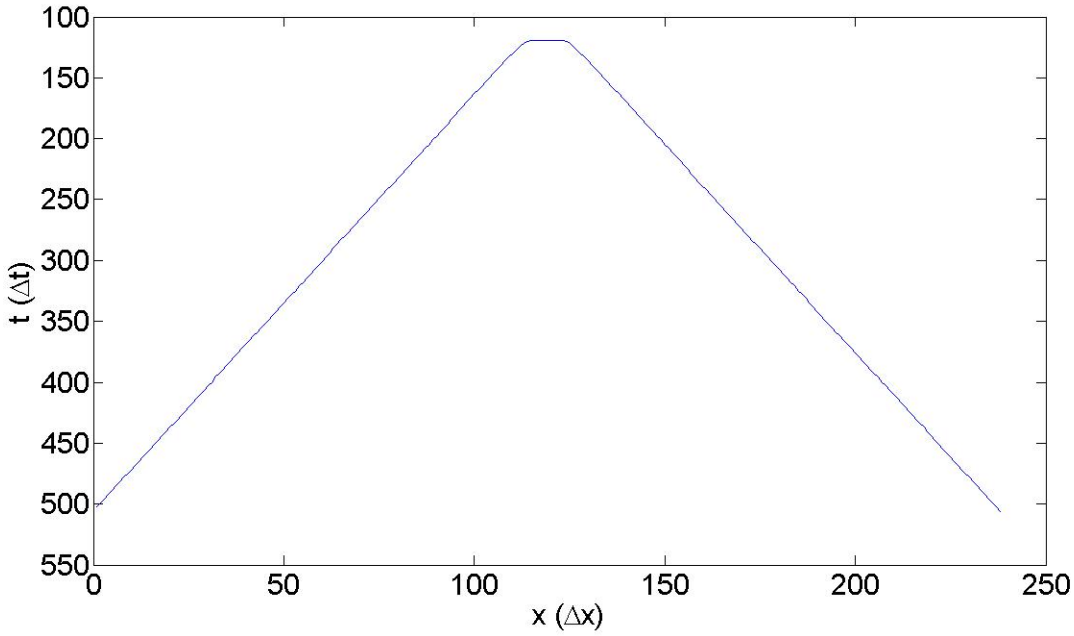

Figure B-59: Arch-like shape extracted from the B-scan image of slab D89W12

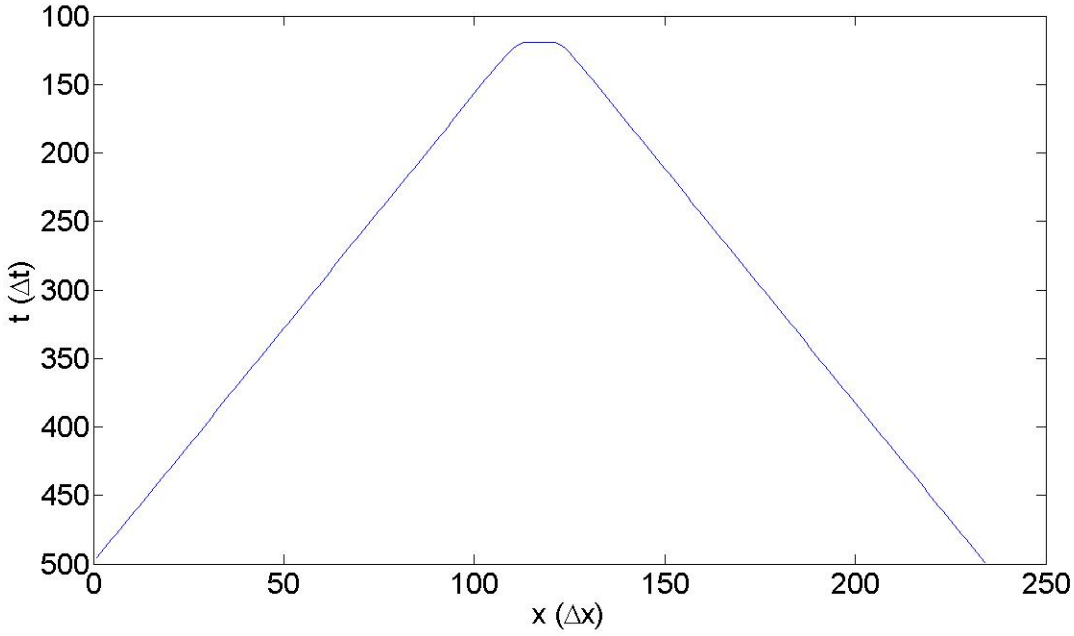

Figure B-60: Smoothened arch-like shape extracted from the B-scan image of slab D89W12

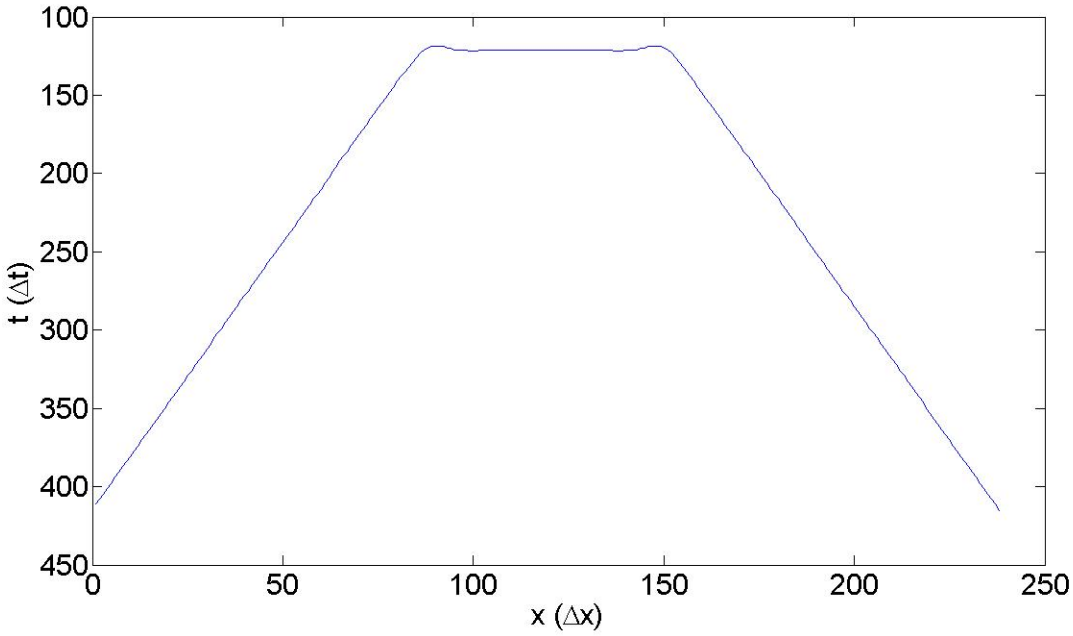

Figure B-61: Arch-like shape extracted from the B-scan image of slab D89W64

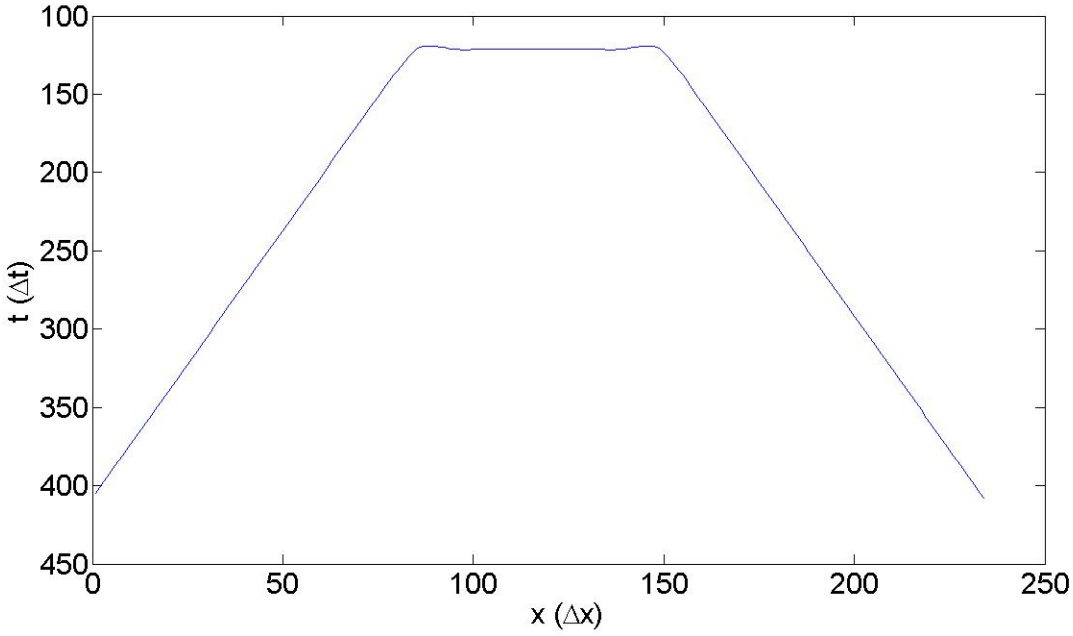

Figure B-62: Smoothened arch-like shape extracted from the B-scan image of slab D89W64

Bibliography

[1] H. M. A. Al-Matterneh, D. K. Ghodgaonkar, and W. M. W. A. Majid. Determination of compressive strength of concrete using free-space reflection measurements in the frequency of 8-12.5 ghz. In *IEEE Proc. APMC2001*, volume 2, pages 679–82, 2001.

[2] C. Aubagnae, X. Derobert, and O. Abraham. Comparison of ndt techniques on a post-tensioned beam before its autopsy. *NDT & E International*, 35:541–8, 2002.

[3] H. Begum, M. Okamoto, and S. Tanaka. Measuring the diameter of reinforcing bars in concrete nondestructively using electromagnetic wave radar. In *SICE Annual Conference 2008*, 2008.

[4] K. Belli, S. W. Fascetti, and C. Rappaport. Model based evaluation of bridge decks using ground penetrating radar. *Computer-Aided Civil and Infrastructure Engineering*, 23:3–16, 2008.

[5] K. Belli, C. Rappaport, H. Zhan, and S. W. Fascetti. Effectiveness of 2-d and 2.5-d fdtd ground-penetrating radar modeling for bridge-deck deterioration eval-

uated by 3d fdtd. *IEEE Transactions on Geoscience and Remote Sensing*, 47(11), November 2009.

[6] K. J. Bois, A. D. Benally, and R. Zoughi. Microwave near-field reflection properties analysis of concrete for material content determination. *IEEE T. Instrum. Measure.*, 49(1):49–55, 2000.

[7] O. Buyukozturk and H. C. Rhim. Modeling of electromagnetic wave scattering by concrete specimens. *Cement and Concrete Research*, 25(5):1011–22, 1995.

[8] O. Buyukozturk and T.-Y. Yu. Far-field radar ndt technique for detecting gfrp debonding from concrete. *Construction and Building Materials*, 23:1678–89, 2009.

[9] T. Chung, C. R. Carter, T. Masliwec, and D. G. Manning. Impulse radar evaluation of concrete, asphalt and waterproofing membrane. *IEEE T. Aero. Electronic Sys.*, 30(2), April 1994.

[10] X. Derobert, C. Aubagnac, and O. Abraham. Comparison of ndt techniques on a post-tensioned beam before its autopsy. *NDT & E International*, 35:541–8, 2002.

[11] B. Engquist and A. Majda. Absorbing boundary conditionsfor the numerical simulation of waves. *Mathematics of computation*, 31:629–651, 1977.

[12] M. Q. Feng, F. D. Flaviis, and Y. J. Kim. Use of microwaves for damage detection of fiber reinforced polymer-wrapped cooncrete structures. *Journal of Engineering Mechanics*, 128(2):172–83, 2002.

[13] B. Graybeal, D. Rolander, B. P. M Moore, and G. Washer. *Reliablity of Visual Inspection for Highway Bridges: Final Report*. FHWA, McLean, VA, 2001.

[14] S. Kharkovsky, A. C. Ryley, V. Stephen, and R. Zoughi. Dual-polarized near-field microwave reflectometer for noninvasive inspection of carbon fiber reinforced polymer-strengthened structures. *IEEE T. Instrum. Measure.*, 57(1):168–75, January 2008.

[15] S. N. Kharkovsky, U. C. Hasar, F. Akay, and C. C. D. Atis. Measurement and monitoring of microwave reflection and transmission properties of cement-based specimens. *IEEE T. Instrum. Measure.*, 51(6):1210–8, 2002.

[16] Y. J. Kim, L. Jofre, F. D. Flaviis, and M. Q. Feng. Microwave subsurface imaging technology for damage detection. *ASCE J. Engng. Mech.*, 130(7):858–66, 2004.

[17] G. Klysz, J.-P. Balayssac, and S. Laurens. Spectral analysis of radar surface waves for non-destructive evaluation of cover concrete. *NDT & E International*, 37:221–7, 2004.

[18] J. A. Kong. *Electromagnetic Wave Theory*. EMW Publishing, Cambridge, MA, 2000.

[19] S. Liu, Z. Zeng, and L. Deng. Fdtd simulations for ground penetrating radar in urban applications. *Journal of Geophysics and Engineering*, 4:262–7, August 2007.

[20] M. Maazi, O. Benzaim, D. Glay, and T. Lasri. Detection and characterization of buried macroscopic cracks inside dielectric materials by microwave techniques

and artificial neural networks. *IEEE Transactions on Instrumentation and Measurement*, 57(12), December 2008.

[21] C. Maierhofer, A. Brink, M. Rollig, and H. Wiggenhauser. Detection of shallow voids in concrete structures with impulse thermography and radar. *NDT & E International*, 36:257–63, 2003.

[22] T. Masliwec, T. Chung, C. R. Carter, and D. G. Manning. Impulse radar evaluation of concrete, asphalt and waterproofing membrane. *IEEE T. Aero. Electronic Sys.*, 30(2):404–15, 1994.

[23] D. M. McCann and M. C. Forde. Review of ndt methods in the assessment of concrete and masonry structures. *NDT & E International*, 34:71–84, 2001.

[24] J. Nadakuduti, G. Chen, and R. Zoughi. Semiempirical electromagnetic modeling of crack detection and sizing in cement-based materials using near-field microwave methods. *IEEE T. Instrum. Measure.*, 55(2):588–97, 2006.

[25] M. Neyrat, C. Guiffaut, A. Reineix, and F. Reynaud. Fast modelling using fdtd method and wave front inverse method for multisensor gpr simulations in the time domain. *Microwave and Optical Technology Letters*, 51(3), March 2009.

[26] S. Nojavan and F.-G. Yuan. Damage identification using electromagnetic waves based on born imaging algorithm. *Journal of Engineering Mechanics*, 135(7):717–28, July 2009.

[27] S. Oka, S. Mochizuki, H. Togo, and N. Kukutsu. A neural network algorithm for detecting invisible concrete surface cracks in near-field millimeter-wave images.

In *Proceedings of the 2009 IEEE International Conference on Systems, Man, Cybernetics*, San Antonio, TX, 2009.

[28] H. C. Rhim and O. Buyukozturk. Wideband microwave imaging of concrete for nondestructive testing. *Journal of Structural Engineering*, December 2000.

[29] M. R. Shaw, S. G. Millard, T. C. K. Molyneaux, M. J. Taylor, and J. H. Bungey. Location of steel reinforcement in conrete using ground penetrating radar and neural networks. *NDT & E International*, 38(3):203–12, 2005.

[30] K. S. Yee. Numerical solution of initial boundary value problems involving maxwell's equations in isotropic media. *IEEE Transactions on Antennas and Propagation*, 14(3):302–7, May 1966.

[31] T.-Y. Yu. *Damage Detection of GFRP-Concrete Systems Using Electromagnetic Waves*. Lambert Academic Publishing, Koln, Germany, 2009.

[32] T.-Y. Yu and O. Buyukozturk. A far-field airborne radar ndt technique for detecting debonding in gfrp -retrofitted concrete structures. *NDT & E International*, 41:10–24, 2008.

[33] H. Zhan, K. Belli, S. W. Fascetti, and C. Rappaport. Effectiveness of 2d fdtd ground penetrating radar modeling for bridge deck deterioration evaluated by 3d fdtd, booktitle =.

[34] R. Zoughi and S. Bakhtiari. Microwave nondestructive detection and evaluation of disbonding and delamination in layered dielectric-slabs. *IEEE T. Instrum. Measure.*, 39(6):1059–63, 1990.